Biophysical Population Models of the Auditory Nerve

Gabrielle O'Brien

A dissertation

submitted in partial fulfillment of the

requirements for the degree of

Master of Science

University of Washington

2016

Reading Committee:

Jay T. Rubinstein, Chair

Julie Bierer

Eric Shea-Brown

Program Authorized to Offer Degree:

Neuroscience

University of Washington

Abstract

Biophysical Population Models of the Auditory Nerve

Gabrielle O'Brien

Chair of the Supervisory Committee:
Professor Jay T. Rubinstein
Bioengineering & Otolaryngology

Biophysical models of the electrically stimulated auditory nerve are a powerful tool to simulate the neural response to cochlear implant stimulation. We review the history and development of these computational models, from single node Hodgkin-Huxley models to morphologically and physiologically inspired cable models of auditory nerve fibers. Next, we pair a stochastic, heterogeneous population model with two neurometric decision making paradigms to investigate the neural correlates of performance on the perceptual amplitude modulation detection task. The model predicts realistic modulation detection thresholds as a function of stimulus intensity and modulation frequency. When the decision criterion relates to fluctuations in instantaneous firing rate, low carrier rates are associated with better performance, but spectral analysis reveals that the modulation frequency is more strongly coded in the auditory nerve response at high carrier

rates. Finally, we consider the effects of simulated pathology on the model’s population-scale response. We develop a single-fiber model of peripheral degeneration and compare temporal and stochastic properties of three distinct population models of cochlear pathology.

TABLE OF CONTENTS

List of Figures iii

List of Tables iv

Chapter 1. The development of biophysical models of the auditory nerve: single node and cable models 1

- 1.1 Introduction 1
- 1.2 Single node models 4
  - 1.2.1 Classical node models 5
  - 1.2.2 Updating the classics 8
  - 1.2.3 Modeling noise and stochastic effects 8
  - 1.2.4 Modeling adaptation 11
- 1.3 Cable models 12
  - 1.3.1 Classical cable models 14
  - 1.3.2 Cable models for cochlear implants: morphological considerations 18
  - 1.3.3 Modeling neural degeneration 21
  - 1.3.4 Modeling heterogeneous populations 23
- 1.4 Future directions for biophysical modeling 23

Chapter 2. Simulating electrical modulation detection thresholds using a biophysical model of the auditory nerve 26

- 2.1 Introduction 27
- 2.2 Methods 30
  - 2.2.1 Auditory nerve model 30
  - 2.2.2 Stimulus synthesis and presentation 32
  - 2.2.3 Recreation of TMTF study 33
  - 2.2.4 Recreation of MDT-level studies 33
  - 2.2.5 Procedures for the estimation of MDTs 35
- 2.3 Results 39

2.3.1 TMTFs 39
2.3.2 MDTs as a function of stimulus intensity 43
2.3.3 MDTs and carrier rate 45
2.3.4 MDTs as a function of temporal precision and population size 47
2.4 Discussion 51
2.4.1 Comparing simulations to behavioral data 51
2.4.2 Possible loudness cues 55
2.4.3 Differences between simulated and psychophysical results 57
2.4.4 Effect of temporal precision 58
2.4.5 Contributions of fiber subpopulations 60
2.4.6 Summary 62
Chapter 3. Modeling pathology of the auditory nerve at the population scale 64
3.1 Introduction 64
3.2 Methods 67
3.2.1 Single fiber degeneration study 67
3.2.2 Population models 70
3.2.3 Stimulus 72
3.2.4 Measures of neuronal response properties 72
3.3 Results 73
3.3.1 Single fiber modeling 73
3.3.2 Population studies 80
3.4 Discussion 85
3.4.1 Single fiber modeling 85
3.4.2 Population models 88
3.4.3 Conclusions 90
Bibliography 92

LIST OF FIGURES

Figure 1.1 A schematic of an example cable model. 15

Figure 2.1 A schematic of the biophysical auditory nerve model. 31

Figure 2.2 The max-min decision rule. 37

Figure 2.3 Summary of TMTF results. 41

Figure 2.4 Summary of MDT results. 44

Figure 2.5 Fractional power of the modulation frequency across carrier rates. 46

Figure 2.6 Comparisons of MDTS with varied temporal precision and population size. 48

Figure 2.7 Effects of modulation depth on spike count. 50

Figure 2.8 Spike time raster plots for 250 pps and 2000 pps. 62

Figure 3.1 A schematic of the peripheral degeneration model. 70

Figure 3.2 A comparison of two population-scale models of auditory nerve pathology.. 71

Figure 3.3 Comparison of input-output functions, latency, and jitter across the dynamic range of three single fiber models. 74

Figure 3.4 Spike initiation histograms for three single fiber models presented with a threshold-level CF stimulus. 76

Figure 3.5 Comparison of input-output functions, latency, and jitter across the dynamic range for three models presented with AF stimulation. 77

Figure 3.6 Spike initiation histograms for three single fiber models presented with an AF stimulus. 79

Figure 3.7 Input-output functions, latency, and jitter across the dynamic range of a population of partially demyelinated ANFS. 81

Figure 3.8 Average input-output functions, latency, and jitter curves in randomly selected subpopulations. 83

Figure 3.9 Average input-output functions, latency, and jitter curves with fibers removed in order of diameter. 85

LIST OF TABLES

Table 3.1 Single Fiber Measurements for a Cathodic Phase First Stimulus..................... 75
Table 3.2 Single Fiber Measurements for an Anodic Phase First Stimulus 78

ACKNOWLEDGEMENTS

I could not have made the progress presented herein without the help of many individuals at the University of Washington. First, I would like to thank my mentor Jay T. Rubinstein for his guidance, advising, and generous book loans. I truly appreciate that you have always made time in your globe-trotting schedule to answer my questions.

My committee members Julie Bierer and Eric Shea-Brown should also be recognized. Julie, it is always a true pleasure to have you as a mentor and role model. Eric, I have been inspired by the work I saw rotating through your lab. My thesis would not be possible were it not for your generous allocation of node space on Hyak.

I would also like to thank the Neuroscience directors David Perkel and Jane Sullivan for their unwavering support and tireless devotion to the program.

Thank you to the researchers in the cochlear implant community who have been my mentors, friends, and co-conspirators: my bandmates David Horn and Ward Drennan, Steven Bierer and his bottomless file cabinet of useful papers, my superior conference travel buddies and unlicensed therapists Lindsay DeVries and Shae DeNino, and Matt Winn, who impressed on me the value of aesthetically pleasing graphs.

Perhaps most of all, thank you Nikita Imennov, my predecessor, for impeccably documenting more than two decades and three thousand lines of code before I arrived.

DEDICATION

Chapter 1. THE DEVELOPMENT OF BIOPHYSICAL MODELS OF THE AUDITORY NERVE: SINGLE NODE AND CABLE MODELS

This work is an invited literature review for which I am the first author, currently in press [1].

Chapter Summary

In the last few decades, biophysical models have emerged as a prominent tool in the study and improvement of cochlear implants, a neural prosthetic that restores a degree of sound perception to the profoundly deaf. Owing to the spatial phenomena associated with extracellular stimulation, these models have evolved to a relatively high degree of morphological and physiological detail: single node models in the tradition of Hodgkin-Huxley are paired with cable descriptions of the auditory nerve fiber. No singular model has emerged as a frontrunner to the field; rather, parameter sets deriving from the channel kinetics and morphologies of numerous organisms (mammalian and otherwise) are combined and tuned to foster strong agreement with response properties observed *in vivo*, such as refractoriness, summation, and strength-duration relationships. Recently, biophysical models of the electrically-stimulated auditory nerve have begun to incorporate adaptation and stochastic mechanisms, in order to better realize the goal of predicting realistic neural responses to a wide array of stimuli.

1.1 INTRODUCTION

Cochlear implants are neural prosthetic devices that convert acoustic vibrations into electrical stimuli, which are delivered directly to the auditory nerve via an implanted electrode array. Although cochlear implants provide high levels of speech perception to hundreds of thousands of deaf individuals, the device remains limited: the restoration of speech perception in noise, binaural hearing, pitch, and music perception are still incomplete [2]. Presumably, a more thorough understanding of the auditory nerve response to electrical stimulation will advance future devices. The task is laden with obstacles, though, including gaps in our understanding of coding in the acoustically-stimulated auditory system [3], the limitations of telemetry in implant recipients [4], and high performance variability across the implanted population [5], [6].

Computational models that simulate neuronal responses to cochlear implant stimuli are a powerful tool to enhance our understanding of neural coding beyond the capacity of experimentation alone. Although we cannot presently restore natural hearing to the deaf, it is within the scope of current technology to design advanced cochlear implant strategies for more optimal information transmission. Of course, owing to the enormous variability in performance between listeners and the time it takes to run a sufficiently large sample size through psychophysical testing, estimating the usefulness of a putative stimulation strategy is a task well-suited to tireless computational models. There are more fundamental reasons to simulate the auditory nerve as well: years before cochlear implants became a mainstream medical technology, computational models of extracellular stimulation addressed questions of basic science concerning the relationships between stimulus waveforms, electrical fields, and neuronal excitation [7].

Generally, computational models in the field of cochlear implants are categorized as either phenomenological or biophysical. In this article, we will review the development and contributions of the biophysical class of computational models of the electrically-stimulated auditory nerve. The canonical biophysical description of the excitable neuronal membrane is the Hodgkin-Huxley (HH) model [8], a set of nonlinear differential equations that describe changes in membrane potential over time (for review, see [9]). Biophysical models in this tradition generally describe the membrane potential in terms of ohmic ionic and/or capacitive currents. Compared to phenomenological models, the variables and parameters in a biophysical model typically have intuitive physiological interpretations; for example, modifications to axon diameter and the density of ion channels within a node are readily enacted through a simple dimensional analysis (although, as we will see, it is not necessarily straightforward to ascertain a physiologically realistic parameterization). This feature makes the class of biophysical models an attractive target for simulating neural responses to a medical device such as the cochlear implant. So far, biophysical modeling studies have probed the mechanism by which an electrical field generates spikes [10], the effects of stimulus and device parameters on neural activity [11]–[13], and the impact of cochlear pathology [14], [15], to name just a few advancements. Although this review is by no means comprehensive, it is our intention to survey the landmark developments and trends in biophysical models leading to the present state of the field.

Commonly, these biophysical models are comprised of three parts: a description of the conducting extracellular space and the implanted macroelectrode, a model of the spike-generating node of Ranvier, and a model of the passive myelinated internode. We will not discuss the extracellular space much here, as it is the focus of another review in this series. We begin with a discussion of *single-node models*, or those that describe the membrane potential as a function of time, but not space. Multiple single-node models arrayed in space can be joined with circuit elements representing myelinated internodes to describe a one- (or more) dimensional axon. This arrangement is called a *cable model*, and will be explored in the second half of the review.

1.2 SINGLE NODE MODELS

Numerous biophysical node models have captured the attention of cochlear implant researchers over the last fifty years, and even today, there is no universally preferred model (compare the recent simulations of [16]–[19]. The gamut of biophysical node models share a mathematical framework but differ in their ion channel parameters, particularly conductances (representing the density of each channel type) and kinetics (representing the speed of conformational changes in channels). Consequently, response characteristics—including the time course of neural activity and subthreshold behavior—vary by model. In the case of cochlear implant stimulation, which presently utilizes amplitude modulated pulse trains with a carrier frequency that ranges from 250-5000 Hz to transmit envelope information to the listener [2], these temporal response properties define a neuron's stimulus-encoding ability. Of particular concern, therefore, are the simulated fiber's refractory and summative properties. Refractoriness determines the post-action potential excitability of a neuron, and in the case of auditory nerve fibers driven by high rate cochlear implant stimulation, plays a significant role in the fiber's firing rate and temporal response. The absolute refractory period of a fiber depends on the time course of sodium channel deinactivation, and there is also a relative refractory period, in which the neuron's threshold is elevated. The summative properties of a fiber determine how quickly subthreshold potentials decay, which is another especially crucial quantity in the case of cochlear implants, where pulsatile stimuli follow one another in rapid succession. As we will see, models are often assessed on their ability to predict these two essential qualities, summation and refractoriness, and the search for parameterizations that most accurately capture them has been a significant driver in the development biophysical models of the electrically stimulated auditory nerve.

Before we begin, we make a terminological note to the reader: the use of the phrase "Hodgkin-Huxley" or "HH model" is inconsistent throughout the literature. It may refer any model whose equations follow the format of the HH model (regardless of its parameters), or it may refer to the exact model published in 1952. We will use the latter definition.

1.2.1 *Classical node models*

In the early studies of neuronal stimulation via electrical field, the canonical HH model was rejected on suspicion that it could not adequately describe the responses of myelinated nerve fibers, being fit to space- and voltage- clamp analyses of the non-mammalian, unmyelinated squid giant axon. The pioneering models of stimulation with an externally-applied electrical field [7], [20], [21] instead used the Frankenhaeuser-Huxley (FH) model of a myelinated amphibian node [22]. The FH formalism is nearly identical to that of the HH model. To quickly summarize, four differential equations representing the membrane potential and gating variables for voltage-gated sodium and potassium channels are solved to give the membrane potential as a function of time. The equation for the membrane potential is based on Kirchoff's law, in which the capacitive current of the membrane is equal to the sum of the inward and outward ionic and leak currents. For example, below are the equations for an abbreviated HH model used by Mino et al. (2002), which does not feature potassium channels:

$$I(t) = C_m \frac{dV_m(t)}{dt} + \frac{V_m(t)}{R_m} + g_{Na} m^3(t) h(t) (V_m(t) - E_{Na}) \tag{1}$$

where

$$\frac{dm(t)}{dt} = \alpha_m [1 - m(t)] - \beta_h m(t), \tag{2}$$

$$\frac{dh(t)}{dt} = \alpha_h [1 - h(t)] - \beta_h h(t). \tag{3}$$

In equation (1), $I(t)$ is the applied current as a function of time, C_m and R_m are the membrane capacitance and resistance, $V_m(t)$ is the membrane potential as a function of time, g_{Na} is the maximal conductance of the sodium current, and E_{Na} is the reversal potential of the sodium current. The terms on the right side of equation (1) describe, from left to right, the capacitive membrane current, the leak current, and a sodium current. In equations (2) and (3), α_m, β_m, α_h, and β_h are transition rates for the opening (α) and closing (β) of the activation (m) and inactivation (n) gates of a sodium channel. These transition rates depend on membrane voltage $V_m(t)$ and temperature (equations not shown for brevity). colo

The FH model differs from the HH model's conventions in two minor ways: the FH model uses ionic permeability in place of the HH model's membrane conductance, and the FH model incorporates an additional delayed nonspecific ionic current. It is noteworthy that many early applications of the FH model for functional electrical stimulation failed to account fully for the effects of raising the temperature parameter (originally 20° C) to warm-blooded levels (37° C) —potential modelers will benefit from browsing Rattay and Aberham's explanation of the discrepancy [23]. The temperature parameter tunes the magnitude and duration of action potentials, properties essential to an accurate description of neural firing rate and temporal response properties to cochlear implant stimulation.

Just as the HH model before it, the suitability of the amphibian model FH to model mammalian nodes was eventually called into question. Voltage clamp analysis of myelinated rabbit nerve fibers revealed "virtually no" fast potassium currents and sodium currents that inactive 2-3 times faster than in frogs [24]. An HH-style model that reconstructed the rabbit action potentials recorded by Chiu et al. was developed, and coined the CRRSS model, an acronym of the voltage clamp experimenters [25]. A contemporary of the CRRSS model is the

Schwarz-Eikhof (SE) description of rat and feline motor neuron nodes [26], which are similarly low in fast potassium channels. The SE equations follow the conventions of the FH model, having a permeability term and nonspecific ionic current.

Unexpectedly, the advantages of the mammalian models have proved controversial. In a comparison of the HH, FH, CRRSS, and SE models, only the “warm squid” HH model (the original model with its kinetic temperature parameter raised) was able to replicate certain phenomena of cochlear implant stimulation, including multiple spikes per stimulus period, and only the HH and SE models predicted realistic summation of subthreshold membrane potentials [23], [27]. Another comparison of the four models with pseudomonophasic stimuli found that, for the purposes of describing both refractoriness and summation properties of the auditory nerve, no model was superior [14], although some models accurately described one or the other at certain temperature parameters. Cartee resolved this discrepancy in a later publication by choosing the FH equations at 20° C for simulations of summation and the HH equations at 31°C for refractoriness [28]. It must be noted that the advantages of the classical HH model do not strongly suggest that the mammalian auditory nerve shares a physiological kinship with the unmyelinated squid giant axons. Rather, incomplete characterization of ion channel densities, kinetics, and electrical properties of the membrane in the usual experimental models of auditory nerve stimulation via extracellular electrical field (felines and guinea pigs) is a more probable culprit. Nor have the apparent benefits of the HH model choked out its peers—many researchers have continued to use, and successfully predicted refractory characteristics of the auditory nerve with, adaptations of the SE parameters [4], [13], [29], [30].

1.2.2 *Updating the classics*

More recently, discoveries in the wet lab have innovated the classical models with increasingly realistic descriptions of ion channel dynamics. It is now known that contrary to the equations of the SE and CRRSS models, potassium channels do, in fact, populate mammalian nerves [31], and there are in humans at least five channel types [32]. Although not crucial for repolarization post- action potential, various potassium channel types modify firing properties of the auditory nerve, including accommodation to constant current injection [33], [34]. Most modern biophysical models incorporate a fast potassium channel [11], [15], [35]–[37] and others contain an additional slow conductance potassium channel [16] to shorten the relative refractory period or low-threshold potassium channel [30] to simulate spike rate adaptation. Additionally, the increasing availability of human physiological data [38], [39] has led to the development of human node of Ranvier models in the HH-style [37], [40]. The human node model, although promising, does not totally account for observed auditory nerve excitation properties, a discrepancy the authors attribute to dynamical properties of their cable model, which were derived from squid data. At the time of press, most recent biophysical node models are not strictly faithful to any of the classical models, instead picking parameters from various sources and tuning them carefully for strong all-around quantitative agreement with the literature of recordings [16], [18], [35], [36].

1.2.3 *Modeling noise and stochastic effects*

Among the most daunting problems in cochlear implant research is the highly synchronous response of the auditory nerve to electrical stimulation [41]. One reason acoustic stimulation may offer more efficient information transfer is the statistical independence of auditory nerve fibers, owing to the stochastic properties of the hair cell synapse [42]. It is presumed that in cochlear implant recipients and animal models of both acute and chronic deafness, the auditory nerve receives no electrical input from the noisy hair cell synapse. Therefore, electrophysiological recordings of the electrically stimulated auditory nerve show an abnormally high degree of locking to the stimulus waveform, particularly when driven by low rate pulsatile stimulation [43], [44]. High synchrony is associated with stimulus frequency following; indeed, single nerve fibers have been observed to fire up to 800 Hz under electrical stimulation [45], considerably higher than is typical for acoustic stimulation [46].

In the last few decades, numerous studies using biophysical models have investigated putative cochlear implant stimulation strategies to enhance more natural, spontaneous neuronal activity [12], [13], [27], [47] capitalizing on the properties of inherently stochastic ion channels. Although neuronal noise is typically considered a synaptic phenomenon, auditory nerve fibers disconnected from the hair cell synapse exhibit threshold fluctuations [48] of a magnitude consistent with sodium channel noise at the nodal scale [49]. This noise represents the seemingly random transitions of individual ion channels between open and closed states [50]. Although this channel noise is orders of magnitude smaller than the noise introduced by the hair cell synapse, these random conformational changes may be sufficient to affect the initiation of spikes, making them a promising avenue of research. In particular, Rubinstein et al. [47] proposed the use of high carrier frequencies (2000-5000 Hz) to restore a degree of stochasticity to the auditory nerve response, such that the firing pattern of an electrically-stimulated fiber is modulated by its inherent refractory characteristics. Over a heterogeneous population where fiber threshold and refractoriness vary, this method may restore a degree of stochasticity without the need for stimulus-specific tuning.

Computational models have provided a useful tool for preliminary investigation of these proposed stimulation strategies, owing to the ease of implementation and precise control of parameters. Unfortunately, all the classical biophysical node models described in the previous section are purely deterministic, firing reliably whenever an intrinsic threshold is crossed. This renders them unsuitable to simulate stochastic phenomena as originally published. Some modelers have skirted this issue by pairing deterministic models with a Gaussian-noise current injection [12], [23]. This approach, while efficient, cannot capture the waxing and waning of noisiness as a function of membrane potential, which grows increasingly relevant at high stimulation rates [49], [51]. More complex algorithms have been developed to simulate voltage-dependent stochasticity in the Hodgkin-Huxley model, by modeling ion channel dynamics with Markov processes (for an overview, see [52]) or stochastic differential equations [53]. Essentially, Markov models describe random conformational changes in sodium and potassium channels by tracking channel subunit's transitions between active and inactive states. The Markov models that are prominent in the arena of auditory nerve modeling have transition rates (corresponding to the probability of an individual channel jumping between two states) dependent on the instantaneous membrane potential, and the transition rates as well as the state of each channel subunit must be recomputed at every time step of the solver. In stochastic differential equation models, on the other hand, noise terms are added to differential equations representing channel activation and inactivation variables (in the HH model, these are the m, h, and n variables). Clearly, this approach is considerably more efficient than many Markov models, particularly as the number of simulated channels grows.

In a comparison of four methods for simulating the stochastic state transitions of voltage-gated sodium channels, a Markov algorithm that tracks the number of channels in each state, but not the states of individual channels [54], was found to be the most accurate and computationally efficient [55] algorithm, compared to a deterministic model, a stochastic differential equation model, and Markov algorithms that simulate individual channels. Channel number tracking algorithms have since been widely incorporated in auditory nerve models [11], [13], [16], [18], [36], [56]. However, a recent mathematical analysis of stochastic differential equation models, suggests that with minor modifications, this formalism may accurately approximate Markov algorithms [57]. As the scale of simulations grows to incorporate large populations of auditory nerve fibers, stochastic differential equations may warrant reinvestigation as a more efficient strategy for simulating ion channel fluctuations.

1.2.4 *Modeling adaptation*

In response to a sustained stimulus, the firing of an auditory nerve fiber will attenuate in a process called adaptation. Changes in spike intervals and jitter have also been observed to accompany the decreasing firing rate [58]. The degree of adaptation depends on stimulation rate, with greater adaptation associated with high carrier frequencies, and generally occurs within 300 ms of stimulus onset [43], [59], [60]. As such, models that intend to predict neuronal responses to speech-like stimuli (on a time scale beyond a few phonemes) may benefit from incorporating an adaptation mechanism. Additionally, an accurate description of the mechanism for neuronal adaptation to repetitive stimulation is especially relevant to predict responses to high-rate stimulation. Yet none of the classical models describes long term adaptation in firing rate, although attenuation in repetitive spike amplitude [29] and rapid firing rate decrement on the scale of a few milliseconds have been reported [13], [47], [55].

At the time of press, two concurrent mechanisms of adaptation have been applied to biophysical models of cochlear implant stimulation. In the first by Negm and Bruce, a low-threshold potassium channel and hyperpolarization-activated channel, two channel types observed to co-localize on the somas of auditory nerve fibers [33], [34], supplement the traditional HH currents [18], [30]. The authors find that, alone and in conjunction, these currents modulate the adaptive and refractory properties of the neuron. They also observe complex changes in subthreshold activity that supports adaptation, in addition to firing rate decrements alone. In another mechanism developed by Woo et al., the concentration of extracellular potassium in a biophysical model is modeled as a dynamic variable; as this quantity accumulates over the course of repeated action potentials, changes in the electrochemical gradient affect the generation of new action potentials [17], [35], [36], [58]. Both mechanisms affect the refractory properties of the simulated auditory nerves, although neither model's predictions completely match the literature: the model of Negm and Bruce does not predict refractoriness out to 4 ms, as observed in feline and human experiments [61], [62], while the model of Woo et al. could not simultaneously reconcile physiological rate adaptation, recovery from adaptation, and refractoriness. Nonetheless, the incorporation of adaptation mechanisms is promising for a new generation of increasingly realistic models that predict neural responses to word- and sentence-length stimuli. It is not currently known which specific ion channels tune adaptive and refractory properties in feline and human auditory nerves, but experiments to isolate and quantify these channels will pave the way for models with more precise mechanisms.

1.3 CABLE MODELS

Single-node models have made useful contributions to our understanding of the neural coding of electrical stimuli [12], [27]. But, if the primary use of biophysical models is to predict the neuronal response to a given stimulus, then in the case of cochlear implant stimulation, certain stimulus-response relationships cannot be estimated with single-node models. In a single-node model, membrane voltage is a function of time but not space, and consequently, the presence of a spike depends on the injected stimulus intensity alone. This assumption is reasonable for a penetrating microelectrode. But when the current-injecting electrode doesn’t directly contact its neuronal target, as in a cochlear implant array, neuronal excitability depends not only on stimulus intensity, but also the electrode distance, electrode configuration (monopolar, bipolar, etc.), stimulus polarity, and stimulus frequency [7], [20]. For example, anodal and cathodal stimuli elicit opposing spatial patterns of activation that affect spike initiation site and threshold: cathodal (-) currents depolarize the fiber nearest the electrode and slightly hyperpolarize symmetrical nodes on either side of the central depolarization, whereas anodal (+) currents hyperpolarize the fiber centrally and slightly depolarize the surrounding nodes [63]. These patterns complicate neuronal responses: anodal stimuli can excite fibers to spike, albeit at higher thresholds than cathodic stimuli and at different spike initiation sites, and intense cathodic stimuli can prevent the transmission of spikes via decentralized hyperpolarization (cathodic block).

Furthermore, the temporal encoding of a stimulus depends on spatial factors. There is experimental evidence that stimulus polarity and intensity can modulate the site of spike initiation between central and peripheral nodes [45], [64]–[66], which will affect the latency of spiking, or time delay between stimulus and transmission of an action potential to a more central site. Likewise, electrode configuration [67], electrode-neuron distance [11], and fiber curvature [58] may also shift the spike initiation site. Similarly, the loss of peripheral processes in the axon due to pathology reduces latency and jitter, consistent with more centralized spike initiation [61], [64], [68]. Finally, spike entrainment to repetitive stimuli may be limited more by axonal conductance properties than the time course of a single node [69], so single node models may overestimate stimulus frequency following.

1.3.1 *Classical cable models*

As alluded to earlier, single node of Ranvier models distributed in space can be linked by circuit elements to construct a one-dimensional spatial description of the axon, called a cable model. In the classical cable models, the axon is chunked into discrete compartments, which may represent linear internodes or nonlinear nodes, and the electrical properties and voltage within each compartment are assumed to be homogenous (see Figure 1.1).

Spatial discretization allows for numerical solvers, such as the Crank-Nicolson algorithm [70], to efficiently solve the partial differential cable equation (which computes the membrane potential at each point, at each time step) over the entire simulated axon. Analytical solutions may be available, but this generally refers to the case where the nonlinear nodes are not modeled [71].

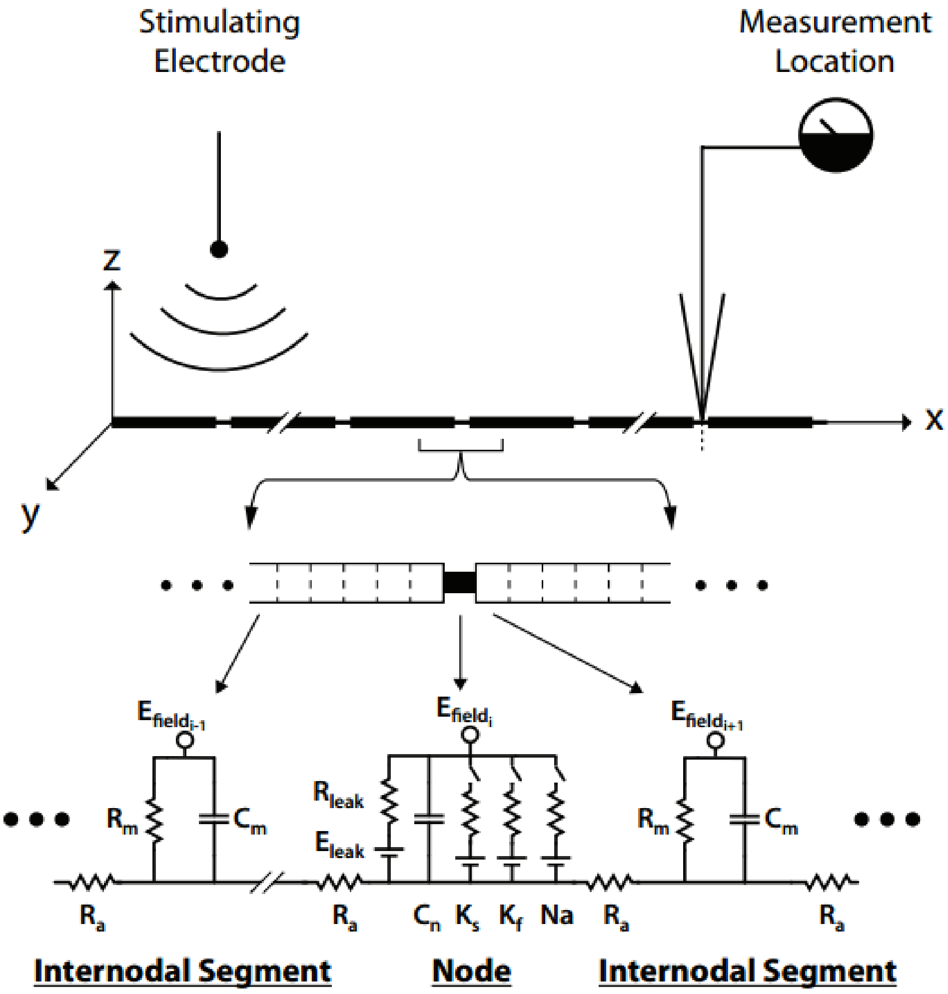

Figure 1.1 A schematic of an example cable model. An extracelluar stimulating electrode situated in a homongenous medium is located some distance away from the axon, and the presence of spikes is recorded at a more central node. The axon is divided into myelinated internodes by regularly spaced nodes of Ranvier. The internodes are in turn divided into discrete, equally-sized segments for simulation. The internodal segments consist of a linear circuit (R_m represents membrane resistance, C_m membrane capacitance, and E_{field} the extracellular field potential), and the nodes are described by a nonlinear model with numerous voltage-gated ion channel types (K_s represents slow potassium channels, K_f fast potassium channels, Na sodium channels, C_n the nodal capacitance, R_{leak} the resistance of the leak current, and E_{leak} the reversal potential of the leak current). This schematic is iterated along the entire length of the simulated cable, and the segments are linked by resistors (R_a) representing axoplasmic current. This figure is reprinted with permission of the authors of [16].

The morphology of the cable can vary from generic to highly species-specific, as we will see shortly. Fundamental to all morphologies is the preservation of diameter-dependent relationships: the length of the internodes is chosen to be proportional to the diameter of the axon sans myelination, as is thickness of the myelinated internode segments, in keeping with the theoretical treatise of Rushton [72]. Formally, these models describe an infinitely long cable, but of course only a finite length of cable is simulated. In fact, the membrane potential must only be computed for half the length of interest, because the responses will be symmetric around the locus of stimulation (for an electrode situated at a point arbitrarily assigned the coordinate $x = 0$, the membrane potential will be the same at $x = 1$ and $x = -1$). For further discussion and mathematical derivation of the cable equations, we refer the reader to a book chapter by Koch, "Linear Cable Theory" [73].

The first cable description of the myelinated mammalian nerve fiber consisted of HH nodes of Ranvier, joined by leaky internodal segments, each represented as a passive, leaky RC circuit [74]. Although generic, this model developed by FitzHugh qualitatively predicted the proportionality of fiber diameter, internode length, and conduction velocity [75]. The FitzHugh model was configured to simulate an injection of current that directly patches the membrane, which is insufficient to describe cochlear implant stimulation for the reasons described above. It was McNeal who first adapted this model for extracellular stimulation with a macroelectrode [7]. This model consisted of a single nonlinear FH node flanked by passive, perfectly insulating internodes, described by linear electrical circuits. While an incomplete description of the axon, this model possessed the advantage of computational efficiency; to its further credit, McNeal demonstrated that linear nodes were accurate descriptors of the nonlinear FH model except when their membrane potential exceeded ~80% of threshold. The McNeal model was the first cable model of extracellular stimulation that provided general solutions for arbitrary electrode configurations, allowing the computation of strength-duration curves for finite-duration stimuli.

The strength-duration curve is a vital descriptor of the excitatory properties of a nerve fiber, relating its firing threshold to the duration of a particular stimulus waveform. Grossly, the strength-duration curve represents the integrative and leaky membrane properties, as well as sodium channel density and kinetics. Of particular interest to cochlear implant researchers is the quantity known as chronaxie, defined as the stimulus duration at which the strength-duration curve is at 50% of its asymptotic value. In the electrically stimulated auditory nerve, measured chronaxies are considerably higher than observed in other sensory nerves [76]; the reasons for this will be discussed shortly.

On the scaffold of the McNeal model, Reilly et al. created the spatially extended nonlinear node (SENN) model—in essence, the McNeal model with multiple active Frankenhaeuser-Huxley nodes [20]. The SENN model raises the question, what are the minimum number of nonlinear nodes that must be simulated to adequately describe neural responses? McNeal found that a single node sufficed to describe spike initiation threshold to a nearby, monopolar, cathodal stimulus, but owing to the spatial effects previously mentioned, a single node is a poor descriptor of distant electrodes or anodal stimulus. To determine the number of nodes that must be simulated to capture such phenomena, Reilly et al. introduced the polarity selectivity ratio, the ratio of anodal to cathodal current thresholds. They concluded that electrode distance from the axon at which the ratio becomes roughly constant provides a scale factor for the length of fiber to be simulated.

Both the McNeal and Reilly models predicted strength-duration curves that depend on stimulus, electrode, and anatomical parameters such as fiber diameter and myelin thickness.

Although they are not tuned to represent either cochlear implant stimulation or the biophysical properties of the auditory nerve, the strength-duration curve relationships observed in these classical cable models are largely faithful to qualitative trends in the electrically-stimulated auditory nerve.

1.3.2 *Cable models for cochlear implants: morphological considerations*

It was not until 1987 that a model specific to the electrically stimulated auditory nerve emerged [21]. Motivated by the abnormally long chronaxie of auditory nerve fibers, Colombo and Parkins revamped the Reilly et al. cable model with feline auditory nerve morphology, simulating a bipolar neuron split by a large soma that cordons off a thin peripheral dendrite from the central axon. The authors also tweaked the FH-node model parameters for stronger agreement with recordings from single auditory nerve fibers in squirrel monkeys. This updated model featured shorter nodes of Ranvier (1μm) than the classical cable models, as well as axonal constriction surrounding the nodes, in agreement with contemporary discoveries in feline histology [77]. It also deviated from the infinite-cable paradigm described previously—although in practice only a finite length of cable can be simulated for any model, the Parkins and Colombo model ascribed a unique morphology to the axon terminal (it was, of course, still necessary to simulate a sufficient length of cable to capture the spatial effects of extracellular stimulation described by Reilly and McNeil). Specifically, the new model included a description of the unmyelinated terminal of the peripheral dendrite, which has a higher capacitance and longer time constant than the myelinated internode. It therefore influences the voltage profile at the axon terminal. The length of the peripheral unmyelinated terminal ultimately proved to be an influential parameter in Colombo and Parkins' model: chronaxie most strongly depended on the length of the peripheral unmyelinated terminal. The second most influential parameter was fiber diameter. Curiously, the authors were unable to identify a length for the peripheral unmyelinated terminal that predicted a chronaxie in the physiological range of squirrel monkey data (the actual length was unknown to the authors).

Shortly after, Frijns et al. combined guinea pig auditory nerve morphology [78], [79] with Colombo and Parkin's anatomical parameters to describe a large diameter, high spontaneous rate fiber [80], [81]. This model, featuring a modified SE node, successfully predicted numerous response properties in agreement with measured mammalian values, as well as phenomena such as aborted spikes with repetitive stimulation.

The appeal of feline and guinea pig morphology is the relative ease of comparison and validation: the wealth of single-fiber electrophysiology studies in these organisms allows modelers to tune kinetic, electrical, and anatomic parameters for optimal agreement with experimental results [16], [81]. Counter to this stream of animal models, Rattay et al. argued that morphological differences alone between man and feline may have major ramifications for spike travel time based on a comparison of two cable models [82], and suggested that these differences may lead to incorrect predictions about cochlear implant stimulus coding in humans. On this ground, Rattay et al. developed a human auditory nerve fiber morphometry that includes an unmyelinated soma, unmyelinated pre- and post-somatic compartments, and more dendritic peripheral process nodes than the feline model. Numerous research groups have since adapted the human cable model [4], [15], [19], although the precise morphology of human neurons is still largely uncharacterized. It must be noted that cable models with human morphology do not necessarily contain human node models- the Smit et al. model is entirely species-specific, whereas the node in the Briare and Frijns simulation is modeled with a modification of the SE model (rat and feline ion channel kinetics). Among their peer cable models, it is quite standard to have morphological, kinetic, and electrical parameters originating from a hodgepodge of species [16], [18], [35], [36].

Surveying the last three decades since Colombo and Parkin’s endeavor, the question arises: when is such attention to morphological detail (and all the extra parameters!) worth a modeler’s effort? In the class of cable models, anatomical parameters such as fiber diameter, node length, internode length, myelin thickness, and the length of the unmyelinated peripheral terminal influence strength-duration curves, to varying degrees [7], [20], [21]. At the very least, these details are justified in order to preserve the proportionality of diameter and conduction velocity [75]. But what about the soma and differentiated periphery? Despite modeling [82], [83] and experimental [64] evidence that the soma and peripheral processes may explain the long chronaxie of auditory nerves, some models exclude them. This decision reflects the priority of the modelers: certain studies intended to describe only the central axon [14], while others intended mainly to draw relative comparisons between stimulation paradigms [11], [13], [47]. At least one model has predicted an appropriately long chronaxie in a fiber without a soma, through widely distributed tuning of electrical parameters [16].

The question of how to best model myelination is not without debate, either. Many of the models discussed in this section make the simplifying assumption that myelin is a perfect insulator [7], [21], [25], while others treat it as an imperfect insulator in which some current may leach through the internodal myelin [29], [71], [74], [75]. A third option for modelers is the double cable model, in which the internodal myelin sheath is modeled as a separate compartment from the axolemma [19], which has the advantage of more accurately describing the recovery cycle after an action potential than the single cable model [84], [85]. In a recent study of the sensitivity of double cable model outcomes to the spatial discretization parameter of an internodal segment by Dekker et al., quantities including threshold, conduction velocity, and absolute refractory period were strongly dependent on the segmentation scheme [86]. It is therefore crucial to determine an appropriate implementation prior to varying other anatomical or kinetic parameters of the double cable model, particularly for small-diameter fibers where the effects of internodal segmentation are more dramatic. Dekker et al. helpfully suggest a computationally low-cost optimization in which only three segments per internode are necessary for predicting physiologically relevant behavior.

1.3.3 *Modeling neural degeneration*

In the chronically damaged cochlea, feline Type I auditory nerve fibers degenerate in stages: first, the peripheral dendrite degenerates, then the soma undergoes demyelination and shrinkage, and finally the central axon loses myelin [87]. Recently, the time course of degeneration has been demonstrated to occur on two scales, at least in the case of noise-induced pathology. In mice and guinea pigs subjected to auditory overexposure, the afferent nerve terminal (including the hair cell synapse) is irreversibly damaged on the order of hours to days post-exposure, but it may take months for the central auditory nerve to degenerate [88], [89]. In accord with this finding, a recent computational modeling study found that certain threshold profiles in human listeners could only be predicted when the model morphology consisted of a peripheral process stripped of its unmyelinated terminal [90].

In terms of neuronal activity, the consequences of degeneration are (generally) shorter latencies and decreased jitter, consistent with more central spike initiation due to compromised peripheral health [68]. In cable models, damage to the periphery is straightforward to implement. Colombo and Parkins' [21] manipulation of the peripheral unmyelinated terminal length describes the beginnings of degeneration, whereas Cartee's [14] model of an axon with uniform diameter describes extensive degeneration, such that spikes can only be initiated on the central axon. Removing the nodes and internodes of the periphery has also been used to describe soma-sparing degeneration [15], [19]. Simply widening the electrode-neuron distance may describe loss of peripheral processes in models that do not differentiate peripheral from central axon.

There is enormous potential for future models to innovate our understanding of the relationship between pathology and neural coding, not least because biophysical models allow straightforward manipulation of physiological parameters one at a time. Therefore, it becomes possible to isolate relationships between neuronal excitability and morphological changes, while the extent and complexity of disease studied *in vivo* may create prohibitive variability. Although it remains a distant goal, there is long-term interest in personalized models to optimally determine stimulation strategies and implant settings, which may take into account a listener's unique etiology of hearing loss. Models of pathology may inform new stimulation strategies in the future, and indeed already have begun to: in Briaire and Frijn's simulations of a volume-conducting model of the cochlea with degenerated nerve fibers [15], the authors reported significant benefits in terms of neuronal threshold, dynamic range and spatial sensitivity for peri-modiolar electrode arrays in the basal portion of the cochlea. Additionally, simulations of electrically evoked compound action potentials revealed a hallmark of neural degeneration that may be objectively measurable non-invasively. More recently, Smit et al. [19] predicted in a human auditory nerve model that the effect of degeneration on threshold varies with stimulation rate.

While these models have been useful, they incompletely represent the extent of degeneration known to occur *in vivo*. Abnormal bursting patterns are noted in response to sustained stimulation of degenerated fibers, suggesting a modification of the adaptation mechanism [68] that has not been explored in a computational model to date. Additionally, no model has yet incorporated the recent discovery that noise-induced damage preferentially affects small diameter, low spontaneous rate fibers [91].

1.3.4 *Modeling heterogeneous populations*

Many models, both phenomenological and biophysical, study single fibers or describe a population composed of a single iterated fiber. This assumption is limiting when predicting the neural responses to a stimulus strategy, because the mammalian auditory nerve is comprised of fibers with a range of diameters [79], [92], [93] and hence thresholds are not uniform across the population. Additionally, conduction velocity is proportional to fiber diameter [72], [75], which will affect the latency of neuronal responses. Jitter and refractoriness depend on threshold indirectly, as they change throughout a fiber’s dynamic range. In cable models of the auditory nerve that incorporate physiologically-distributed fiber diameters, this heterogeneity is advantageous for the coding of a stimulus, both in terms of transmitting fine temporal information [56] and representing modulations in the stimulus envelope [16], [92]. Heterogeneous populations also expand the dynamic range beyond that of a single fiber [27], which may better explain the range of comfortable intensities for a listener and the ability to perceive envelope modulations over that range.

1.4 FUTURE DIRECTIONS FOR BIOPHYSICAL MODELING

After decades of study, biophysical models of the electrically-stimulated auditory nerve have illuminated the mechanisms by which electrical fields stimulate neurons, relationships between morphology and neural excitability, and how complex mechanisms such as adaptation and stochastic fluctuations interact with cochlear implant stimulation. Moving forwards, we anticipate that biophysical models will continue to strive for better matches with physiology, as there is yet no model—rat, cat, or human—that manages to simultaneously capture the refractory, summative, adaptive, stochastic, and excitable properties of auditory nerve fibers from any species. In particular, new discoveries that better quantify the kinetics of human ion channels will inform the next generation of node of Ranvier models [37]. Additionally, as histology and electrophysiology continue to distinguish the effects of various pathologies on neural anatomy and activity [68], [91], we can expect more detailed models that better explain individual differences and aid in the prediction of optimal stimulation strategies and electrode settings. Finally, we hope to bridge the gap between biophysical details such as electrode distance, peripheral demyelination, stimulation rate, and pathological adaptation to predictions about the perception of complex stimuli. This will entail pairing biophysical models with decoding paradigms from information theory and signal detection theory [56], [94] to better understand the relationship between model parameters and the efficiency of information transmission. Here, biophysical models are at a relative disadvantage compared to phenomenological models, in which analytical techniques are available to readily predict the discriminability of stimuli and the information content of a particular neural response [95], [96]. Fortunately, there are numerous theoretical techniques that allow similar measures to be made on the spike times that are output by a biophysical model, including spike train distances [97], [98] and statistical methods [99]. Of course, these techniques require large sample sizes; the availability of high performance computing clusters on most academic campuses should render this caveat tractable for all but the most painstakingly detailed models so long as stimulus lengths are kept short. With the concurrent developments of ever more accurate, nuanced models and theoretical methods to analyze and crack the neural code, biophysical models may continue to mature into an indispensable tool to streamline the development of optimal cochlear implant strategies.

Chapter 2. SIMULATING ELECTRICAL MODULATION DETECTION THRESHOLDS USING A BIOPHYSICAL MODEL OF THE AUDITORY NERVE

This work is a first-author manuscript currently under review [100].

Chapter summary

Modulation detection thresholds (MDTs) assess listeners' sensitivity to changes in the temporal envelope of a signal and have been shown to strongly correlate with speech perception in cochlear implant users. MDTs are simulated with a stochastic model of a population of auditory nerve fibers that has been verified to accurately simulate a number of physiologically important temporal response properties. The procedure to estimate detection thresholds has previously been applied to stimulus discrimination tasks. The population model simulates the MDT – stimulus intensity relationship measured in cochlear implant users. The model also recreates the shape of the modulation transfer function and the relationship between MDTs and carrier rate. Discrimination based on fluctuations in synchronous firing activity predicts better performance at low carrier rates, but quantitative measures of modulation coding predict better neural representation of high carrier rate stimuli. Manipulating the number of fibers and a temporal integration parameter, the width of a sliding window, varies properties of the MDTs, such as cutoff frequency and peak threshold. These results demonstrate the importance of using a multi-diameter fiber population in modeling the MDTs and demonstrate a wider applicability of our model to simulating behavioral performance in cochlear implant listeners.

2.1 INTRODUCTION

The temporal envelope of a sound, expressed as slow fluctuations in its amplitude, is vital to the successful perception of speech [101], [102]. The ability of cochlear implant (CI) listeners to discriminate a non-changing envelope from a modulated (changing) one has been shown to correlate well with vowel, consonant, and phoneme recognition [103]–[105], as well as with tone and intonation recognition [106], [107]. This discrimination ability is measured using modulation detection thresholds (MDTs), which specify how large the amplitude changes have to be for the listener to consistently differentiate a changing from a non-changing stimulus amplitude. The correlation between MDTs and clinical outcomes with CIs suggests that an accurate model of envelope discrimination could potentially be used to predict the real-world performance of CI sound encoding strategies.

To successfully estimate modulation detection thresholds, a biophysical model has to capture the thresholds' dependence on a number of stimulus parameters. The overall loudness, rate of envelope modulation and carrier pulse rate are three well-studied and important features of acoustic and electric stimulation that can affect listeners' performance on MDT tasks. A typical cochlear implant listener can detect smaller envelope fluctuations if the stimulation intensity (volume of the sound) is large [6], [104], [108], [109]; conversely, increasing the modulation frequency attenuates the subject's performance [5], [110] as does increasing the carrier pulse rate [6], [108], [109].

Because all of the information used to discriminate the stimuli is contained in the spiking patterns of the listener's auditory nerve fibers (ANFs), researchers have examined the effects of stimulus intensity and modulation frequency on *in-vivo* neural responses to better understand and simulate the discrimination process [111]–[115]. It is known that in the normal cochlea, amplitude modulation around characteristic frequency is represented in the auditory nerve as an increase in synchrony around the modulation frequency with increasing modulation depth; because firing rate is generally invariant to modulation, the central decoder must make use of temporal cues to detect modulation. In the more limited set of neural recordings from an electrically stimulated cochlea, the peristimulus time histogram takes the shape of the stimulus envelope and the firing rate increases with modulation depth, even when the peak amplitude is fixed [43].

Computational modeling is a tool that, when properly validated, can provide insights that are difficult to observe *in vivo*. However, many of the simulations used to date employed phenomenological models that capture only the most basic characteristics of the neural response. Previous predictions of MDTs from simulations have used filter banks [116], a single unit inferior colliculus model [117], point process modeling [94], and a stochastic, homogenous ANF population [118]. Simulations by Heinz et al. have incorporated mixed fiber diameters, but were configured for acoustic stimulation [119]–[121]. While all these models have been able to make powerful predictions about auditory nerve fiber responses to electrical or acoustic stimuli, they do not contain the level of description necessary to account for the contributions of different fiber subpopulations to the neural code for electrical hearing. To a far greater degree than in acoustic hearing, fiber recruitment and temporal response properties are directly related to fiber geometry in electrical hearing, thus heterogeneity in the population is not negligible.

Unlike preceding efforts, our model consists of a diameter-distributed population of fibers whose response has been shown to accurately capture multiple temporal and excitation properties of the auditory nerve [16] and to simulate the behavioral trends observed in tests of temporal fine structure discrimination [56]. By applying our model to study a slower temporal phenomenon, the envelope, we examine the importance of spike time precision at different modulation frequencies, how individual fibers contribute to modulation detection, and whether the modeled performance is consistent with the perceptual trends observed in CI listeners.

In the present study, we recreate three classic psychophysical experiments in our model. Because our model allows us to simulate realistic population responses to the same stimuli used in the testing booth during the amplitude modulation detection task, we are able to test two hypotheses about the neurometric decision making rule used to complete the test. One hypothesis is that discrimination is based on phase locking to the modulation frequency, as observed in electrophysiological recordings from single units in normal hearing animal models. An alternative hypothesis is that discrimination depends on the magnitude of fluctuations in the instantaneous population firing rate. The first hypothesis implies that the modulation frequency of the stimulus is coded by the temporal characteristics of the population response. The second hypothesis does not, as it describes a decision rule based on detecting changes in the magnitude of the population response, not a spectral feature. It is perhaps akin to the use of a loudness cue.

First, we replicated an experiment by Shannon assessing the relationship between modulation frequency and MDTs [5]. Second, we examine the effects of increasing stimulus intensity on modulation detection using the method of Galvin and Fu [6]. Finally, we compare the effects of stimulus carrier pulse rate on MDTs as measured in cochlear implant subjects [6], [109].

2.2 METHODS

2.2.1 *Auditory nerve model*

A spatially-distributed, biophysical model of electrically stimulated auditory nerve fibers was used to simulate all of the neural responses presented here. Nodes of Ranvier within each model fiber are represented by stochastic, voltage-dependent ion channels (sodium, fast potassium and slow potassium), a leakage current and a membrane capacitance, while the myelinated internodes are modeled by resistive and capacitive elements of the membrane (Figure 2.1A). The geometric dimensions of the model fiber are based on the morphology of a typical cat Type I spiral ganglion peripheral process, described in detail elsewhere [16]. The parameterization of the model as such was motivated by the extensive knowledge of the structural and response properties of these mammalian fibers [92], [122]

In addition to replicating the behavior of single fibers, the model also simulates the in-vivo response characteristics of a population of fibers. Using fibers with an anatomically accurate distribution of fibers (Figure 2.1B and C), our model accounts for the range and log-normal distribution of normalized thresholds measured in animal studies [123]. These findings suggest that a diameter-distributed set of model fibers may be sufficient to represent in-vivo population response behavior under a number of different experimental conditions.

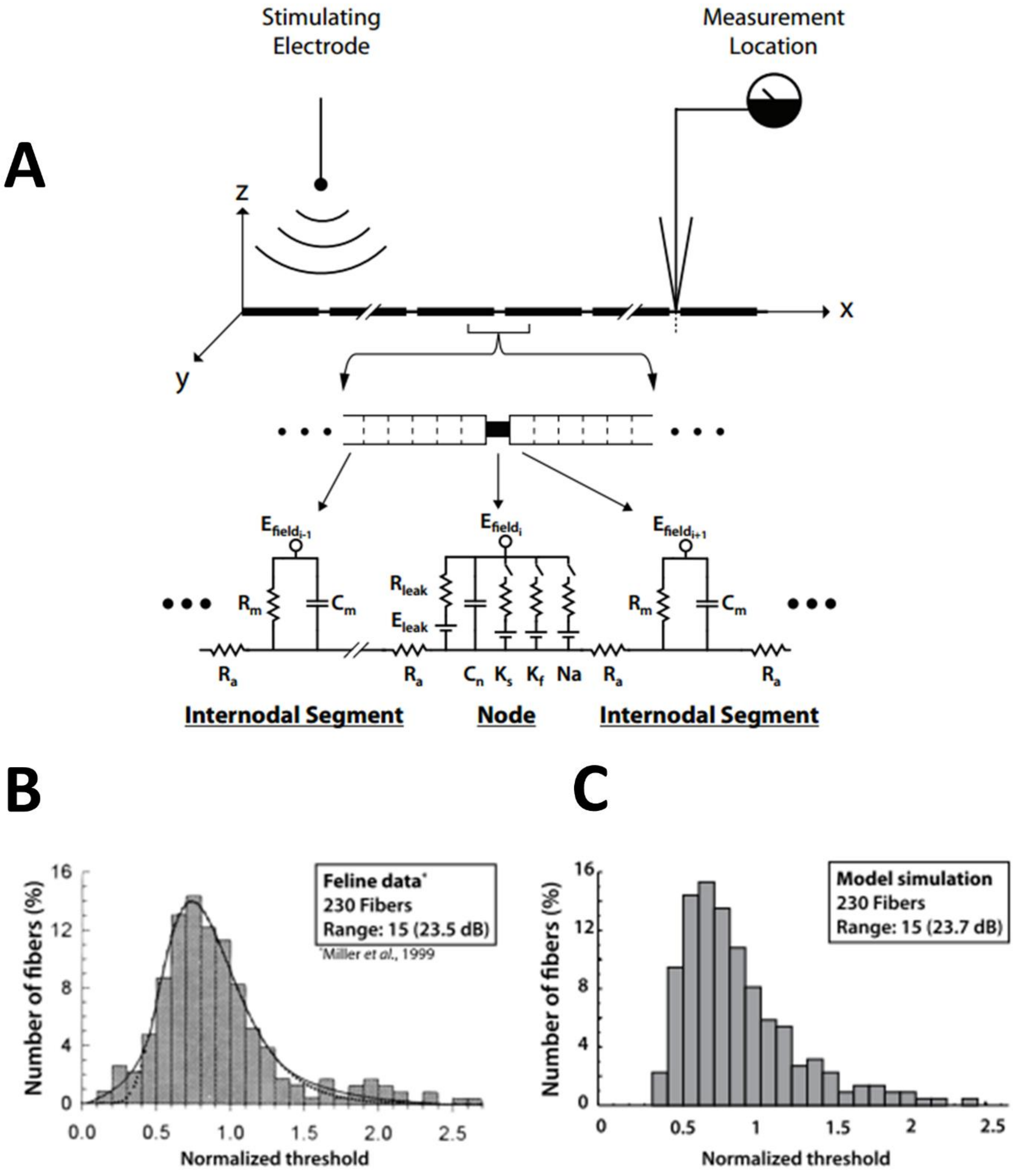

Figure 2.1 A schematic of the biophysical auditory nerve model. (**A**) Description of the model of spiral ganglion peripheral process. Note that the internodal segment is deterministic while the node of Ranvier contains stochastic ion channels. (**B**) Experimentally obtained, normalized thresholds of Type 1 feline auditory nerve fibers. (**C**) Normalized thresholds of the distributed diameter model. All images reprinted with permission from [16].

2.2.2 *Stimulus synthesis and presentation*

Whenever possible, stimulus settings matched the parameters in the psychophysical cochlear implant studies conducted by Shannon [5] and Galvin and Fu [6], [109]. In all cases, the biphasic, 100 µs wide per phase pulse trains were delivered to a single electrode situated 3 mm from the fiber axons at a fixed distance from the termination of each fiber. Although a 3 mm space between electrode and the spiral ganglia is relatively large for an implanted cochlea, the distance is appropriate for a model of an electrode in a homogenously conducting medium. Because the highly resistive bone is not modelled, the ‘electrical distance’ must be greater to accurately describe the true geometric distance with a resistive boundary separating the cochlear fluid from the auditory nerve [11], [124]. The amplitude of the fixed-envelope signal was sinusoidally modulated to produce the stimulus waveform *f(n)*:

$$f(n) = 1 + m_i \cdot \sin(2\pi \cdot m_f \cdot t_n) \ ,$$

where $m_i \in [0,1]$ denotes the modulation depth, m_f the frequency of modulation, and t_n corresponds to the time of the *n*-th pulse. In preliminary testing, the duration of the stimuli was set to 400 ms, the same length of time used in behavioral analogues to our study. However, we found that, due to the periodic nature of the responses, MDT estimates remained the same if the duration was decreased to 100 ms. Due to the computational expense of the detailed model, the shorter duration was used. A consequence of equal duration stimuli is that fewer cycles are presented of low modulation frequencies than high modulation frequencies. Interestingly, psychophysical studies with CI users have also shown that MDTs were largely fixed across different stimulus durations [106].

2.2.3 *Recreation of TMTF study*

To compare our results with those presented by Shannon, the temporal modulation transfer function (TMTF) was calculated by iteratively setting m_f to 10, 20, 50, 80, 100, 150, 200, 250, 300 and 350 Hz and estimating the modulation detection threshold at each corresponding frequency. The carrier pulse rate was fixed to 1000 pps as reported. Prior to conducting the experiment, stimulus intensity was adjusted to a level at which approximately half of the fibers responded to an unmodulated waveform. We assumed this level to be a reasonable proxy for mid-dynamic range stimulation because neural responses were always evoked yet were never saturated at any of the modulation frequencies.

2.2.4 *Recreation of MDT-level studies*

In our recreation of Galvin and Fu's experiments relating stimulus intensity to modulation detection, the modulation frequency was fixed to 100 Hz, the carrier pulse rate was fixed to either 250, 1000 or 2000 pps and the effects of loudness were measured by adjusting the current of the model's monopolar electrode to control the intensity of the stimuli. Galvin and Fu compared MDTs measured with various carrier rates over a range of modulation frequencies. They concluded that variation of modulation frequency in the range tested (20 Hz to 100 Hz) did not significantly affect the MDT curves. Therefore we replicated their experiment with only one modulation frequency.

A primary objective of our experiment was to compare MDT curves across carrier rates. This is challenging because of differences in the dynamic range and thresholds associated with carrier rate. Galvin and Fu observed loudness differences for the same stimulus intensity across carrier rates and therefore balanced stimulus intensities to a reference level in all tests. Because the explicit code for loudness is unknown [125]–[129], we followed the example of Bruce et al. [95] and Goldwyn et al. [94] who related stimuli by spike count. Spike count was defined as the number of spikes elicited from the population during one modulation cycle (10 ms) of a stimulus, averaged over 60 trials. Therefore, two unmodulated stimuli that elicit on average the same number of spikes are assumed to be loudness balanced. While this method can only approximate loudness balancing, it seems likely to dramatically improve the quality of comparisons across carrier rates.

For each carrier rate, the bottom of the stimulus intensity range was determined by lowering the current until an unmodulated stimulus generated action potentials. Across carrier rates, we observed that the simulated MDTs followed a rise-plateau-decline pattern as the stimulus amplitude is increased. To match the behavioral trends, we chose a maximum stimulus intensity so that MDTs were approximately monotonic functions of stimulus amplitude. In keeping with our proxy for loudness balancing, we found the upper bound on the 1000 and 2000 pps carrier rates' intensity that elicited roughly equivalent spike count to the maximal stimulus amplitude at 250 pps. Once these boundaries were established, stimuli were supplied at 8 evenly-spaced current levels that spanned the dynamic range of the modeled population.

One minor difference between our stimuli and the stimuli used in Galvin and Fu's experiments is that their biphasic pulse trains have a 45 μs interphase gap, whereas ours do not. We found that incorporating the gap into our stimuli had no significant effect on the shape of the MDT curves besides shifting them along the stimulus intensity axis (not shown). This is consistent with psychophysical results [130], [131] which show that interphase gap decreases threshold for neuronal activity. Therefore we have not included the interphase gap in any of our stimuli.

2.2.5 *Procedures for the estimation of MDTs*

Modulation detection thresholds in the Shannon and Galvin and Fu experiments were established adaptively, by iteratively changing the depth of modulation until the subjects could successfully discriminate modulated from unmodulated stimuli on 79.4% of the trials. While adaptive threshold-finding is well-suited to behavioral testing, the sequential nature of the adaptive procedure is highly inefficient when applied to large-scale, distributed computer models such as the one used here. Rather than waiting for one set of neural responses to be generated before modeling responses to the next, to efficiently allocate our computational resources, we simulated model output for a range of modulation depths and determined the thresholds *post-hoc*, by interpolating the m_i value that corresponded to a 79.4% correct performance.

We estimated performance on the psychophysical task using two distinct discrimination procedures in order to compare the results across two decision-making strategies. The first procedure is hereafter called the *max-min* rule, and it entails identifying modulation by large fluctuations in the population activity. This procedure was implemented in three steps. First, we simulated the neural responses to a given stimulus. Then we applied a model of temporal integration and detected modulation in the integrator output. The second procedure is a traditional metric for modulation detection, vector strength, which quantifies neural phase locking to the modulation frequency.

2.2.5.1 The max-min rule

The neural response to a given stimulus was computed independently for every fiber, as there are expected to be no synapses or stimulus-independent correlations between the activity of peripheral auditory nerve fibers [46]. We combined the neural responses from all fibers into a population response and discarded the identities of the individual fibers. This describes a putative neural code for stimulus amplitude as the summed population activity as a function of time. It is possible that a labelled line code, in which pooling the contributions of fibers decreases information about the stimulus, is used by the auditory nervous system. However, the results presented here suggest that the summed population firing rate is sufficient to account for the behavioral trends observed in MDT studies.

In order to convert the discrete spike times into a population firing rate that is a smooth function of time, temporal integration was performed by passing an integration window over the pooled spike times. This is equivalent to convolving unit-impulses at each spike time with the window function. We selected a tapered rectangular window (the Tukey window in MATLAB, defined as a rectangular window with the first and last 25% of points equal to parts of a cosine) as a compromise between the time domain precision of a rectangular window and the well-behaved band stop attenuation of a cosine window. The width of the window (effectively, the amount of smoothing applied to the neural response, denoted hereafter by $\Delta\tau$) was varied from 1.5 ms to 4.5 ms, with the area under the window fixed for all widths.

The process of detecting modulation in the output of the temporal integrator is derived from [132]. A decision statistic was computed as the ratio of the maximal firing rate to the minimal firing rate for the duration of the stimulus[1] (Figure 2.2A). For stimuli with 250 pps carrier rates, the firing rate function is a series of peaks spaced 4 ms apart that rapidly decay to

---

[1] 1. When using a ratio, care must be exercised that the denominator (the minimum population firing rate) does not approach zero too closely. In order to prevent this, a value of one was added to both the maximum and minimum. The exact value of this number is insignificant and we have checked that MDT estimations are not sensitive to it.

zero on either side (Figure 2.2B); therefore the decision statistic for this condition is not the ratio of the maximum to the absolute minimum firing rate but the ratio of the maximum to minimum peaks.

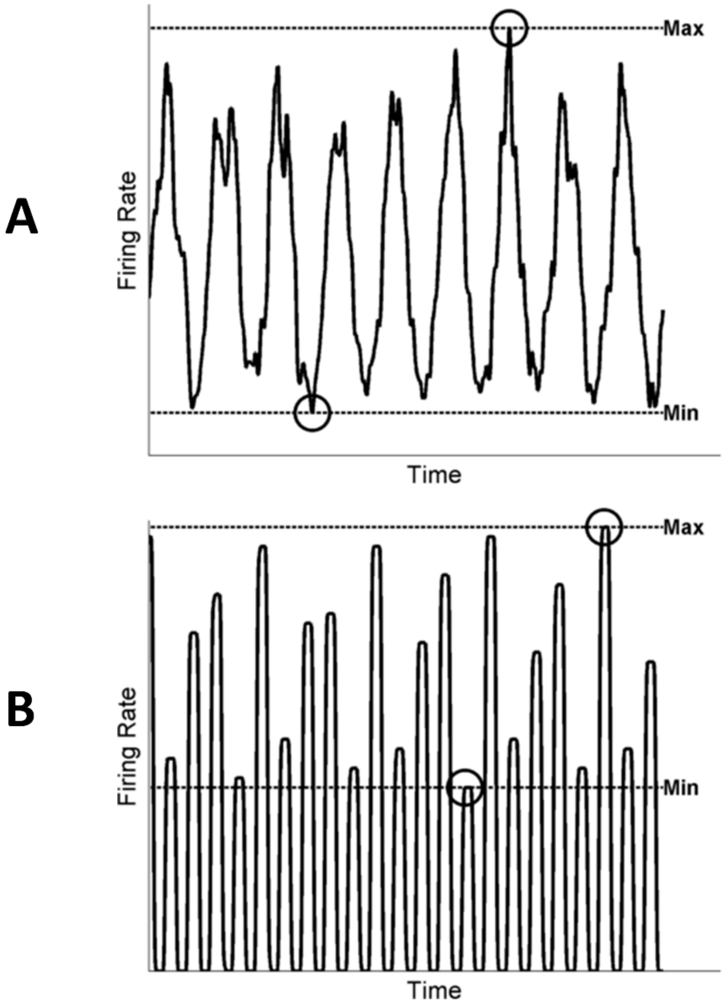

Figure 2.2 The max-min decision rule. (A) The max-min decision rule applied to the population firing rate function for the 1000 pps and 2000 pps carrier rate experiments. The plot shows a real example of the population firing rate over time in response to a modulated, 2000 pps stimulus. (**B**) The max-min decision rule applied to the population firing rate over time for the 250 pps carrier rate experiment. Unlike at pulse rates over 1000 pps, spikes occur in periodic pulses locked to the stimulus. We consider a putative code for modulation based on fluctuations in population firing rate.

For a given pair of modulated and unmodulated stimuli, the decision statistic was computed for each population response, and if the statistic was higher for the modulated stimulus, correct detection was said to have occurred. As the onset of either a modulated or unmodulated stimulus elicits a massive wave of synchronized spikes across the population, we discarded the first 10 ms of the simulated response from the modulation detection process.

Our detailed auditory nerve model poses considerable computational expense to run, but sufficient sampling of the stochastic responses is essential for predicting psychophysical thresholds. In order to simulate repeated presentations of the stimulus to the population, we took advantage of the fact that the individual neural responses are independent of one another and the identities of the fibers are discarded in the decision procedure. For each fiber, 6 responses were computed for a given stimulus, and population responses were generated by selecting one trial at random for each fiber to add to the pooled set of spike times. As such, there were 125^6 possible unique population responses. For a given modulated-unmodulated stimulus pair, we simulated the detection task 250 times and assessed the proportion of correct classification; increasing the number of iterations beyond 250 had little effect on the MDT predictions.

2.2.5.2 Vector strength discrimination

Vector strength is a popular metric that has been used to analyze auditory nerve responses to AM stimuli (for review, see [114]), simulated auditory nerve spike trains [94] with CI stimulation, and auditory cortex responses to CI stimulation [133]. Whereas the max-min rule is informative only about the scale of fluctuations in population firing rate, vector strength quantifies the degree of stimulus envelope coding in these fluctuations.

To decode by vector strength, the same procedure was used as the max-min rule except that the decision variable was the vector strength measure of phase locking applied to the pooled population spike times. Let $\theta_i \in [0, 2\pi]$ $(i = 1, \dots, N)$ be the phase of the ith spike relative to the period of modulation. Then the VS is defined to be [134]:

$$\mathrm{VS} = \frac{\sqrt{(\sum \sin \theta_i)^2 + (\sum \cos \theta_i)^2}}{N}$$

The VS measure is therefore a function that takes spike times normalized to the modulation cycle and produces a single value between 0 and 1 that quantifies the distribution of spike times relative to the modulation period. If VS = 0, spike times are randomly distributed around the period, whereas VS = 1 indicates perfect phase locking. The vector strength measure can give spuriously high values if there are few spikes present, so whenever less than three spikes were available, a value of 0 was assigned.

2.3 RESULTS

2.3.1 *TMTFs*

The dependence of modulation detection thresholds on the modulation frequency m_f are summarized in a plot of temporal modulation transfer functions (Figure 2.3). Shannon's psychophysical results are shown for reference in Figure 2.3A and simulated TMTFs using the max-min rule are shown in Figure 2.3B. Modulation frequency is shown on the *x*-axis and the modulation detection thresholds are measured in log-transformed (to dB) modulation depth on the *y*-axis. Thresholds at smaller m_i values, displayed near the top of the ordinate axis, correspond to better discrimination performance. The only difference among the MDT curves is that these estimates were produced using different $\Delta\tau$ values, specified in the figure legend.

In Figure 2.3B, one can see that increasing the width of the temporal integration window attenuates performance at higher modulation frequencies. When $\Delta\tau$ = 2.5 ms, the TMTF is fairly flat. Increasing $\Delta\tau$ to 3.0 ms gives a nearly identical TMTF, so for ease of reading it is not shown. Increasing $\Delta\tau$ further to 3.5 ms yields a lowpass curve that declines for modulation frequencies greater than 100 Hz. Interestingly, when $\Delta\tau$ = 4.0 ms, the result is a bandpass shape with best modulation detection at 100 Hz. This tuning is a result of the fact that a 4 ms-wide window covers almost half the duty cycle of a 100 Hz sinusoidal modulation (the up-modulation is 5 ms long), so this window size will preferentially boost 100 Hz modulations. This window size gives the best overall modulation detection at its peak, and also the steepest drop in performance and worst performance at high modulation frequencies. Interestingly, increasing the window size much beyond 4.0 ms does not continue attenuating the cutoff frequency.

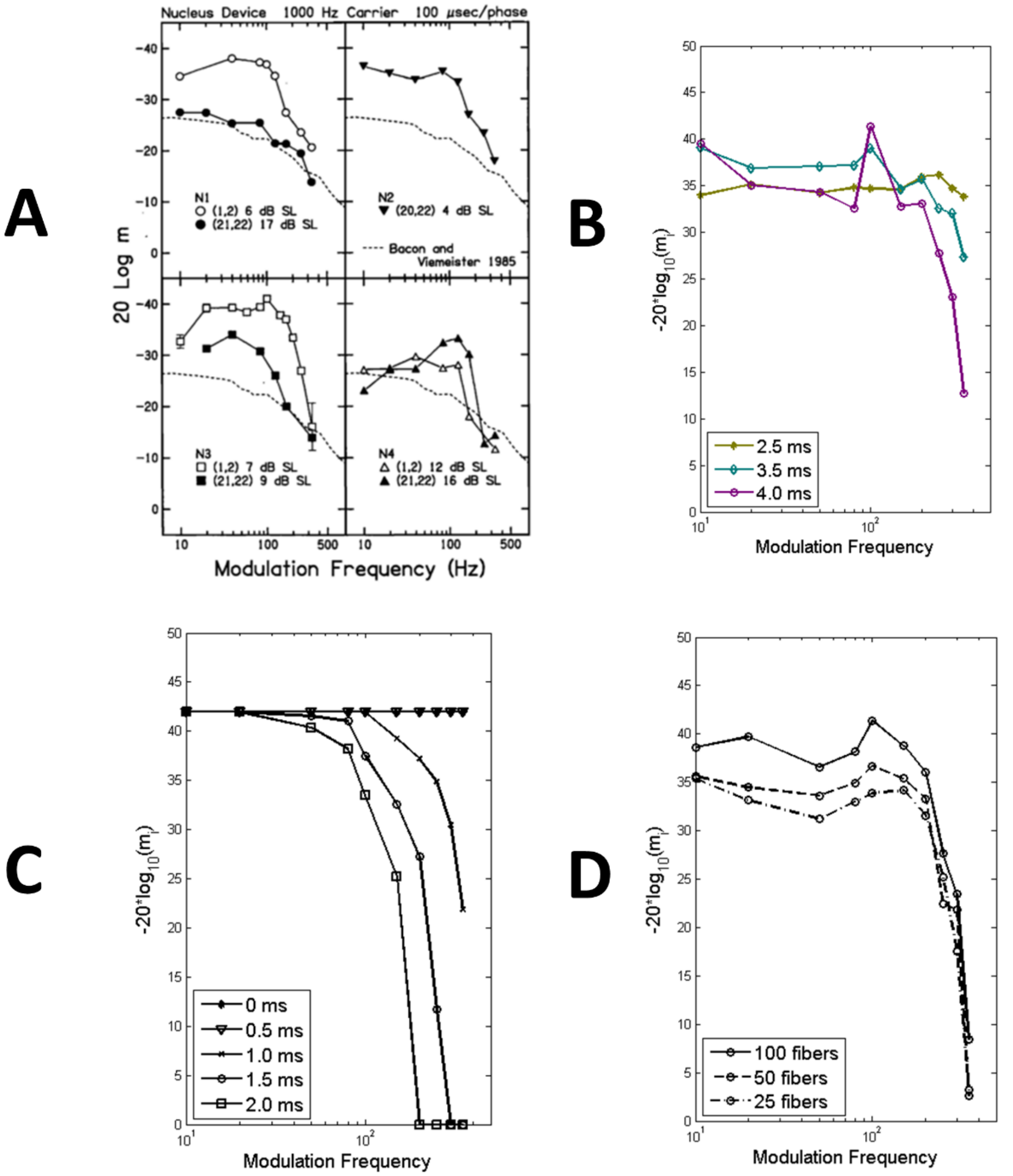

Figure 2.3 Summary of TMTF results. **A**) TMTFs in four CI listeners, compared at two intensity levels. Reprinted with permission from [5]. Copyright 1992, Acoustic Society of America. (**B**) TMTFs calculated with the max-min rule. The various curves correspond to results obtained with different window sizes. (**C**) TMTFs calculated with the VS rule. Curves represent the addition of Gaussian jitter and are indexed by jitter standard deviation. (**D**) TMTFs compared by the population size using the max-min rule with $\Delta\tau = 2.5$ ms.

We estimated TMTF cutoff frequency using the same procedure as Shannon: for the downward sloping part of the curves, we fit a regression line (in the log-frequency domain) and calculated the frequency at which the regression line had dropped 3 dB from peak selectivity. For the smaller windows ($\Delta\tau$ = 2.5 and 3.0 ms) the estimated cutoff frequency was beyond the range of modulation frequencies tested. This suggests that these TMTFs are poorly described as lowpass or bandpass functions. For the larger windows, the regression lines better fit the data and predicted cutoff frequencies within the range of modulation frequencies presented. The relationship between bin width and cutoff frequency is not linear: 3.5 and 4.0 ms phenomena correspond to 285 and 250–Hz events respectively, while TMTF cutoff frequencies corresponding to these $\Delta\tau$ curves are approximately 175 and 130 Hz. For comparison, the CI listeners in Shannon's study have highly variable cutoff frequencies, ranging from 96 Hz to 171 Hz.

The presence of flat TMTFs when small temporal integration windows are used suggests that the simulated auditory nerve responses are in fact locked to modulation frequencies up to 350 Hz. Thus the decrement in modulation detection at these frequencies typically observed in psychophysical results may be caused by a more central smoothing mechanism, represented in our model as larger temporal integration windows. To confirm that the auditory nerve model codes the full range of modulation frequencies presented here, we applied the vector strength decoder to the pooled spike times. Figure 2.3C shows that discrimination on the unprocessed spike times with the vector strength metric is near perfect and completely flat across modulation frequencies. By adding Gaussian jitter with standard deviations of 0.5, 1, 1.5 or 2 ms, the TMTFs take on the behavioral lowpass shape, with greater jitter predicting lower cutoff frequency. Note that jittering best describes the psychophysical curves when the standard deviation is approximately 1.5 and 2 ms. For normal distributions with standard deviation 1.5 and 2 ms, 95% of the distribution falls within 3 and 4 ms respectively; thus the timescale of the optimal jittering is similar to the timescale of the optimal temporal integration window.

We also investigated the relationship between the TMTF and the number of fibers available to the discrimination procedure. Using the max-min decoder, Figure 2.3D shows how stimulus-dependent TMTFs evolve as we fix $\Delta\tau$ = 4.0 ms and vary the number of fibers available to the discrimination procedure. Varying the number of fibers does not have much effect on the cutoff frequency of the TMTF. The main effect of this particular manipulation is to shift the curves up or down on the performance axis on the order of 5 dB. A secondary effect is to sharpen the bandpass quality at 100 Hz: using more fibers gives a more distinct peak at the best modulation frequency.

2.3.2 *MDTs as a function of stimulus intensity*

The effects of stimulation intensity on modulation detection thresholds computed with the max-min rule using 250, 1000 and 2000 pps carrier rates are shown in Figure 2.4, with Galvin and Fu's psychophysical results reprinted for reference. We show the trends with $\Delta\tau =$ 2.5 ms and complete inclusion of fibers; the effects of varying these parameters will be described in the following section. The *x*-axis shows the spike count per stimulus, which increases with stimulus intensity level and is used to indicate loudness perception level. The *y*-axis corresponds to log-transformed modulation depth at the threshold. Thresholds located high on the axis indicate better performance because they reflect successful discrimination of AM/UM stimuli pairs based on progressively fainter amplitude modulation cues.

Across all carrier rates, MDTs generally improve with stimulus intensity. In the range of intensities considered, performance with the 250 pps carrier plateaus: at this level, many of the fibers are spiking maximally (approaching 250 spikes/second) for the 250 pps carrier and very little information can be added. Note that while Figures Figure 2.4A and B show qualitative agreement in the relationships between carrier rates, the scale of the *y*-axes differs.

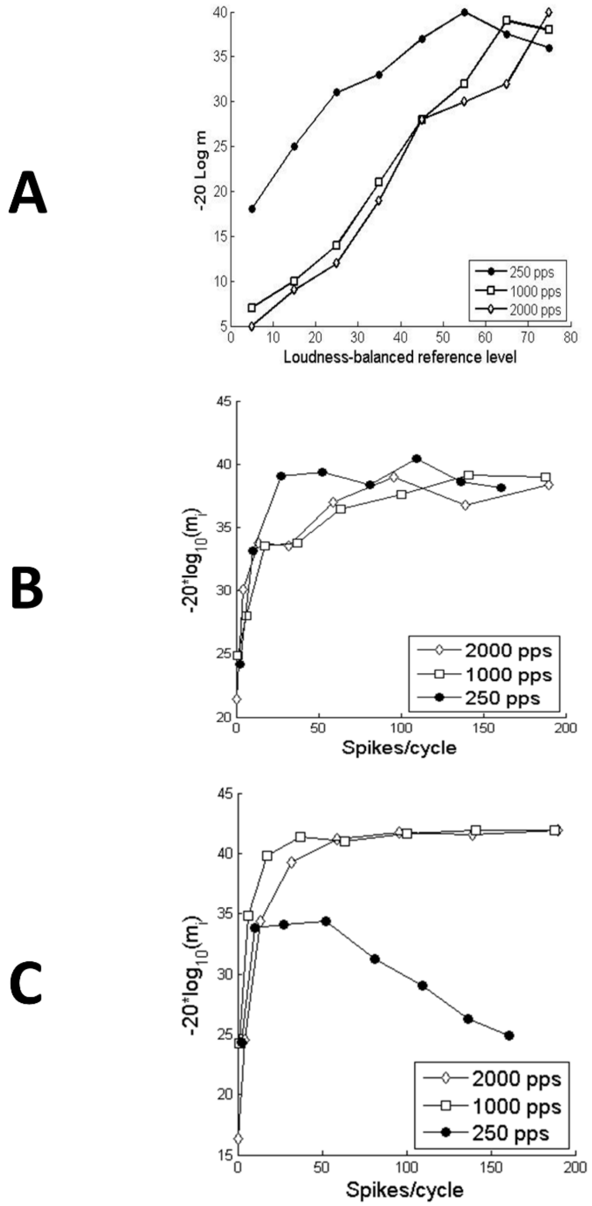

Figure 2.4 Summary of MDT results. (**A**) The mean MDTs of five CI users tested by Galvin and Fu [6] are replotted for comparison. (**B**-**C**) A comparison of MDTs at three carrier rates (250, 1000, and 2000 pps) are shown where stimulus levels are equated by spike count. MDTs are estimated with the max-min rule (**B**) and vector strength discrimination (**C**).

2.3.3 *MDTs and carrier rate*

Consistent with psychophysical results, MDTs estimated with the max-min rule are better at 250 pps than 1000 or 2000 pps for most of the intensities considered. The difference is largest in the lower portion of the intensity range, although at the extremely low end, thresholds are similar. The high carrier pulse rates have no advantage until the top of this intensity range, when MDTs plateau for the 250 pps carrier (compare Figure 2.4A and B). The relationship between curves is consistent with Galvin & Fu's results as well: MDTs for 1000 pps and 2000 pps are close, MDTs for 250 pps are better.

In contrast, when the vector strength rule is applied, the relationship is reversed: MDTs for 1000 pps and 2000 pps outperform MDTs at 250 pps across the entire range (Figure 2.4C). When the vector strength rule was applied to the full population response, MDTs at 1000 pps and 2000 pps were at ceiling levels so Figure 2.4C is computed with 50 randomly selected fibers, which preserves the relationships across carrier rates but does not artificially flatten at the peak MDTs. There is also a compressive effect on the dynamic range (at least for the lowest carrier rate), as the 250 pps curve rises, plateaus and falls over a smaller range of stimulus intensities than in the case of the max-min rule. This suggests that while fluctuations in the population firing rate may be greater for the 250 pps case, they are not necessarily well locked to the modulation frequency.

To investigate this possibility further, we computed the fractional power of the modulation frequency for the population responses at each carrier rate. We presented spike-count balanced stimuli of equal modulation depth using each carrier rate to the auditory nerve population, then lowpass filtered the pooled spike times (third-order Butterworth filter, fc = 300

Hz) to extract a representation of the envelope waveform coded by the population firing rate (Figure 2.5A-C). We subtracted the DC component and computed the discrete FFT for each waveform. The fractional power is the ratio of the FFT component at 100 Hz to the sum of all components. Figure 2.5D shows the fractional power as a function of modulation depth for all three carriers.

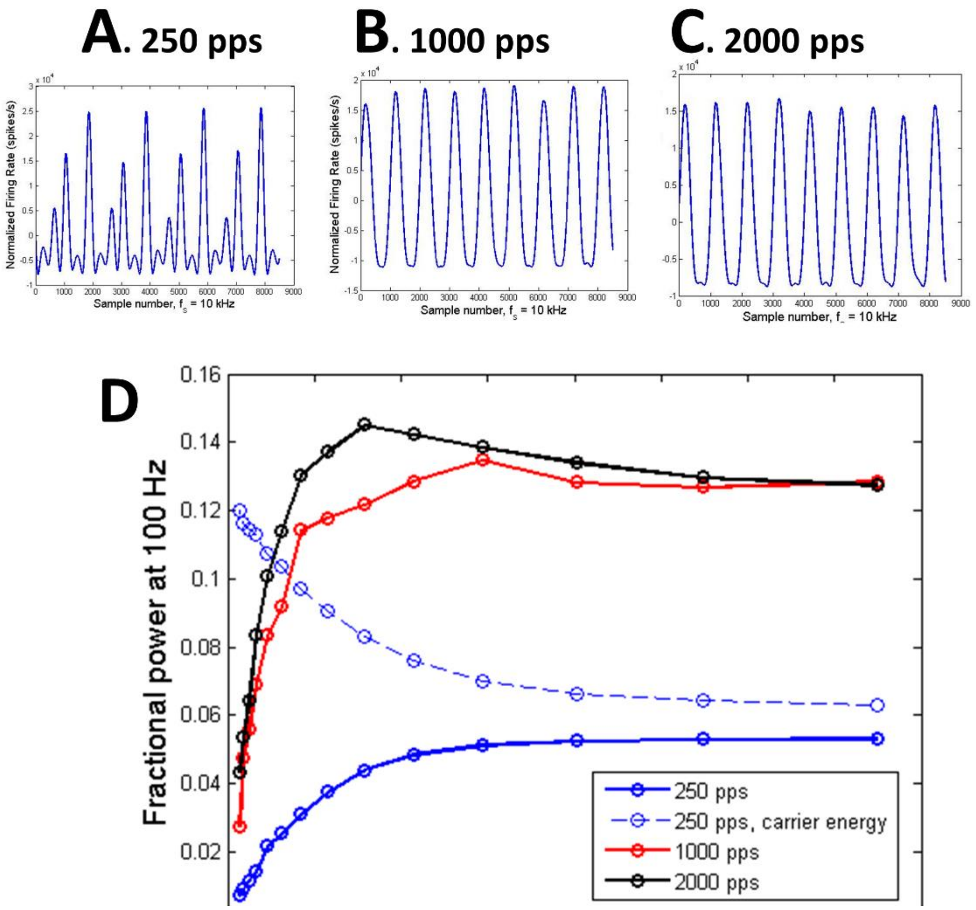

Figure 2.5 Fractional power of the modulation frequency across carrier rates. (**A-C**) The pooled population spiketimes are lowpass filtered (third order Butterworth filter, $f_c = 300$ Hz) to give a reconstruction of the original signal presented at three different career rates. For all carrier rates, a 100 Hz modulation of equal depth is presented; the stimuli are amplitude-balanced to produce identical spike counts across carriers. The stimulus-onset response is removed and the filtered responses have their means subtracted (hence the y-axis is the “Normalized Firing Rate”). (**D**) The proportion of power at the modulation frequency is plotted as a function of modulation depth for all three carrier rates. Additionally, the blue dashed line demarcates power at the 250 Hz carrier rate for the 250 pps signal.

This analysis indicates that across modulation depths, there is nearly three times as much energy at the modulation frequency when the 1000 pps and 2000 pps carrier rates are used than with a 250 pps carrier rate. When the modulation is applied to a 250 pps carrier, the population response has more power at the frequency of the carrier than the modulation frequency itself. This indicates that while low carrier rates may generate more detectable fluctuations in population activity, they may be at a disadvantage when it comes to coding the stimulus envelope.

2.3.4 *MDTs as a function of temporal precision and population size*

We now consider the effects of temporal resolution (manifested by changing $\Delta\tau$) and number of fibers on MDTs as a function of stimulus intensity. In the subplots of Figure 2.6, the *x*-axis shows the stimulus intensity in dB relative to 1 mA. As in previous figures, the *y*-axis corresponds to log-transformed modulation depth at the threshold.

Figure 2.6A-C shows how the stimulus-dependent MDTs evolve if we fix $\Delta\tau$ = 2.5 ms and vary the number of fibers involved in the max-min discrimination task between 25, 50 and 100 fibers. MDTs shown are the average over ten subpopulations for each fiber count condition, in order to ascertain the effects of fiber number on MDT variability. Across all carrier rates, we find that decreasing the number of fibers shifts MDT curves down on the performance axis. The difference in MDTs computed with 25 and 100 fibers was in the range of 7-15 dB across all levels; the magnitude of this relationship is approximately consistent across carrier rates. Additionally, fiber count does not strongly affect the shapes of the curves.

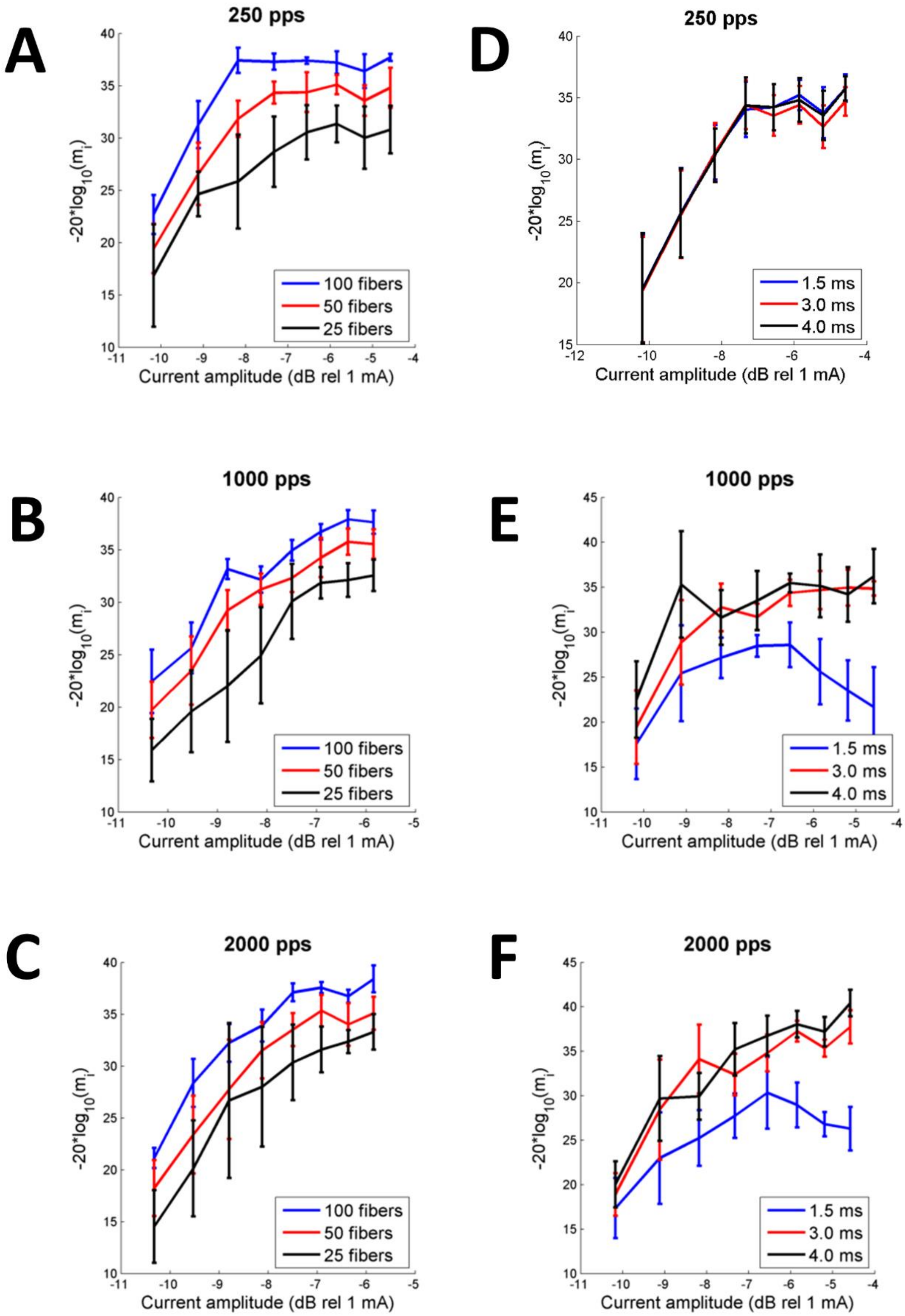

Figure 2.6 Comparisons of MDTS with varied temporal precision and population size.(**A-C**) MDTs as a function of stimulus intensity when the carrier rate is 250 pps, 1000 pps, and 2000 pps respectively using the max-min rule with $\Delta\tau = 2.5$ ms. Each curve shows MDTs computed with a different number or randomly selected fibers; the error bars are the standard deviation of 10 trials. (**D-F**) Comparison of MDTs where the temporal integration window size was varied.

Variability in MDTs is largest when there are the fewest fibers available for the discrimination procedure—in the case of 25 fibers, the standard deviation of MDTs can be on the order of 10 dB, especially at lower stimulus intensities. This suggests that heterogeneity in neural morphology can underlie significant variability in psychophysical trends for individuals with low neural survival, and also indicates that the incorporation of a distribution of fiber diameters and thresholds has a non-negligible effect on the predictions of our model.

Figure 2.6D-F demonstrates how the temporal precision of spike timing affects MDT estimates with the max-min rule. As in the TMTF study, window size $\Delta\tau$ was varied from 1.5 to 4 ms. This manipulation has no effect on MDTs in the low carrier rate condition, which is to be expected because the population response is a series of discrete, nearly synchronous pulses arriving every 4 ms. For the high carrier rates, increasing the window size can actually improve performance. This can be thought of as smoothing out the stochastic fluctuations so that the large scale modulation-driven fluctuations dominate the population activity. At the smallest window size ($\Delta\tau$ = 1.5 ms), MDTs at high carrier rates display a non-monotonicity at higher stimulus intensities. This is a result of a trend exhibited by many fibers to lock to an approximately 500 Hz firing pattern at high stimulus intensities at high carrier rates, which is inadequately smoothed by a very small window.

The relationship between window size and modulation detection at high carrier rates can be better understood by considering the effects of stimulus modulation on population spike count. We computed the difference in number of spikes elicited in the population by modulated and unmodulated stimuli over a range of stimulus intensities (Figure 2.7). At both 250 pps and 2000 pps carriers, modulated stimuli elicit more spikes per modulation cycle than unmodulated stimuli at low stimulus intensities; as stimulus intensity is raised there is a reversal in the relationship. It is worth noting that the reversal point of the trend at 250 pps approximately corresponds to the maximal stimulus intensity used in the simulated MDTs; for higher stimulus intensities we observed falling MDTs at 250 pps.

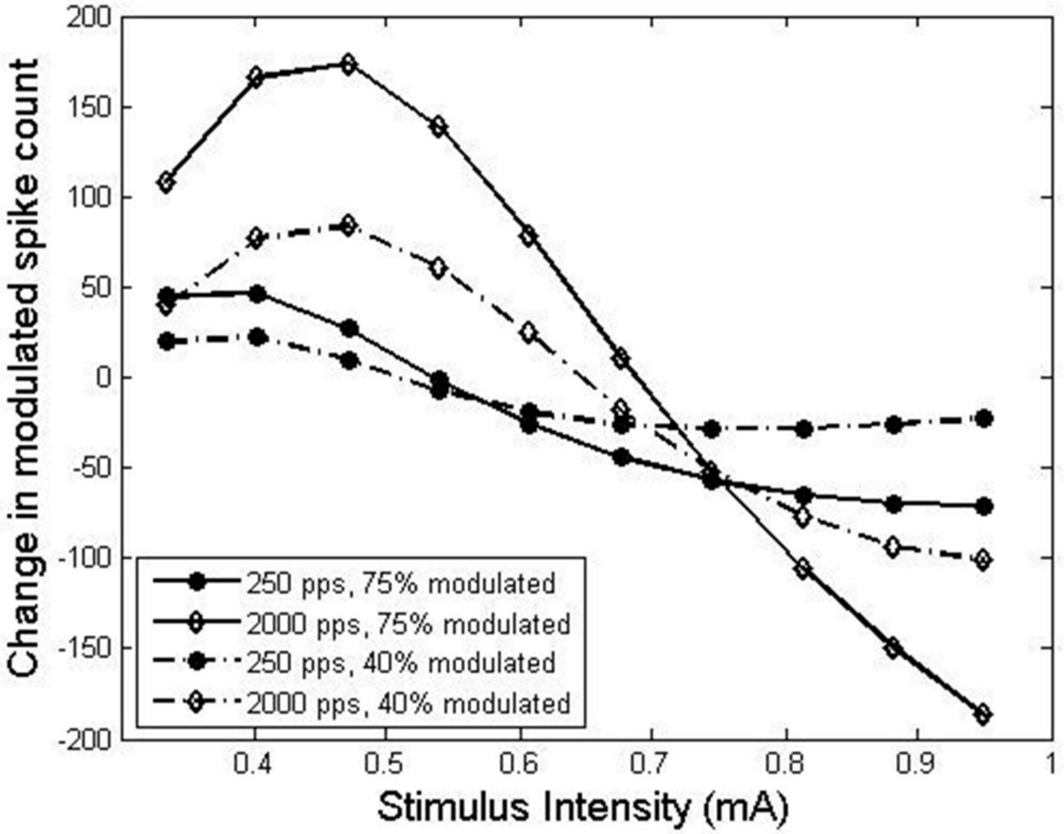

Figure 2.7 Effects of modulation depth on spike count. The difference in spike counts elicited by unmodulated and modulated stimuli with the same average current level is plotted against current. Trends are shown for two carrier levels (250 pps, black dots, and 2000 pps, white diamonds) at two modulation depths (~75% and ~40%).

At all stimulus intensities before the reversal point, and therefore all stimulus intensities in the range studied here, the magnitude of the difference in spike count is greater for the 2000 pps carrier than the 250 pps carrier. This indicates that there is a larger cue in overall spike count at high carrier rates. But spike times are tightly locked at low carrier rates, and high carrier rates show variable spike times that grow more stochastic as the modulation depth shrinks. Thus appropriately large temporal integration windows may enhance the large fluctuations in population activity at high carrier rates.

2.4 DISCUSSION

2.4.1 *Comparing simulations to behavioral data*

The modulation detection thresholds simulated in response to a change in stimulus level and in response to the different modulation frequencies track the discrimination performance observed in cochlear implant psychophysical experiments ([5], [6], [109]. To allow an easy comparison between simulations and behavioral data, we provide the results obtained by Shannon and Galvin and Fu and discuss them below.

2.4.1.1 TMTFs

A comparison of temporal modulation transfer functions in Figure 2.3A and B reveals a close correspondence between modeled estimates and subject data. Due to the wide range of inter-subject variance [5], [110], comparison of our results to those measured during behavioral testing is restricted to qualitative trends rather than the specific threshold values of the particular experiments. It is intriguing that by varying $\Delta\tau$ the cutoff frequency of the TMTF curves can be systematically varied, and by varying the number of fibers involved in discrimination the magnitude of the TMTF curves can be systematically varied. Cazals [135] showed that cutoff frequency is strongly correlated with speech perception. These findings in conjunction with our observations suggest that individual differences in temporal integration could contribute to variability in TMTF cutoff frequency and perhaps even speech discrimination ability.

Nonetheless, despite the differences in MDT limens, subject and model testing both produce a TMTF composed of two segments: one, a relatively gradual decrease in performance, and another, a precipitous drop in performance at modulation frequencies above the cutoff frequency of ≈ 100 Hz [5], [110], [136], [137]. Some of Shannon's subjects have improving thresholds for low modulation frequencies below the cutoff (TMTFs have a band-pass as opposed to low-pass shape, see subject N4 in Figure 2.3A). We predict both lowpass and bandpass curves depending on the choice of temporal integration window size and number of fibers. In Cazal's work, numerous subjects showed flat TMTFs; this can be obtained in our model by using a small temporal integration window (2.5 or 3 ms).

When the vector strength measure of phase locking is considered as a discrimination rule (Figure 2.3C), we find that the auditory nerve fibers, as a population, successfully code the modulation frequency through phase locking up to 350 Hz. This is consistent with numerous electrophysiological studies [44], [138], which found that auditory nerve fibers could lock to both analog and pulsatile sinusoidally modulated electric stimuli in this range of modulation frequencies. Our analysis suggests that the decline in modulation detection at higher modulation frequencies does not occur at the level of the peripheral auditory nerve and represents a more central process. This process is described phenomenologically as jittering the spike times in the vector strength rule or increasing the temporal integration window width in the max-min rule. Jittering spike times is a qualitatively different manipulation than smoothing, though, and each affects TMTF curves differently. Notice that adding jitter to the spike times in the vector strength measure only predicts lowpass TMTFs, whereas adjusting the temporal integration window length in the max-min rule can predict bandpass trends.

2.4.1.2 *MDTs and stimulus intensity*

The mean MDTs of five CI users, as recorded by Galvin and Fu [6], are presented as a function of loudness in Figure 2.4A. Key stimulation parameters used to produce our simulations in Figure 2.4B-C are identical to those used by the experimenters: m_f = 100 Hz and stimulation rate is 250, 1000 or 2000 pps. Juxtaposing the two figures, the reader will see that MDTs generated from the model output with the max-min decision rule mirror the behavioral data (Figure 2.4B): poor discrimination at low stimulus intensities, improving with an increase in intensity to a plateau.

The relationship of stimulus intensity to MDTs is predicted by both the max-min and vector strength rules. This dual analysis indicates two reasons for the trend. First, as stimulus intensity grows, there is better population phase locking to the modulation frequency (although note that in Figure 2.4C, phase locking to the modulation frequency also plateaus and declines for the 250 pps carrier). Second, at higher stimulus intensities, the absolute value of the fluctuation in stimulus intensity is greater for the same modulation depth—a 10% modulation results in larger fluctuations in population firing rate at high than low stimulus intensities. Modulation- driven changes in firing rate are attributed both to fiber recruitment and high firing efficiency in fibers above threshold. Therefore using the max-min decision rule, larger fluctuations in population activity at higher stimulus intensities lead to better discrimination.

An observant reader may notice that MDT simulations at 250 pps in Figure 2.4B and C generally reach a plateau around and remain at the same performance for a range of stimulation levels greater than the range measured in Galvin and Fu’s experiments. We believe this discrepancy is due to the broader range of stimulation intensities employed in our simulations. In the interests of safety and subjects’ comfort, stimulation current in CI experiments was increased only to 75% of the participant’s dynamic range. We did not need to exercise the same caution in our model and, because there is no reliable way to map spiking patterns to a corresponding loudness percept, we continued to increase the stimulus level to ascertain that a plateau had been reached. In fact, our preliminary data indicated that if we had continued to increase stimulation intensity, the spike rate of all the modeled fibers would saturate and the presence or absence of envelope modulation would become impossible to determine. A similar “rise—plateau—fall” pattern of performance has been previously reported elsewhere [94]. We also note that the dynamic range (the range of stimulus intensities between rise and plateau) is smaller for the low carrier rate than either the 1000 pps or 2000 pps carrier rates, which have nearly identical ranges.

2.4.1.3 MDTs and carrier rate

Our model predictions are in decent qualitative agreement with the Galvin and Fu’s subject data when spike count balancing is used to compare stimuli (compare Figure 2.4A and B). In both the model predictions using the max-min rule and the human study, modulation detection is best at the low carrier rate up until a certain stimulus intensity is reached. At this point, performance at the low carrier rate plateaus or drops and is overtaken by the high carrier rate. In both the simulation and psychophysical study, the modulation detection thresholds of the 1000 and 2000 pps carrier rates are nearly identical. Our results suggest that there is a range of intensities in which performance with the high carrier rate would surpass that with low carrier rate, but this regime might be beyond the dynamic range of a cochlear implant. When stimuli were applied with a high carrier rate in the range of spike count balanced levels, very few fibers in the population were firing maximally.

The magnitude of the difference in MDTs between high and low carrier rates effect is strongly dependent on the size of the temporal integration window used in max-min discrimination (Figure 2.6E and F) We conclude that in our model, the 250 pps carrier rate generates larger synchronous fluctuations in instantaneous population firing rate than the high carrier rates for a moderate range of stimulus intensities. However, our analyses of vector strength discrimination and population coding of the modulation frequency indicate that there is a marked disadvantage at low carrier rates for the coding of the stimulus envelope (Figure 2.4C and Figure 2.5D). Thus, while we can demonstrate that a decision rule exists that will mirror the psychophysical trends, we have also demonstrated that a rule based on tracking the stimulus envelope predicts a reversed relationship. Litvak et al. also found enhanced amplitude modulation coding through a firing rate code at high pulse rates [44], but direct comparison is difficult as pulse rates in these electrophysiological experiments were 5000 pps. This suggests that there may be other benefits to the high carrier rate not captured by this particular psychophysical task, such as the ability to discern the time-varying statistics of a natural sound. To this end, it may be telling to apply methods from information theory towards reconstructing the signal coded by the auditory nerve or predicting its statistical properties [99], [139].

2.4.2 *Possible loudness cues*

We observed differences between spike counts for unmodulated and modulated stimuli of the same total current. Upon investigation, we found an intriguing non-monotonic relationship between the change in spike count with modulation and the stimulus intensity (Figure 2.7). At low stimulus intensities, a modulated stimulus elicits more spikes than an unmodulated stimulus. At both carrier rates, approximately halfway through the dynamic range, the unmodulated stimulus begins eliciting more spikes than the modulated stimulus (although the halfway mark is different for each carrier). A similar trend was observed in cat auditory nerve fibers, though with acoustic stimulation [112]. We find that the effect is greater at the higher carrier rate and at greater modulation depths.

Specifically, one way modulation affects spike count is by way of fiber recruitment. Because the stimulus amplitude is modulated up *and* down as a percentage of the average stimulus amplitude, modulated stimuli have higher peak amplitudes than unmodulated stimuli of the same average amplitude. As such, fibers near threshold will be activated by the modulated stimuli but not the unmodulated stimuli when the modulation depth is large, providing a reliable form of information even when temporal resolution is poor. However, at very high average stimulus intensities, there is very little difference in the fiber populations recruited for modulated and unmodulated stimuli due to the log-normal distribution of neuronal thresholds. There is actually a decrement in total spike count in response to modulation as fiber recruitment at the stimulus peaks is insufficient to compensate for decreased activity during the stimulus troughs. All of our simulations were performed in the regime where a modulated stimulus would generate more spikes than an unmodulated one.

This result suggests that in a typical MDT experiment where only unmodulated stimuli are loudness balanced, an additional loudness cue may be present. Additionally, our finding that the 250 pps carrier rate generates larger fluctuations in synchronous population firing rate than higher carrier rates may represent a loudness cue. However, we cannot say how spike count pertains to perception or whether the magnitude of spike count changes predicted would be perceptible at all. McKay and Henshall [140] found that loudness cues were more salient at higher modulation depths using a model for loudness and psychophysical testing, consistent with our results (Figure 2.7). They also found that the effect was greater at low carrier rates, contrary to what we would predict if spike count alone predicted loudness. However, the lowest carrier rate tested was 500 pps, and the modulation rate was 250 Hz. If they found the same trend for the conditions tested here (250 pps carrier modulated at 100 Hz), this may suggest that synchrony of spike times plays a greater role than absolute number of spikes in determining the loudness of electrical stimuli.

2.4.3 *Differences between simulated and psychophysical results*

While our model qualitatively predicts psychophysical trends in MDTs as a function of stimulus intensity, modulation frequency and carrier pulse rate, there are a few ways that it differs from the psychophysical results. Our MDTs computed by the max-min rule reach comparable maximal values (Galvin and Fu and Shannon observe MDTs with up to m_i >40 dB) as well as realistic floor values (~20 dB in the stimulus intensity study, ~10 dB in the TMTF study). However, the difference between carrier rates predicted in our model is less than what what is observed on average in Galvin and Fu’s results. Compare the 6 dB difference predicted here (computed with all fibers and a 2.5 ms temporal integration window) to a maximal difference of nearly 20 dB in Galvin and Fu’s 2009 study. However, Galvin and Fu’s results represent the average of 5 listeners, and there are listeners in their study for whom the difference predicted here is consistent. Additionally, the magnitude of difference across carrier rates is known to vary across cochlear stimulation sites [108]. Exploring parameters such as neural conduction velocity (to simulate demyelination or degeneration) and electrode placement may enhance the differences in our model.

There are a number of other potential reasons for this discrepancy. First, it is important to consider in the interpretation of our results that our ANF model is based on recordings from an acutely deafened feline. Real cochlear implant users, by contrast, are typically derived of sensory input for some time before implantation. Studies of degenerated ANFs in felines show reduced latency and jitter, corresponding to more central spike initiation owing to the loss of the presomatic terminal, decreased frequency following, and abnormal adaptation [68], phenomena which will all affect the coding of amplitude modulated pulse trains especially at higher stimulation rates where frequency following, refractoriness, and adaptation are more influential.

In a range of hearing loss etiologies, the population size will also be decremented, an effect we have considered in a preliminary fashion herein (Figure 2.6A-C). However, our population model does not fully describe the extent of single fiber effects associated with sensory deprivation and neural degeneration, and it would be of great value to correlate various pathological modifications of our model with simulated MDTs in a future study.

A second potential source of discrepancy is that our discrimination procedures (either the max-min or vector strength rules) may not represent the metrics actually used by the central nervous system to classify stimuli on the modulation detection test. Finally, our model does not incorporate intensity discrimination thresholds, which may affect the results the max-min decision procedure. Anytime the max-min ratio was greater for the modulated stimulus an ideal observer was said to have correctly classified it; perhaps some fluctuations would have been too small to have perceptual value.

2.4.4 *Effect of temporal precision*

Interestingly, almost all of the TMTF shapes measured across subjects can be recreated from the simulated spike patterns by varying the temporal integration window parameter in the max-min discrimination procedure. Analysis with temporal integration window size $\Delta\tau = 3.5$ ms resembles the trends observed in electric-hearing subjects N2 and N3 in Shannon's results. Increasing the precision parameter to $\Delta\tau = 4$ ms is results in band-pass-like TMTF curves observed in some instances (*e.g.*, see subject N4 in Figure 2.3A). In contrast, for small windows such as $\Delta\tau = 2.5$ or 3 ms, a nearly flat TMTF results. A nearly flat TMTF has been observed behaviorally [103].

When MDTs are considered as a function of stimulus intensity, we observe that max-min discrimination of the 250 pps carrier condition was unaffected by changes in the size of the temporal integration window up to 4 ms. This robustness suggests a putative advantage of the low carrier rate in individuals with degraded temporal processing. We noted that increasing $\Delta\tau$ from 1.5 to 4 ms improved MDTs for modulations of the 1000 and 2000 pps carrier rates. This results from smoothing local stochastic fluctuations and taking advantage of the large asynchronous fluctuations in total spike count over the course of the modulation cycle.

The best qualitative description of the relationship of MDTs across carrier rates is compatible with a small temporal integration window, such as 2.5 ms. But this same temporal integration window would give flat TMTFs using the max-min rule, and the choice of window size that gives non-flat TMTFs would predict roughly equal performance across carrier rates. This discrepancy suggests either that two separate mechanisms are at work, we have not accurately pinpointed the decision rule used by the central nervous system, or the model has not captured some aspect of the auditory nerve response.

Our temporal integration window shape and length (between 1.5 and 4 ms) does not closely correspond with certain previously published temporal integration windows. McKay and McDermott, for example, used an asymmetric exponential window with an equivalent rectangular duration of 7 ms to study loudness perception [141]. In the original Oxenham and Moore study from which this window is derived, the ERD that best fit subject data ranges from 7 to 10 ms, indicating substantial variability in temporal integration between listeners [142]. Presently, we utilized a Tukey window that consists of a flat center flanked by two cosine window curves, which was selected arbitrarily as a compromise between high temporal acuity and excellent stop-band attenuation (in order to ensure TMTFs that decrease after the cutoff frequency in a range up to 350 Hz). The difference in window shape makes comparisons across studies less direct, but certain inferences can still be made. Although we expected at the outset that a longer window would predict behavioral MDTs better, we found that shorter windows enhanced the difference in performance between high and low pulse rates (Figure 2.6D-F). Because modulations in pulse trains with high carrier rates are associated with a greater increase in population spike rate, although with less synchrony than is observed with low carrier rates (Figure 2.7) longer window lengths actually accentuate fluctuations in population firing rate at high carrier rates. This may be the result of an oversimplification in our model of population coding—if spikes across the population are not universally pooled (and doubtlessly they are not in the real auditory nervous system), the benefit of a longer window length at high carrier rates may not be so strongly observed. Alternatively, the small window length is on the order of the integration time for a single neuron that receives converging input from the auditory nerve. Inferior colliculus neurons, including chopper and ICC cells, have been modeled with excitatory post-synaptic potential time constants on the order of 1-3 ms [117], [143]. Perhaps our short window length is not so closely related to a loudness model as the input to an upstream, coincidence detecting neuron.

2.4.5 *Contributions of fiber subpopulations*

The effect of population modeling is demonstrated by varying the number of the fibers that are used to estimate the discrimination performance. Results from stimulus-intensity and m_f experiments indicate that general trends in MDTs are preserved across a wide range of population sizes. In general, decreasing the number of fibers used to discriminate according to the max-min rule gave worse performance overall, but the shape of the curves and trends in cutoff frequency were robust. In the case of the TMTF, we did note that the bandpass character of the curve could be dulled by decreasing fiber count, but the frequency at which the precipitous drop in thresholds occurred was unaffected.

We also noted increased variability in MDTs with fewer fibers. Certain subpopulations of 25 fibers had better peak thresholds than certain subpopulations with 50 fibers. This suggests the trends in thresholds for an individual cannot predict the state of their neural survival well, but an average across individuals may reveal a more pronounced trend. This result also indicates a potential peril of modeling studies with homogenous fibers- the smaller the population, the more pronounced the effects of heterogeneity. The exact number of fibers needed for precise modeling of neural behavior, however, is task-specific and general guidelines remain to be determined [144], [145].

Although we do not quantify the information carrying capacities of individual fibers here, inspection of the raw spike data (Figure 2.8) demonstrates the range of possible responses to CI stimuli. Conceptually, we can separate neural responses produced by both modulated and unmodulated stimuli into three categories: quiescent fibers, those driven to respond at their maximal rate, and those spiking “normally”. In discriminating AM and UM responses, fibers failing to respond to either of the stimuli and those already driven at their maximal response rate do not aid in the discrimination process. It is the fibers that are spiking normally (in a non-saturated manner) whose spike pattern is altered in response to a change in the envelope modulation. As long as the stimulus levels are strong enough to elicit spikes but weak enough to avoid saturating the response rate, there will be a subset of fibers whose spiking rate will change in response to amplitude-modulated stimuli.

A potential direction for further analysis would be the systematic removal of certain populations- for example, the subset of small-diameter fibers, which are correlated with high thresholds and low spontaneous firing rate in the normal cochlea [146], may be especially susceptible to cochlear neuropathy [147]. Our current results predict that, for spike-count balanced stimuli, low carrier rates make more use of these small-diameter fibers whereas high carrier rates activate fewer, larger fibers (at the cost of higher firing rates on recruited fibers), as is visible in the population spike raster plot in Figure 2.8. Therefore, if these small fibers were truly unavailable for electrical stimulation, we hypothesize that MDTs at low carrier rates would suffer most.

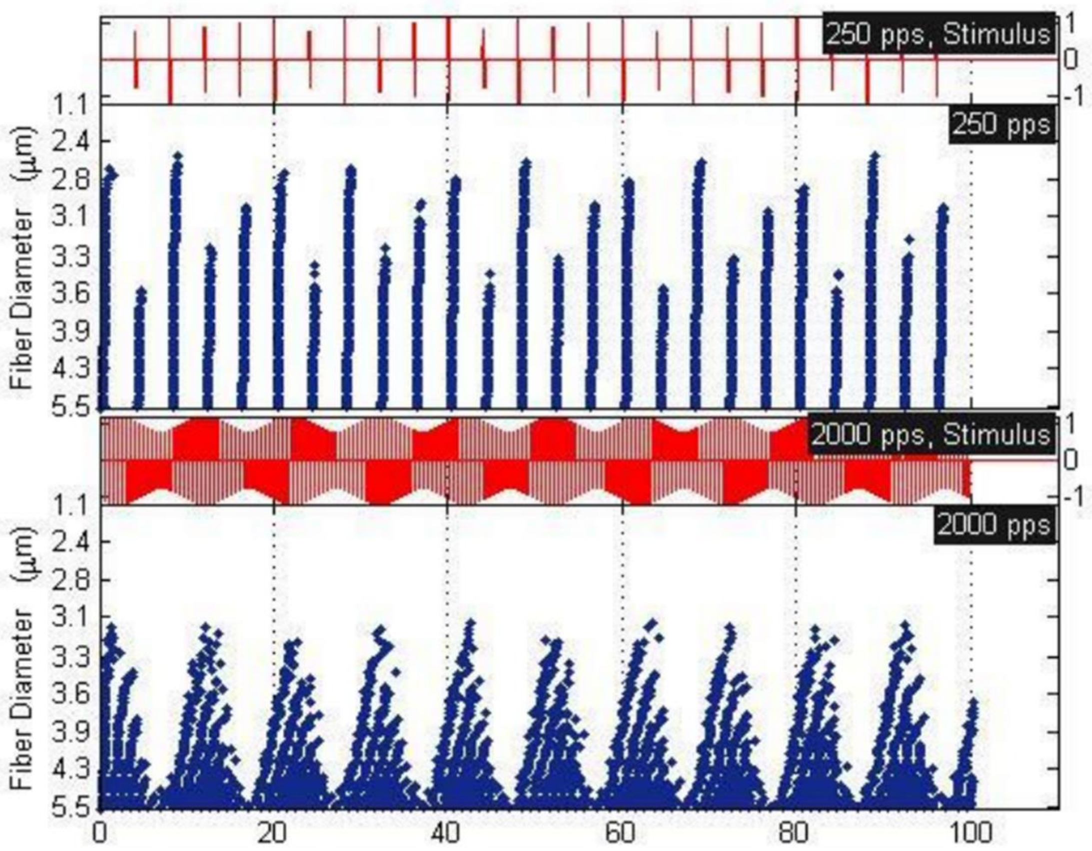

Figure 2.8 Spike time raster plots for 250 pps and 2000 pps. Raster plots are compared for two 100 ms stimuli with identical m_f and m_i but different carrier rates. The stimuli are loudness balanced in that unmodulated stimuli of the same average level elicit the same number of spikes.

2.4.6 *Summary*

A biophysical model of an auditory nerve fiber population has successfully simulated modulation detection thresholds as a function of stimulus intensity and frequency of modulation. The overall shape of the simulated curves corresponds to the trends observed across CI listeners during behavioral testing. Our results demonstrate the importance of using multi-fiber population models to capture listeners' performance on amplitude modulation tasks and suggests that performance on the modulation detection task may not be predictive of the quality of stimulus envelope coding by the population.

Acknowledgements

This work was facilitated through the use of advanced computational, storage, and networking infrastructure of the Hyak supercomputer system, supported in part by the University of Washington eScience Institute. This work was supported by NSF grant DGE-1256082 and an educational gift from Advanced Bionics.

Chapter 3. MODELING PATHOLOGY OF THE AUDITORY NERVE AT THE POPULATION SCALE

Chapter summary

In theory, comparing the neural coding deficits associated with different cochlear pathologies could inform the development of new cochlear implant stimulation strategies optimized for individual listeners. Computational models, in conjunction with histological and electrophysiological studies in the wet lab, can improve our understanding of the relationship between neural health and electrotonic response. Using a previously published biophysical, computational model of a population of auditory nerve fibers (ANFs), we demonstrate the effects of various pathological modifications on single-fiber and population-scale responses. Specifically, we simulate three distinct pathologies: widespread, indiscriminant loss of ANFs, selective neuronal death by fiber diameter (characteristic of acoustic overexposure), and degeneration of the ANF periphery while sparing the central axon.

3.1 INTRODUCTION

From an information-theoretical perspective, the maximal amount of information about an external stimulus a cochlear implant listener can access is contained in the firing pattern of the auditory nerve. As such, the temporal and probabilistic properties of the auditory nerve will constrain the neural representation of a given stimulus [148]. Consequently, pathologies that affect the morphology, electrical properties, stochasticity, and number of auditory nerve fibers will be expected to influence the information capacity of the auditory nerve.

It is not yet clear exactly how specific etiologies of hearing loss relate to neural coding, although duration of deafness and residual hearing do correlate with performance [149]–[151]. Histological studies of chronic sensory deprivation indicate that over time, the periphery of the nerve fiber degenerates, eventually followed by the cell soma and central axon [152]. Therefore, some association can be made between the outcome of implantation and the state of the auditory nerve. More recently, the mechanisms of cochlear damage relating to acoustic overexposure have been elucidated. Although the hair cell is destroyed in most forms of noise-induced hidden hearing loss, the hair cell is spared in “hidden hearing loss”, in which certain auditory nerve fibers are lost without a corresponding long-term shift in threshold. In this particular paradigm, the peripheral dendrite of the synapsing auditory nerve fiber degenerates promptly after acoustic overexposure [88], [89]. A few weeks to months later, the central axon is lost. Acoustic overexposure preferentially culls small diameter fibers with high thresholds and low spontaneous rate, which is thought to degrade the quality of neural coding for time-varying, complex sounds [91].

Biophysical models of the electrically stimulated auditory nerve are especially suited for the study of cochlear pathology for a few reasons. First, it is straightforward to implement morphological changes, like demyelination, in part or all of the axon with a biophysical cable model, where many anatomical features have a corresponding parameter. Second, morphological changes including the degradation of the peripheral dendrite are associated with spatial effects, including more central spike initiation [68]; such phenomena are more directly studied in a cable model with an extracellular electrode than a phenomenological one. In fact, any model in which the current is directly injected instead of propagated through an extracellular potential field will gloss over the interaction between morphology and current spread. Third, a model of a heterogeneous population, incorporating a realistic range of fiber diameters and thresholds, is required to simulate the effects of losing specific subsets of neurons, like small diameter fibers. Finally, the precision of computational models allows for exquisite control of all parameters, thus the effects of varying certain morphological or population parameters can be ascertained unambiguously. Of course, proper validation with electrophysiological studies are required of even the most detailed models for maximal usefulness.

There have been a number of biophysical modeling studies targeted towards the study of cochlear pathology. Cartee studied refractoriness and summation in a cable model of a central axon; although this study makes no explicit attempts to model a known pathology it effectively describes an auditory nerve fiber (ANF) sans peripheral dendrite [14]. Briaire and Frijns simulated the loss of the peripheral dendrite in a uniform population of ANFs, combining a detailed and morphologically realistic ANF model with a three-dimensional volume conducting model of the cochlea [15]. The intention of their study was to optimize the location of a monopolar-stimulating electrode in a degenerated cochlea. In classical cable modeling literature, it is common to vary parameters such as the myelin thickness to simulate the effects of demyelination [7], [20], [75], and this was done in Colombo and Parkins landmark squirrel monkey auditory nerve model [21]. But in the years since that 1987 study, popular biophysical models of the ANF have evolved to include more realistic kinetics, ion channel densities, and electrical parameters [1]. It is certainly relevant to revisit the classical paradigm with more recent models.

In this chapter, we consider the effects of three distinct pathological manipulations of a previously-published biophysical model of the auditory nerve. First, we develop a model of peripheral degeneration and establish single fiber measures, including latency, jitter, and a probabilistic metric. Then, we investigate three population-scale models of pathology: a population in which fibers are removed at random, a population in which fibers are removed in order of diameter, and a population in which all fibers are peripherally degenerated. To our knowledge, this is the first systematic investigation of population-scale effects of degeneration in a heterogeneous model of the auditory nerve. We find that the population metrics of latency, jitter, and dynamic range are distinct in each of the three simulated pathologies.

3.2 METHODS

3.2.1 *Single fiber degeneration study*

3.2.1.1 *Modeling demyelination*

Although we wish to study the effects of auditory nerve degeneration at a population scale, we must first develop a single fiber model of degeneration to be simulated in parallel. We have previously published a model of the electrically-stimulated auditory nerve in which measures such as jitter, latency, chronaxie, relative spread, threshold, and refractoriness are in close agreement with published values of the acutely-deafened feline [16]. For further details, we invite the reader to refer back to the methods section of Chapter 2.

Doubtlessly degeneration is a complex phenomenon involving numerous cellular changes from the molecular to the morphological level, and we consider a very preliminary modification of our control model presently. Specifically, simulated demyelination is the proxy for degeneration of the ANF.

For the single fiber study, a 1.5 μm diameter fiber was considered. The stimulating electrode was placed over node ten, at a distance of 3 mm from the cable. Although it is not physiologically realistic that the electrode would be directly over the tenth node—as the periphery of the ANF is approximately 5 nodes long in humans and 3 in cats [153]—a more central placement on the axon mitigates terminal effects observed in finite-length cable models [123].

To simulate degeneration, we followed the conventions of previous cable model simulations [75], [154] to relate myelin thickness explicitly to electrical parameters of the internodal membrane. Specifically, the membrane resistance and capacitance was determined for internodal segments of the cable model as follows:

$$\mathrm{C_m} = k_1 \left(\log \frac{D}{d}\right)^{-1}$$

Where d is the axon diameter, D is the total myelinated fiber diameter, and

$$k_1 = \left(1.45 \times 10^{-10} \frac{nF}{mm}\right) \log(0.6^{-1}).$$

Similarly,

$$\mathrm{R_m} = k_2 \log \frac{D}{d}$$

Where

$$k_2 = \frac{1254 \times 10^{6}\ \Omega * mm}{\log(0.6^{-1})}$$

The ratio of D to d is called the g-ratio, and in myelinated fibers, it is generally observed to be a constant value of 0.6 [72]. Readers can confirm that when the g-ratio of a simulated fiber is exactly 0.6, the terms of the above equations cancel such that $\mathrm{R_m}$ and $\mathrm{C_m}$ take on their default published values of 1254×10^{6} Ω mm and 1.45×10^{-10} nF/mm, respectively. Whenever the g-ratio is greater than 0.6 (corresponding to the case when the myelinated fiber diameter is closer to the axon diameter, and thus myelin is thinner than normal), $\mathrm{R_m}$ will decrease and $\mathrm{C_m}$ will increase. It should be noted that in the given model for demyelination, both $\mathrm{R_m}$ and $\mathrm{C_m}$ vary in proportion—thus their product, the membrane time constant τ, is fixed.

3.2.1.2 Anatomical considerations of degeneration

Historical models of demyelination in cable models have often treated the length of the cable uniformly. However, in light of evidence that the ANF periphery may degenerate before the central axon, we sought to explore the effects of partial demyelination.

To this end, we compared two distinct anatomical models of degeneration. In the *totally degenerated* model, every internode is manipulated equally. The g-ratio of for every internodal compartment of the cable is set to 0.95, which describes a 90% reduction in myelin thickness from the control. Although we observe this manipulation to greatly decrease conduction velocity, salutatory conduction is still observed. In the *peripherally degenerated* model, only the first fifteen internodes are treated (Figure 3.1). The location of the boundary between degeneration and health, after the first 15 internodes, is not intended to exactly describe any particular pathology. The position is motivated by human anatomy: because the electrode is situated over node 10, and there are approximately 5 internodes in the human ANF periphery, this configuration effectively describes the maximum distance an electrode might be situated from a central axon. An astute reader may be concerned as to why we are imposing human anatomy on a feline model of the ANF; it should be noted that the feline peripheral dendrite is only approximately 3 internodes long, which may cause an underestimation of the magnitude of the effects of peripheral degeneration relevant to humans.

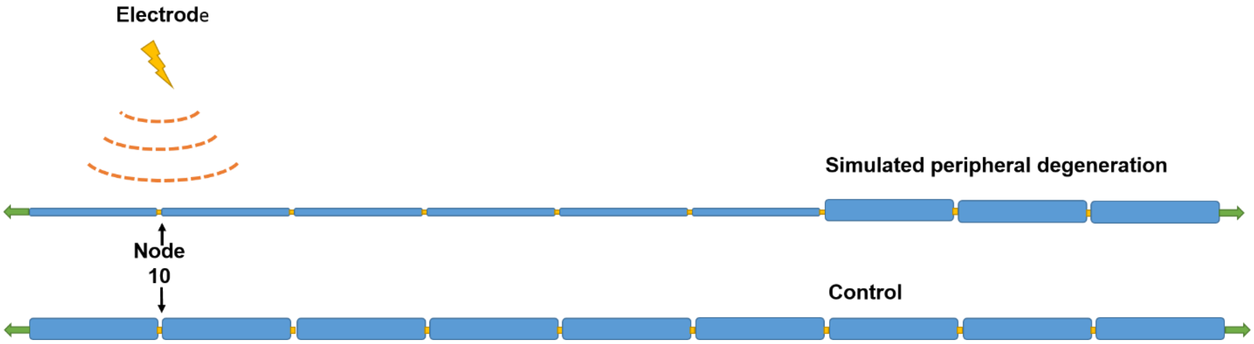

Figure 3.1 A schematic of the peripheral degeneration model. Blue segments represent internodes and their thickness represents the diameter of the myelin wrapping. Yellow segments represent nodes, which are of uniform diameter and electrical properties throughout. Green arrows at the ends of the cable indicate that the model continues in the peripheral (left) and central (right) directions.

3.2.2 *Population models*

We considered the population response to a given stimulus for three models of auditory nerve pathology. In the control population, fiber diameters are drawn from a Gaussian distribution centered at 2 μm with a standard deviation of 0.5 μm (visualized in Figure 3.2A). This approximates the distribution of fiber diameters observed in healthy feline auditory nerves [123]. Fiber threshold varies with diameter, and we have confirmed previously that the log-normal distribution of thresholds in our population closely matches the feline distribution [16]. We simulated a population 30,000 ANFs by choosing 300 fibers from the diameter distribution and simulating each 100 times per stimulus.

Three unique pathological modifications were explored. In the first, which we will denote the Random Die-Off (RDO) model, fibers were chosen at random to be removed from the population (Figure 3.2B). In another manipulation, called the Diameter Die-Off model (DDO), fibers were removed in order of diameter from smallest to largest (Figure 3.2C). Thus "25% loss" should be interpreted that the top 25% smallest fibers have been culled from the population. In both the RDO and DDO models, normal fibers from the previously published model were used (not the new model of degeneration outlined in the previous section). Finally, we considered a degenerated population model (DP), in which the single fiber study of degeneration is generalized to the whole population. The distribution and number of fibers are unchanged from the control case, but each fiber is 90% demyelinated.

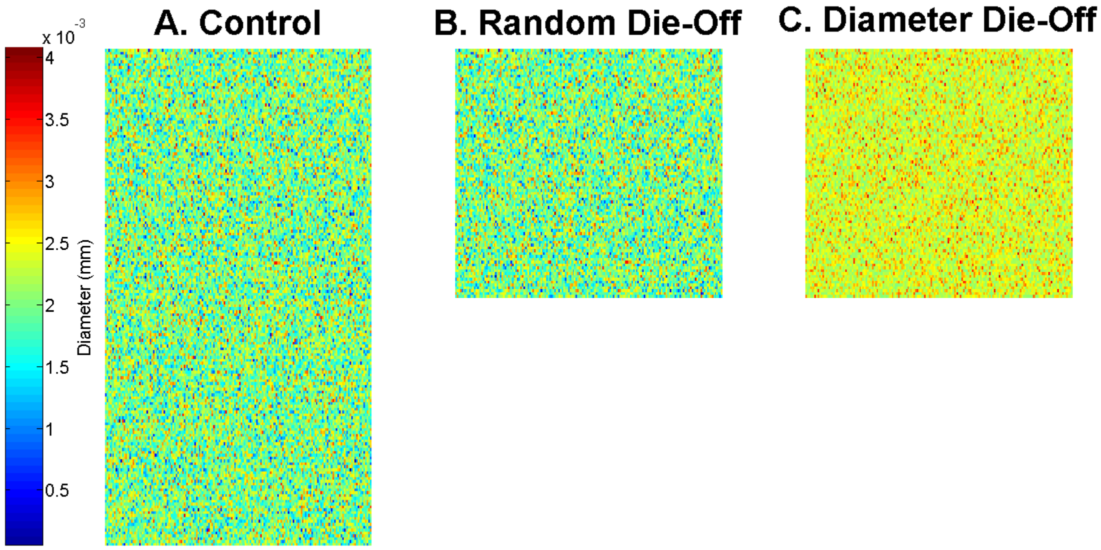

Figure 3.2 A comparison of two population-scale models of auditory nerve pathology.(**A**) The diameters of approximately 30,000 simulated ANFs (drawn from a Gaussian distribution matched to the distribution of healthy feline auditory nerves) are visualized. (**B**) In the Random Die-Off model, fibers are selected at random to be removed. Here, 50% loss is shown. (**C**) In the Diameter Die-Off model, fibers are culled in order of increasing fiber diameter. Again, 50% loss is shown.

3.2.3 *Stimulus*

The electrical stimuli used for population and single-fiber studies were biphasic, charge balanced current pulses, a common stimulus for electrophysiological studies [45], [68], [122]. Each phase lasted 100 µs and there was no interphase gap. The stimulus waveform occurred only once per presentation. We varied the leading phase (anodic or cathodic) at times to investigate spatial effects and spike initiation site. Therefore the order will be specified with each result.

3.2.4 *Measures of neuronal response properties*

Following the protocol of electrophysiologists, we computed various measures of neuronal responses in order to make comparisons across pathological models. In order to prevent confusion of metrics traditionally consigned to single fiber models with population scale measures, we have coined alternate terms for the two cases as we deemed necessary.

Firing efficiency is the probability of a given stimulus eliciting a spike in a single fiber. It was computed by calculating the percent of trials at a certain intensity the fiber was elicited to spike. So as not to confuse the single fiber measure with its population analogue, the corresponding metric for the population is called *recruitment efficiency*. It is computed after pooling the spike counts across all fibers and trials for a given stimulus intensity. Because each trial corresponds to a fiber (recall there are 300 fibers simulated 100 times to represent 30,000 fibers), this measure reflects what percent of fibers in the entire auditory nerve are recruited to fire by a given stimulus.

Threshold is the stimulus intensity at which the probability of generating a spike in a single fiber is 50%. In the population, it refers to the stimulus intensity at which recruitment efficiency is at half its maximal value.

Latency is defined as the average interval between stimulus presentation and spike time. For the population model, all spikes across all fibers were pooled before computing the average latency for a given stimulus intensity. When we refer to latency in tables, it is the value at threshold.

Jitter is the standard deviation of spike times relative to the stimulus onset. Just as with latency, all spikes across all fibers were pooled in the population model to generate a whole-nerve estimate of jitter. When we refer to jitter in tables, it is the value at threshold.

Relative spread is a measure of stochasticity in single fibers. It is computed by fitting a cumulative Gaussian function to the input-output function of a given fiber; the relative spread is the standard deviation of this distribution. *Slope* is the analogous quantity for the population input-output function. There is one crucial difference: owing to the log-normal distribution of thresholds in the population, the input-output function is best not to a cumulative Gaussian, but a cumulative log-normal Gaussian (MATLAB function `logncdf`).

3.3 RESULTS

3.3.1 *Single fiber modeling*

We compared firing efficiency, latency, jitter and relative spread for three single fiber models: a control, a peripherally degenerated fiber, and a totally degenerated fiber. First, we examined the differences in firing behavior with a stimulus (Figure 3.3).

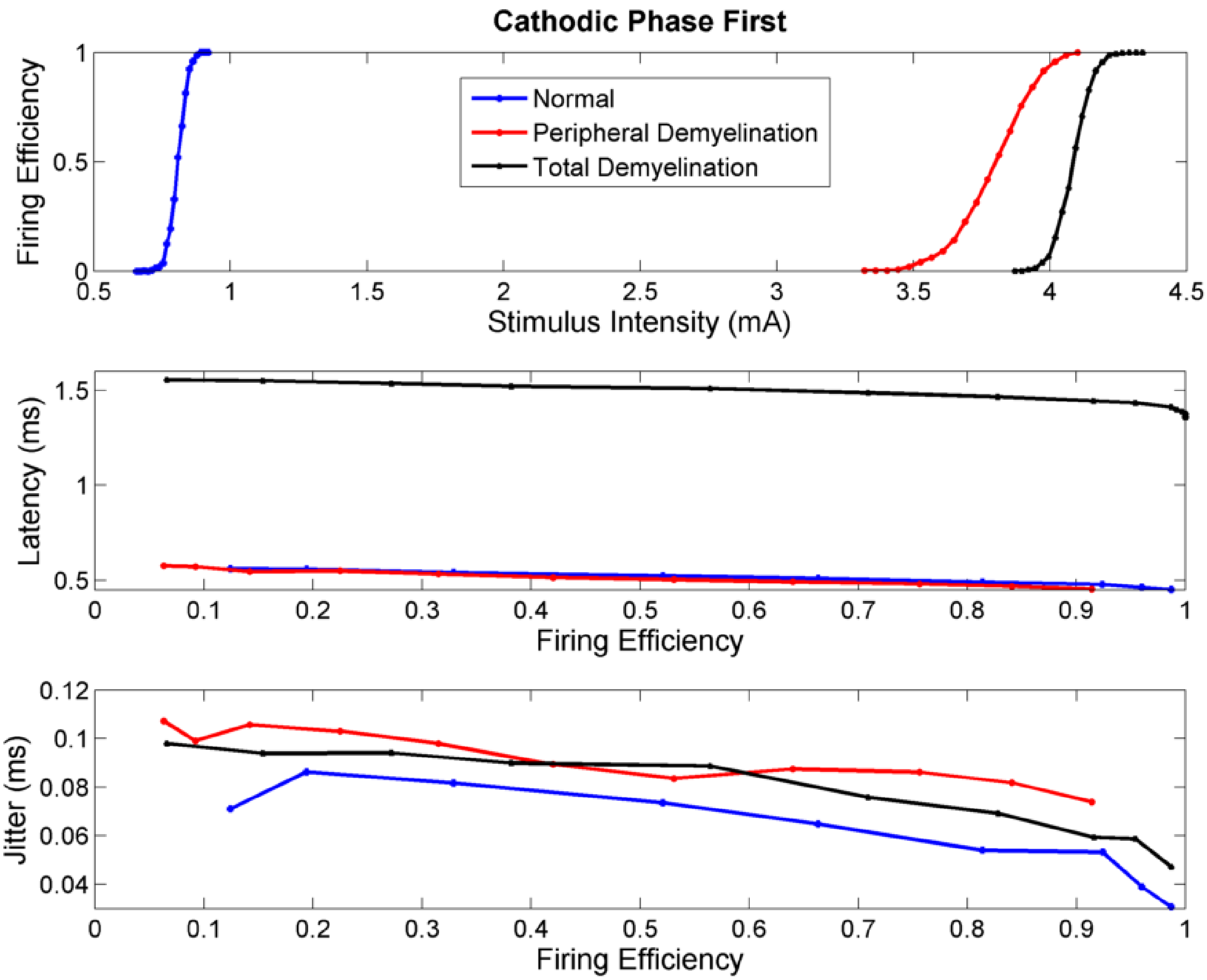

Figure 3.3 Comparison of input-output functions, latency, and jitter across the dynamic range of three single fiber models. Blue curves denote measurements for the control fiber, red is the peripherally demyelinated fiber model, and black is the totally demyelinated fiber.

The jitter, latency, threshold and relative spread for each model is summarized in Table 3.1. When a biphasic cathodic first (CF) stimulus is presented, both the peripherally (PD) and totally demyelinated (TD) fibers have higher thresholds and greater relative spread than the control. For the PD fiber, threshold is slightly lower and relative spread is greater than for the TD fiber. For all fibers, latency decreases as a function of FE. In measurements of latency computed at threshold stimulus levels (50% FE), the PD fiber latency is 10 µs less than the control. The TD fiber, on the other hand, has a latency nearly 1 ms greater than the control. As we will see shortly, this effect is solely attributable to the decreased conduction velocity of the TD fiber and not a change in spike initiation site. In measurements of jitter, which generally decreases over the dynamic range of a fiber, the lowest values are observed for a normal fiber. Both the PD and TD fibers have similar jitter at threshold. There is a slight non-monotonicity in the PD model near 60% FE, which is the result of two spike initiation sites emerging. At sufficiently high stimulus intensities, a small number of spikes can be observed on the degenerated periphery. The number of peripherally-originating spikes increases with stimulus intensity, which complicates the jitter curve.

Table 3.1 Single Fiber Measurements for a Cathodic Phase First Stimulus

	Jitter (ms)	**Latency (ms)**	**Threshold (mA)**	**Relative Spread**
Control	0.074	0.52	0.82	0.0319
Partially Demyelinated	0.084	0.51	3.808	0.1397
Totally Demyelinated	0.094	1.5	4.0846	0.0619

In Figure 3.4, we compare histograms of spike initiation site at threshold levels for all three fibers. In the control and TD models, spikes are generally initiated locally to the electrode, at node 10. Notably, there is much less variability in spike initiation site for the TD model than the control, although the TD fiber is more jittered across its dynamic range. This observation suggests that both the high latency and jitter of this fiber are results of altered propagation dynamics in the TD model, not shifts in spike initiation site. In the PD model, on the other hand, spike initiation at threshold is clustered around the 27th node. This indicates that the PD fiber, in the middle of its dynamic range, is driven to spike by the anodal phase of the stimulus only, which depolarizes distant regions of the axon. In light of this, the PD model's true latency is 100 μs shorter than we compute by our metric, because the excitable phase of the stimulus is delayed by the 100 μs long cathodic pulse.

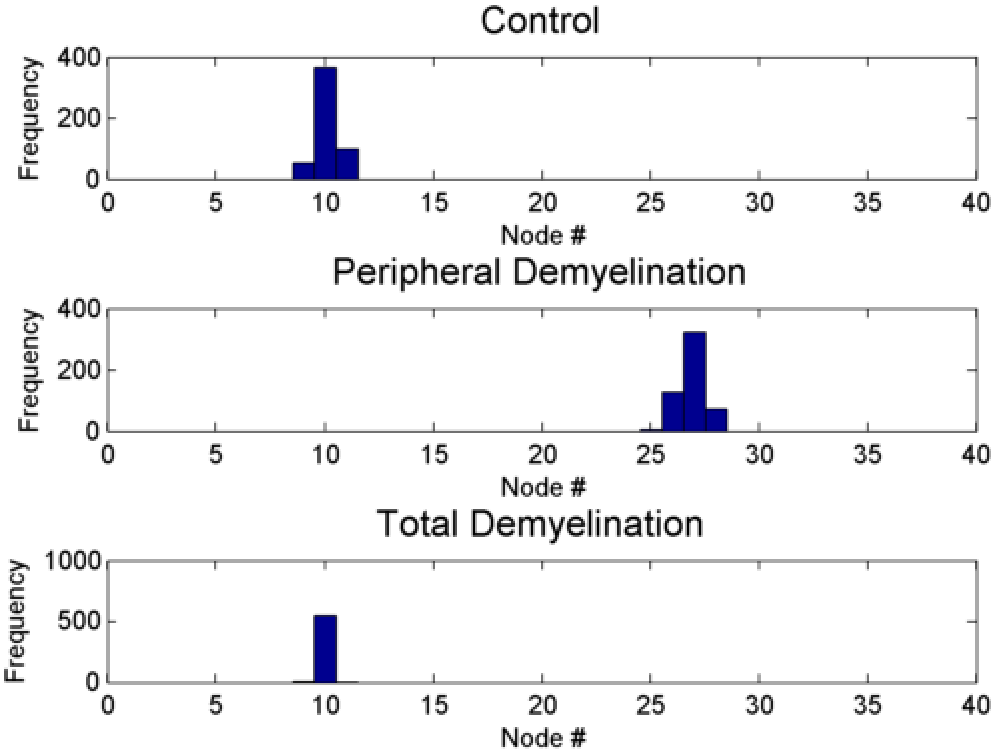

Figure 3.4 Spike initiation histograms for three single fiber models presented with a threshold-level CF stimulus. Node 0 is the peripheral termination of the axon; higher node indices indicate more central placement.

Next, we consider the effects of anodic-phase first (AF) stimulation (Figure 3.5). We find that the input-output functions for the control and TD fibers are shifted up with concomitantly high thresholds, but surprisingly, the PD fiber trends in the opposite direction. Its threshold is actually *lower* for AF stimulation than CF. This reversal can be understood in terms of the spatial features of the two phases. When a CF stimulus is presented, distant parts of the axon will be temporarily hyperpolarized—in the PD model, these central regions are more likely to be excited to spike than the degenerated region local to the electrode. In order to fire on the anodic phase of the stimulus, the initial hyperpolarization induced by the cathodic phase in the spike-generating central axon must be overcome. When an AF stimulus is presented to the PD fiber, on the other hand, there is no preceding hyperpolarization of the central spike initiation site, and so threshold is lower.

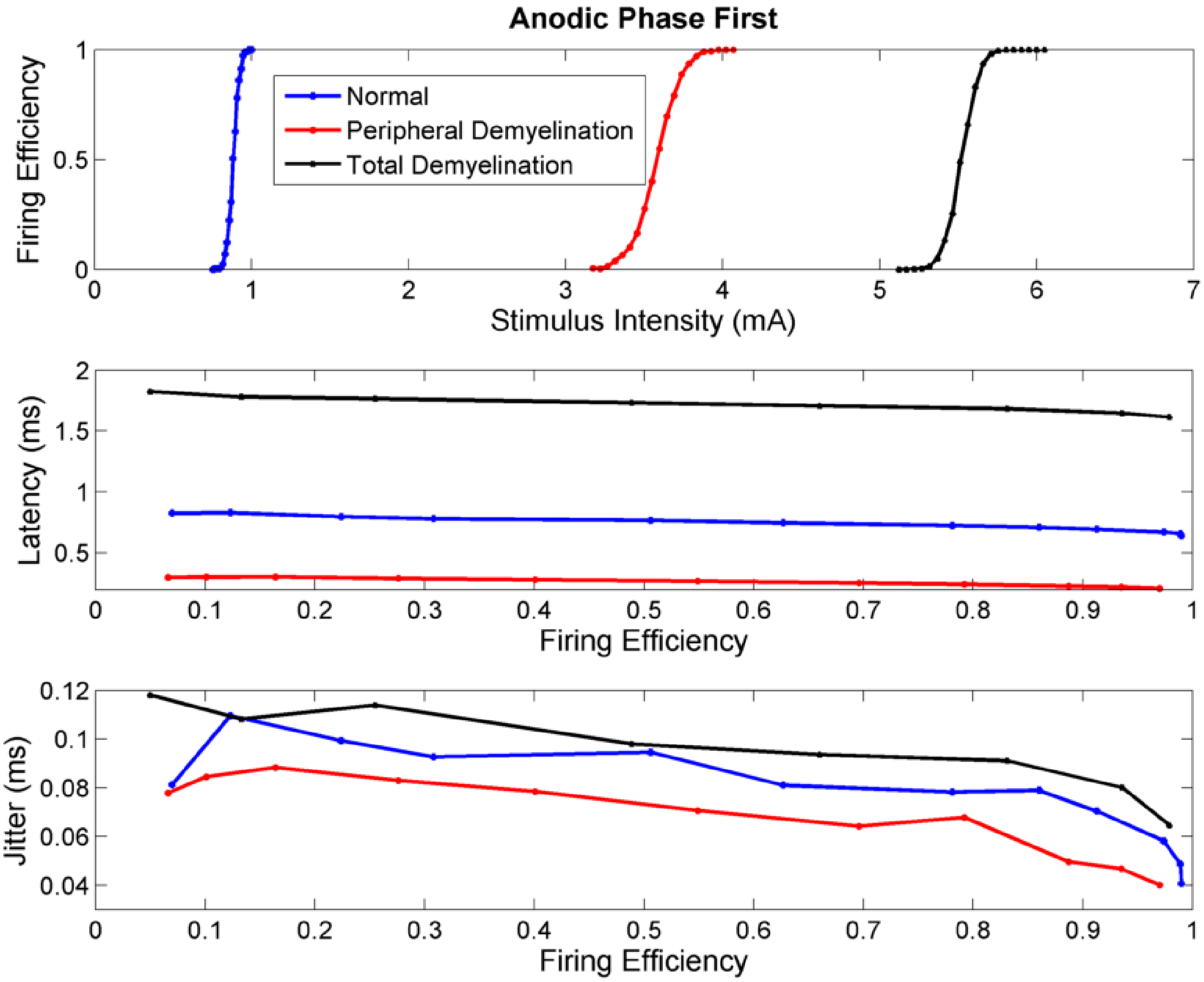

Figure 3.5 Comparison of input-output functions, latency, and jitter across the dynamic range for three models presented with AF stimulation.Blue curves denote the control model, red the partially demyelinated model, and black the totally demyelinated model.

A summary of measured values for each model is presented in Table 3.2. We find most strikingly that in AF stimulation, the effects of degeneration on latency and jitter are especially pronounced. In the PD fiber, for example, latency is 50 µs less than the normal fiber at threshold (compared to a 10 µs difference in CF stimulation). Just as in the case of CF stimulation, the TD fiber still has the longest latency by more than a millisecond, and again we will confirm that this is due to sluggish conduction velocity down the length of the entire axon. For measures of jitter, the lowest values are observed across the entire dynamic range for the PD model; the control and TD models have nearly identical jitter at threshold.

Table 3.2 Single Fiber Measurements for an Anodic Phase First Stimulus

	Jitter (ms)	**Latency (ms)**	**Threshold (mA)**	**Relative Spread**
Control	0.095	0.77	0.89	0.034
Partially Demyelinated	0.074	0.27	3.58	0.133
Totally Demyelinated	0.097	1.7	5.52	0.0929

Considering the spike initiation site histograms (Figure 3.6), we note that again, the TD and control fibers are predominantly excited local to the electrode at node 10. This indicates that both are excited to spike by the cathodic phase of the stimulus, whereas the PD fiber is excited by the anodic phase. Compared to the histograms for CF stimulation, there is less variability in spike initiation site for the PD fiber, which is in accord with the relatively low levels of jitter observed.

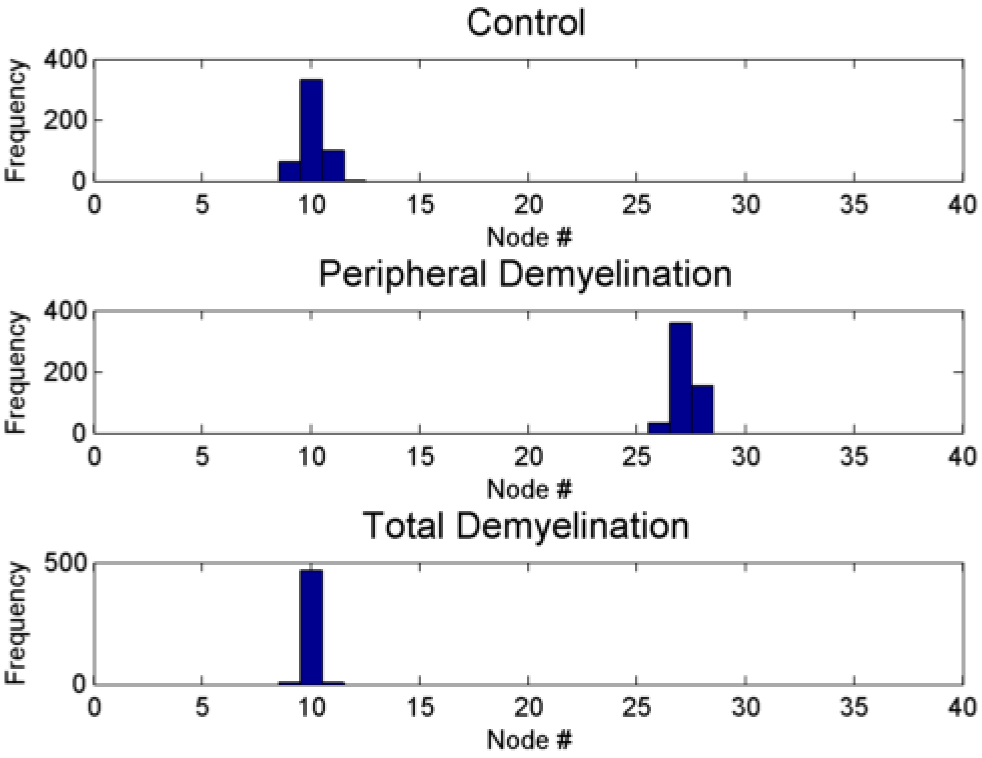

Figure 3.6 Spike initiation histograms for three single fiber models presented with an AF stimulus. Node 0 is the peripheral termination of the axon; higher node indices indicate more central placement.

3.3.2 *Population studies*

Our intention in the previous section was to lay the groundwork for a population model of degeneration by simulating demyelination in a single unit. We considered two models of demyelination, one in which the whole axon is treated and one in which only the periphery is affected. In terms of latency, jitter, spike initiation site and sensitivity to stimulus polarity, the two models are quite different and certainly not interchangeable. Thus, based on its ability to replicate central spike initiation and more physiological values of latency and jitter, we will continue to the population-scale simulation using the PD model. Because we observed the most dramatic differences between the PD and control fibers with AF stimulation, we used AF stimulation for all population studies.

As the first of three population models to be considered, we computed the input-output curves, latency, and jitter of a population of 30,000 PD models of various diameters (Figure 3.7).

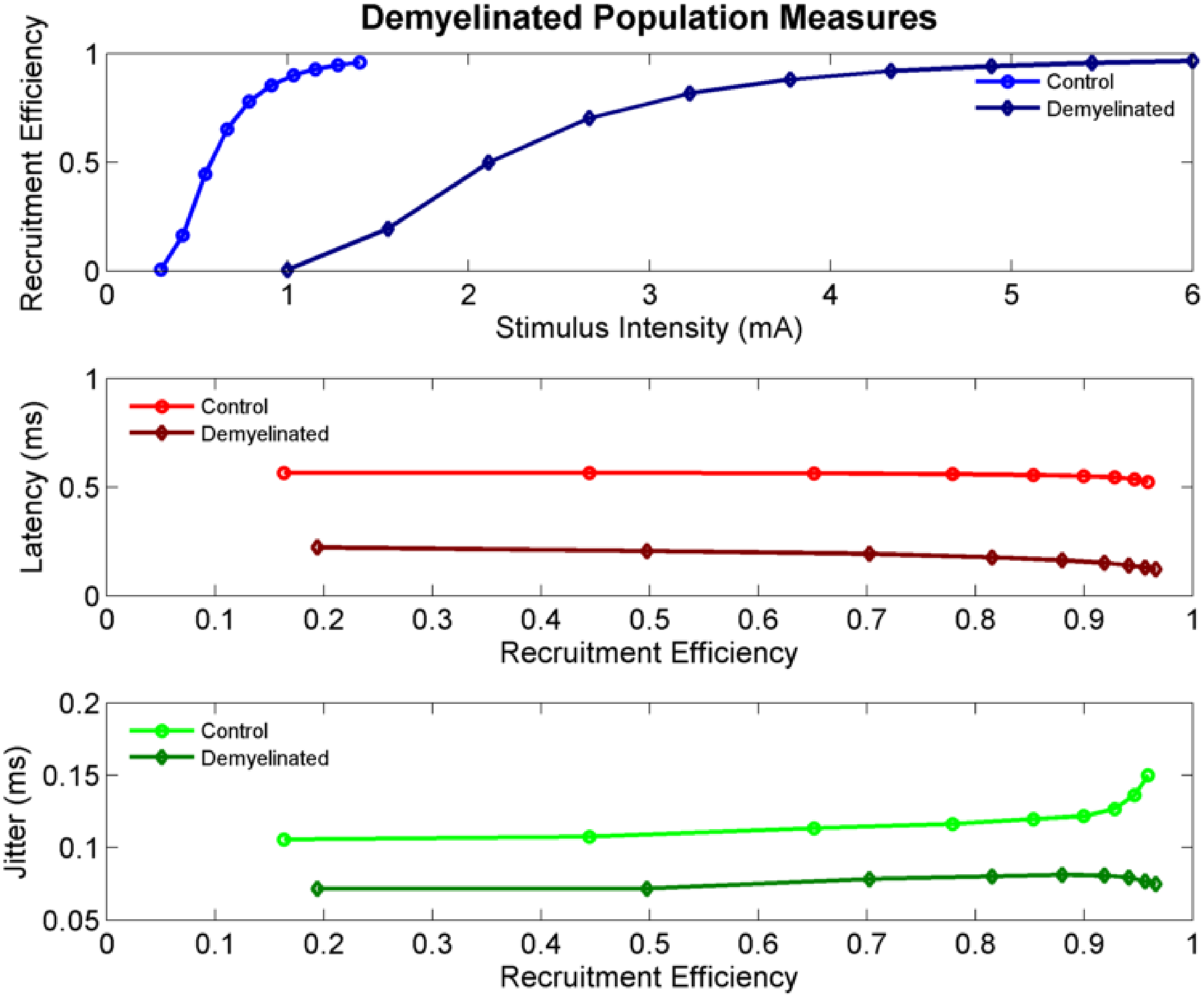

Figure 3.7 Input-output functions, latency, and jitter across the dynamic range of a population of partially demyelinated ANFS.

We observe major differences in the slope of the demyelinated population input-output function and that of the control population—compare 0.4386 to 0.3933 (recall that this is the analogue of the relative spread metric for a population, and is the standard-deviation of a cumulative log-normal Gaussian fit to the input-output function). In terms of latency, values differ between the control and deymeylinated population by nearly 0.5 ms across the dynamic range, with lower latency associated with the demyelinated population. Jitter is also lower across the dynamic range, most strikingly at the upper end—jitter for the control population actually trends upwards. This is a result of the choice of stimulus: with a biphasic pulse, it's possible and sometimes observed to have a bimodal distribution of spike times at high stimulus levels. This corresponds to each phase initiating a spike at a different site on the axon. In our model population, many large-diameter fibers are being driven well over their threshold by the maximum stimulus intensity considered here, so spikes may be elicited by both phases, either centrally or peripheral. Aggregated over the population, this effect can increase the total jitter. We have confirmed that when a monophasic cathodic pulse is presented, jitter in the control population decreases as a function of stimulus intensity (data not shown). In spite of simulated demyelination, the PD model fibers can exhibit two spike initiation sites at high stimulus intensities, as the degraded periphery is still capable of spike initiation and propagation albeit at an augmented threshold, but this occurs much less frequently than in the control population.

Next, we consider a population model in which fibers are removed at random, the RDO model. For a given population size, we selected at random that many of the original 30,000 fibers to include in our analysis of dynamic range, relative spread, latency, and jitter. In order to sample the distribution of possible subpopulations reasonably, we drew 500 randomly selected subpopulations for each population size. The plots in Figure 3.8 represent the average input-output functions, latency and jitter curves for various population sizes. We find that there are no appreciable differences in any of the response measurements on average. That is not to say that every population of 15,000 fibers randomly selected from the original 30,000 will give identical input-output functions or latency curves—indeed, the standard deviation error bars are largest for small population sizes. Rather, it means only that averaged over many trials there is no shift in the quantities measured here. This is the result that should be expected: drawing randomly from a

Gaussian distribution of fiber diameters produces another Gaussian. The statistical distribution of threshold and diameter are unchanged by the random culling of fibers. What is more unexpected is that even when only 25% of the population remains, the input-output curve varies little and error bars are short, suggesting that the majority of fibers can be lost with only minor effects on the population behavior as a whole. The question relevant to psychophysics, then, is only whether there are *enough* fibers left to detect a signal.

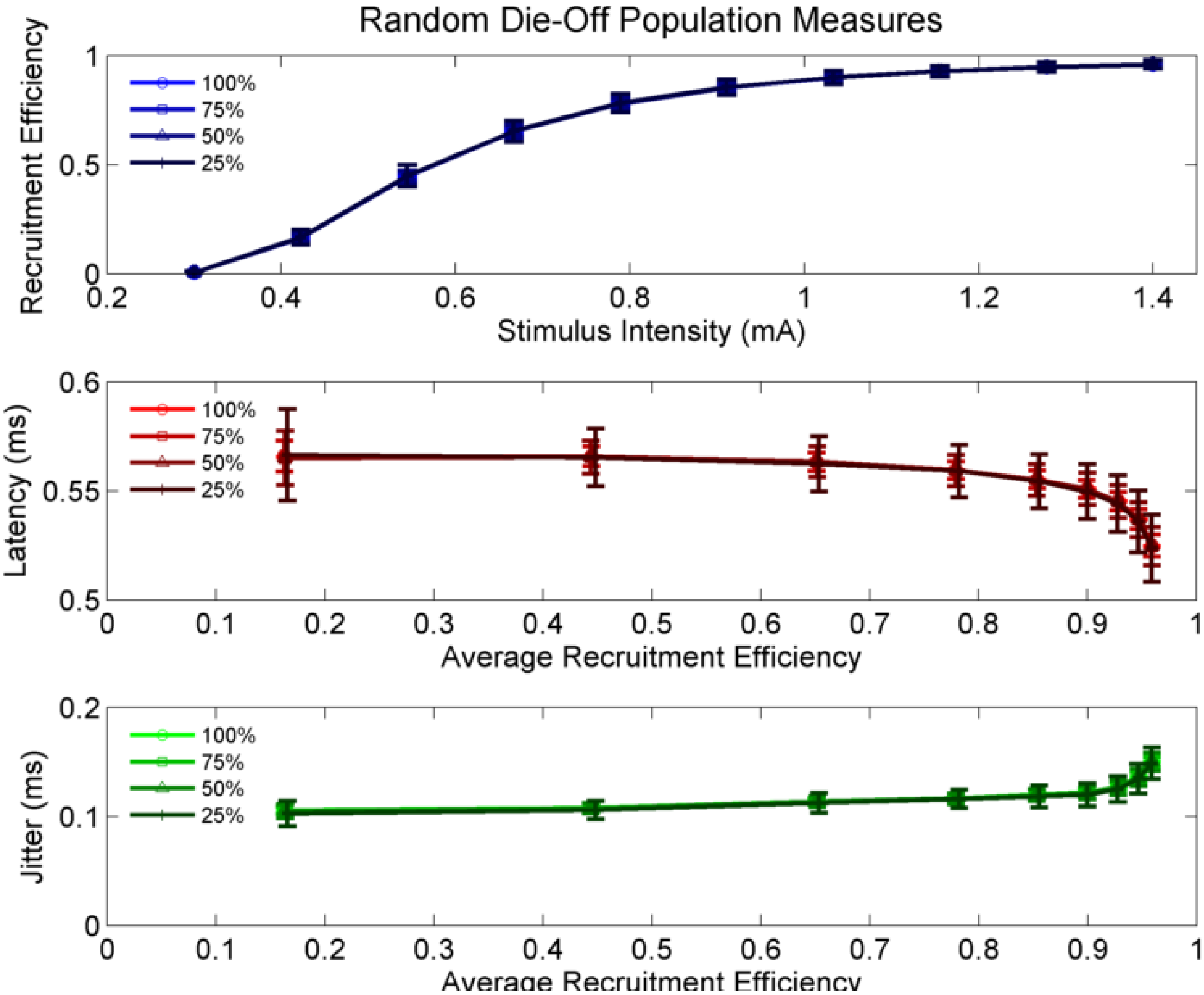

Figure 3.8 Average input-output functions, latency, and jitter curves in randomly selected subpopulations. Curves are indexed by percent of fibers remaining from the original 30,000. Each curve represents the average of 500 randomly drawn populations; error bars mark the standard deviation at each point. Note that the x-axis of the latency and jitter plots is the average recruitment efficiency for the subpopulation.

The final population model of degeneration we consider is constructed by removing fibers in order of their diameter, from smallest to largest (the DDO model). Because there is only one way to remove the top 25% of fibers ordered by size, there is no need to sample multiple subpopulations as in the RDO model. Small-diameter fibers have the highest thresholds for electrical stimuli, and as expected, we observe the most significant effects on jitter and latency at the uppermost end of the dynamic range (Figure 3.9). In the DDO model, smaller population sizes are associated with low jitter. This effect is attributed to the loss of high threshold fibers, who respond more stochastically to a given stimulus level than a low-threshold fiber to that same stimulus. The most striking effect of reducing population size in the DDO model is decreased dynamic range (compare the widths of the input-output curves for the various population sizes) and decreased slope. Slope declines from 0.3933 to 0.2348, then 0.1555 and finally 0.1321 as the percent of remaining fibers drops from 100% to 75%, 50%, and 25% respectively.

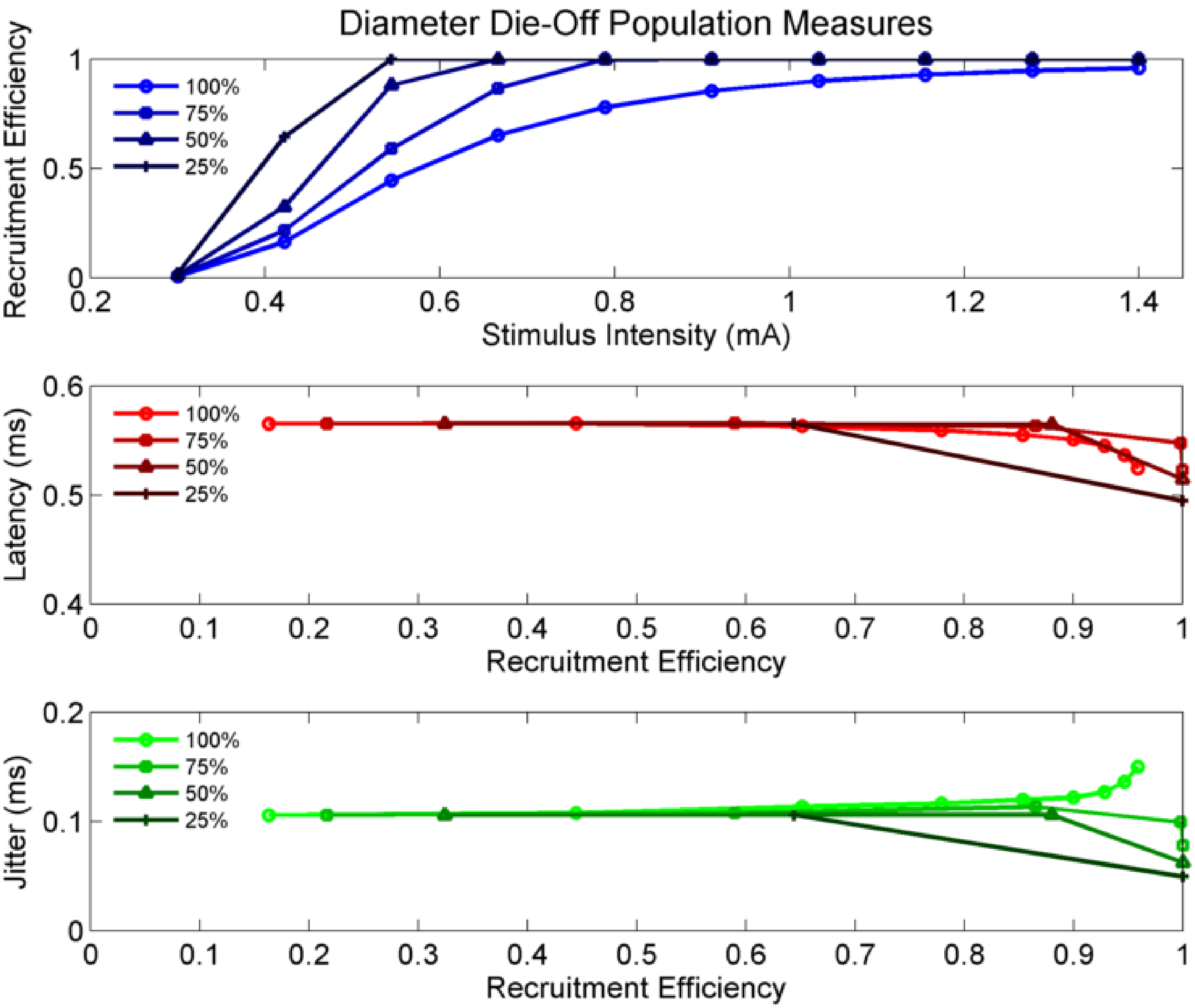

Figure 3.9 Average input-output functions, latency, and jitter curves with fibers removed in order of diameter. Curves are indexed by percent of fibers remaining from the original 30,000.

3.4 DISCUSSION

3.4.1 *Single fiber modeling*

We compared two biophysical ANF models of degeneration, one in which 90% demyelination was simulated along the length of the cable (the TD model) and one in which only a number of peripheral nodes were manipulated (the PD model). After testing the dynamic ranges, latency, and jitter of both models for both AF and CF stimuli, we discovered numerous major differences between the two conditions.

First, spike initiation on the central axon at moderate levels of stimulation is only observed on the PD model. The TD model, like the control, initiates spikes local to the stimulating electrode for the majority of its dynamic range. The reason for this difference pertains to the spatial qualities of anodal and cathodal stimulation: anodal stimulation tends to hyperpolarize locally and depolarize at a distance from the current source, whereas cathodal stimulation depolarizes the axon cable locally and hyperpolarizes some distance away from the current source (for review see [10]). Central excitation in the PD model, usually centered around a site 17 nodes away from the electrode (Figure 3.5 and Figure 3.6), is caused by the anodal phase of the biphasic stimulus. The TD and control models, whose spike initiation histograms are clustered around the electrode site for both AF and CF stimulation, are induced to spike by the cathodal phase of the stimulus. In the PD model, the threshold is increased near the peripheral electrode site due to simulated demyelination, and so it is easier (except at extremely high levels of stimulation) to initiate a spike more centrally, where thresholds match the control. In the TD model, thresholds are uniformly high everywhere along the axon, so it is no easier to induce central spike initiation than in the control model. As such, there is a reversal in the stimulus phase selectivity: the control and TD models have higher thresholds for AF stimuli than CF, but in the PD model exactly the opposite is observed.

A second major difference between the two models is in conduction velocity. Although we do not directly measure the conduction velocities of the TD and PD models here, a metric is implicit in the latency measurement. Because we can confirm through spike initiation histograms that the TD model has the same spike initiation site as the control, and its latency is nearly 1 ms longer than the control for both AF and CF stimulation, we can deduce that the bulk of this difference is in propagation time. This is what we would expect from simulated demyelination along the length of the axon. In the PD model, on the other hand, latency is always shorter than the control (10 μs in CF stimulation and ~50 μs in AF). At the more central site where spikes are initiated in the PD model, the axon is identical to the control condition, and so propagation time is no longer than normal.

In light of these major differences, and also differences in jitter and relative spread, it is obvious that the PD and TD models are not fungible. Electrophysiological studies on chronically deaf ears (induced by a variety of ototoxins) have shown lower latency and jitter, suggesting central spike initiation [68]; only the PD model captures these effects. We conclude that the PD model is a more realistic choice for describing the degeneration of the periphery so ubiquitous in cochlear pathology [68], [89], [91], [152]. There may still be a place for the TD model in the pathology researcher's arsenal—perhaps as a second stage of degeneration, after the peripheral dendrite has disintegrated and the myelin of the central axon begins to unspool. One advantage the TD model may have over the PD model is realistic frequency following—the PD model can entrain to pulse trains up to 1000 Hz, because spikes are initiated in a "healthy" part of the fiber. The TD model, on the other hand, would be expected to have a lower maximal firing rate, which is observed in degenerated fibers.

It must be noted in the interpretation of our results that the morphology of our model is simplified. For example, it features neither a soma nor a peripheral unmyelinated terminal, two structures that act primarily as capacitors [155]. There is also evidence that the soma contributes to jitter [64]. Our model has physiologically appropriate jitter, threshold, latency, chronaxie, and other response measures owing to widespread tuning of its electrical parameters. Thus, morphological changes to the model—such as simulated peripheral demyelination—may not produce identical effects in a more anatomically detailed cable model (such as [76], [86]).

3.4.2 *Population models*

We compared three pathological modifications to a heterogeneous control population of 30,000 simulated ANFs. In the RDO model, we randomly selected subsets of the population to remove. In the DDO model, we removed fibers in order of diameter, from smallest to largest. In the degenerated model, we simulated 30,000 PD model fibers, as developed in the single fiber study. These manipulations are not intended to replicate any one particular pathology in detail, nor would they be expected to occur in isolation (when peripheral degeneration is present, there could also be a loss of fibers). Rather, the aim of the study is to make preliminary predictions about the effects of cochlear changes associated with pathology in a heterogeneous model of the auditory nerve. By differentiating the effects of various types of population-scale damage on the response of the auditory nerve, more optimal, patient-tailored cochlear implant stimulation strategies may be developed.

In the degenerated population model, we observed an elongated dynamic range, nearly 50 μs less latency than the control population across stimulus intensities, and uniformly decreased jitter. Essentially, the behaviors of the single fiber are mirrored when scaled to a population. We might therefore also expect that, in populations where there is significant loss of peripheral dendrites, there will be lower thresholds for anodal than cathodal stimuli. In terms of the neural coding of more complex stimuli, we hypothesize that there may be more challenges preventing abnormal synchrony to the stimulus waveform for a peripherally-degenerated population than a healthy one.

In the RDO model, we observe, on average, strikingly little deviance from the control latency, jitter, and input-output functions. The variance of these quantities is quite low, even when only 25% of the population remains. This result seems to corroborate the apparent lack of evidence for a relationship between total number of surviving spiral ganglion cells and CI performance [156], [157]. It has been suggested by these studies that there is a minimum number of cells that must be present for speech recognition, estimated roughly to be about 5,000—certainly, this agrees with our result that the considered measures were nearly constant down to 7,500 cells. However, such comparisons must be made cautiously, as our model does not account for the spatial distribution of surviving ANFs (which is thought to be predictive of success, especially for focused stimulation strategies [158], [159]). Additionally, the histological studies that have studied the relationship between surviving cell counts and CI performance did not specify the diameter distribution of remaining ANFs; thus it is unclear if the samples were more aligned with the RDO or DDO model. Lastly, it would be capricious to equate neuronal measures of threshold and temporal properties with speech perception—a more temperate comparison might be with the ECAP measures of listeners with known hearing disorders.

In the DDO model, we observe decreases in jitter and latency at the uppermost end of the dynamic range. The most dramatic effect of removing small-diameter fibers is the truncation of the dynamic range from above (the input-output function saturates at a lower stimulus intensity). Although we considered up to 75% loss of fibers by diameter, pathologies that preferentially affect smaller fibers may not be so devastating in terms of total cell death. Smaller fiber diameters are typically found in low- and medium- spontaneous rate fibers [146], which constitute less than 40% of the auditory nerve population [91], [146], [160]. Thus pathologies like noise-induced excitotoxicity, which specifically target low- and medium spontaneous rate (and hence smaller) fibers [89], [91], might be best modeled with 0-40% loss in the DDO model. Unfortunately, our preliminary measures do not address many of the consequences thought to result from the loss of this particular subpopulation: low- and medium- spontaneous rate fibers project to different parts of the cochlear nucleus [161], [162], which will doubtlessly impact higher auditory processing. We would also expect there to be a distortion of the neural code for an amplitude-modulated sound (especially if the modulation depth is high), owing to a dearth of high-threshold fibers; a quantification of the information lost in the coding of a time-varying stimulus presented to the DDO model may be a future direction for research.

3.4.3 *Conclusions*

In this preliminary study of the effects of various simulated pathologies in a biophysical model of the auditory nerve, we consider two single fiber models of degeneration and three population-scale models. We find that:

1. A single fiber model where demyelination is simulated along the length of the axon will not predict more central spike initiation or reduced latency, two characteristics of peripheral nerve degeneration.
2. A single fiber model where demyelination is simulated in a peripheral segment may have lower thresholds for anodal than cathodal stimuli, if the stimulating electrode is over the "demyelinated" region.
3. A population of fibers where demyelination is simulated peripherally exhibits a larger dynamic range, lower latency, and lower jitter than a control population.

4. When fibers are randomly removed from a control population of 30,000 heterogeneous, simulated fibers, the input-output function, latency, and jitter of the surviving cells varies little. This holds for at least up to 75% cell death.
5. When the smallest, high-threshold fibers are removed from a normal population preferentially, dynamic range is truncated. The most dramatic effects of removing these fibers may not be revealed by the metrics imposed in the present study.

BIBLIOGRAPHY

[1] G. O'Brien and J. T. Rubinstein, "The development of biophysical models of the auditory nerve: single node and cable models," *Netw. Comput. Neural Syst.*

[2] J. T. Rubinstein, "How cochlear implants encode speech.," *Curr. Opin. Otolaryngol. Head Neck Surg.*, vol. 12, pp. 444–448, 2004.

[3] B. C. J. Moore, "Coding of sounds in the auditory system and its relevance to signal processing and coding in cochlear implants.," *Otol. Neurotol.*, vol. 24, no. 2, pp. 243–54, Mar. 2003.

[4] J. J. Briaire and J. H. Frijns, "Unraveling the electrically evoked compound action potential.," *Hear. Res.*, vol. 205, no. 1–2, pp. 143–56, Jul. 2005.

[5] R. V Shannon, "Temporal modulation transfer functions in patients with cochlear implants.," *J. Acoust. Soc. Am.*, vol. 91, no. 4 Pt 1, pp. 2156–64, Apr. 1992.

[6] J. J. Galvin and Q. J. Fu, "Influence of stimulation rate and loudness growth on modulation detection and intensity discrimination in cochlear implant users.," *Hear. Res.*, vol. 250, no. 1–2, pp. 46–54, Apr. 2009.

[7] D. R. McNeal, "Analysis of a Model for Excitation of Myelinated Nerve," *IEEE Trans. Biomed. Eng.*, vol. BME-23, no. 4, pp. 329–337, Jul. 1976.

[8] A. Hodgkin and A. Huxley, "A quantitative description of membrane current and its application to conduction and excitation in nerve," *J. Physiol.*, vol. 117, no. 4, pp. 500–544, 1952.

[9] J. Rinzel, "Electrical excitability of cells, theory, and experiment: Review of the foundation and an update.," *Bull. Math. Biol.*, vol. 52, no. 1, pp. 5–23, 1990.

[10] F. Rattay, "The basic mechanism for the electrical stimulation of the nervous system," *Neuroscience*, vol. 89, no. 2, pp. 335–346, Mar. 1999.

[11] H. Mino, J. T. Rubinstein, C. A. Miller, and P. J. Abbas, "Effects of electrode-to-fiber distance on temporal neural response with electrical stimulation.," *IEEE Trans. Biomed. Eng.*, vol. 51, no. 1, pp. 13–20, Jan. 2004.

[12] R. P. Morse and E. F. Evans, "Additive noise can enhance temporal coding in a computational model of analogue cochlear implant stimulation," *Hear. Res.*, vol. 133, no. 1–2, pp. 107–119, Jul. 1999.

[13] A. J. Matsuoka, J. T. Rubinstein, P. J. Abbas, and C. A. Miller, "The effects of interpulse interval on stochastic properties of electrical stimulation: models and measurements.," *IEEE Trans. Biomed. Eng.*, vol. 48, no. 4, pp. 416–24, Apr. 2001.

[14] L. A. Cartee, "Evaluation of a model of the cochlear neural membrane. II: Comparison of model and physiological measures of membrane properties measured in response to intrameatal electrical stimulation," *Hear. Res.*, vol. 146, no. 1–2, pp. 153–166, Aug. 2000.

[15] J. J. Briaire and J. H. Frijns, "The consequences of neural degeneration regarding optimal cochlear implant position in scala tympani: a model approach.," *Hear. Res.*, vol. 214, no. 1–2, pp. 17–27, Apr. 2006.

[16] N. S. Imennov and J. T. Rubinstein, "Stochastic population model for electrical stimulation of the auditory nerve," *IEEE Trans Biomed Eng*, vol. 56, no. 10, pp. 2493–2501, 2009.

[17] C. A. Miller, J. Woo, P. J. Abbas, N. Hu, and B. K. Robinson, "Neural masking by sub-threshold electric stimuli: animal and computer model results.," *J. Assoc. Res. Otolaryngol.*, vol. 12, no. 2, pp. 219–32, Apr. 2011.

[18] M. H. Negm and I. C. Bruce, “The Effects of HCN and KLT Ion Channels on Adaptation and Refractoriness in a Stochastic Auditory Nerve Model,” vol. 61, no. 11, pp. 2749–2759, 2014.

[19] J. E. Smit, T. Hanekom, A. van Wieringen, J. Wouters, and J. J. Hanekom, “Threshold predictions of different pulse shapes using a human auditory nerve fibre model containing persistent sodium and slow potassium currents,” *Hear. Res.*, vol. 269, no. 1–2, pp. 12–22, Oct. 2010.

[20] J. P. Reilly, V. T. Freeman, and W. D. Larkin, “Sensory Effects of Transient Electrical Stimulation - Evaluation with a Neuroelectric Model,” *IEEE Trans. Biomed. Eng.*, vol. BME-32, no. 12, pp. 1001–1011, Dec. 1985.

[21] J. Colombo and C. W. Parkins, “A model of electrical excitation of the mammalian auditory-nerve neuron.,” *Hear. Res.*, vol. 31, no. 3, pp. 287–311, Dec. 1987.

[22] B. Frankenhaeuser and a F. Huxley, “The action potential in the myelinated nerve fibre of Xenopus laevis as computed on the basis of voltage clamp data,” *J. Physiol.*, vol. 171, pp. 302–315, 1964.

[23] F. Rattay and M. Aberham, “Modeling axon membranes for functional electrical stimulation.,” *IEEE Trans. Biomed. Eng.*, vol. 40, no. 12, pp. 1201–9, Dec. 1993.

[24] S. Y. Chiu, J. M. Ritchie, R. B. Rogart, and D. Stagg, “A quantitative description of membrane currents in rabbit myelinated nerve.,” *J. Physiol.*, vol. 292, pp. 149–166, 1979.

[25] J. Sweeney, J. Mortimer, and D. Durand, “Modeling of mammalian myelinated nerve for functional neuromuscular stimulation,” in *IEEE 9th Annual Conference of the Engineering in Medicine and Biology Society*, 1987.

[26] J. R. Schwarz and G. Eikhof, “Na currents and action potentials in rat myelinated nerve fibres at 20 and 37 degrees C.,” *Pflugers Arch.*, vol. 409, pp. 569–577, 1987.

[27] H. Motz and F. Rattay, “A study of the application of the Hodgkin-Huxley and the Frankenhaeuser-Huxley model for electrostimulation of the acoustic nerve,” *Neuroscience*, vol. 18, no. 3, pp. 699–712, Jul. 1986.

[28] L. A. Cartee, “Spiral ganglion cell site of excitation II: numerical model analysis.,” *Hear. Res.*, vol. 215, pp. 22–30, 2006.

[29] J. H. Frijns, J. Mooij, and J. H. ten Kate, “A quantitative approach to modeling mammalian myelinated nerve fibers for electrical prosthesis design.,” *IEEE Trans. Biomed. Eng.*, vol. 41, no. 6, pp. 556–66, Jun. 1994.

[30] M. H. Negm and I. C. Bruce, “Effects of I h and I KLT on the Response of the Auditory Nerve to Electrical Stimulation in a Stochastic Hodgkin – Huxley Model,” pp. 5539–5542, 2008.

[31] J. Röper and J. R. Schwarz, “Heterogeneous distribution of fast and slow potassium channels in myelinated rat nerve fibres.,” *J. Physiol.*, vol. 416, pp. 93–110, 1989.

[32] G. Reid, a Scholz, H. Bostock, and W. Vogel, “Human axons contain at least five types of voltage-dependent potassium channel.,” *J. Physiol.*, vol. 518 (Pt 3, pp. 681–96, 1999.

[33] C. L. Adamson, M. a. Reid, Z. L. Mo, J. Bowne-English, and R. L. Davis, “Firing features and potassium channel content of murine spiral ganglion neurons vary with cochlear location,” *J. Comp. Neurol.*, vol. 447, pp. 331–350, 2002.

[34] Z.-L. Mo, C. L. Adamson, and R. L. Davis, “Dendrotoxin-sensitive K(+) currents contribute to accommodation in murine spiral ganglion neurons.,” *J. Physiol.*, vol. 542, pp. 763–778, 2002.

[35] J. Woo, C. A. Miller, and P. J. Abbas, “Biophysical Model of an Auditory Nerve Fiber

With a Novel Adaptation Component," *IEEE Trans. Biomed. Eng.*, vol. 56, no. 9, pp. 2177–2180, Sep. 2009.

[36] J. Woo, C. A. Miller, and P. J. Abbas, "Simulation of the electrically stimulated cochlear neuron: modeling adaptation to trains of electric pulses.," *IEEE Trans. Biomed. Eng.*, vol. 56, no. 5, pp. 1348–59, May 2009.

[37] J. E. Smit, T. Hanekom, and J. J. Hanekom, "Predicting action potential characteristics of human auditory nerve fibres through modification of the Hodgkin – Huxley equations," *S. Afr. J. Sci.*, vol. 104, no. 7–8, pp. 284–292, 2008.

[38] a Scholz, G. Reid, W. Vogel, and H. Bostock, "Ion channels in human axons.," *J. Neurophysiol.*, vol. 70, pp. 1274–9, 1993.

[39] J. R. Schwarz, G. Reid, and H. Bostock, "Action potentials and membrane currents in the human node of Ranvier," *Pflugers Arch. Eur. J. Physiol.*, vol. 430, pp. 283–292, 1995.

[40] W. Wesselink, J. Holsheimer, and H. Boom, "A model of the electrical behaviour of myelinated sensory nerve fibres based on human data," *Med. Biol. Eng. Comput.*, vol. 37, no. 2, pp. 228–235, 1997.

[41] E. C. Moxon, "Neural and mechanical responses to electrical stimulation of the cat's inner ear," MIT, Cambridge, Mass, 1971.

[42] N. Kiang and E. Moxon, "Physiological considerations in artificial stimulation of the inner ear," *Ann. Otol. Rhinol. Laryngol.*, vol. 81, no. 5, pp. 714–30, 1972.

[43] L. Litvak, B. Delgutte, and D. Eddington, "Auditory nerve fiber responses to electric stimulation: modulated and unmodulated pulse trains.," *J. Acoust. Soc. Am.*, vol. 110, pp. 368–379, 2001.

[44] L. Litvak, B. Delgutte, and D. Eddington, "Improved temporal coding of sinusoids in electric stimulation of the auditory nerve using desynchronizing pulse trains.," *J. Acoust. Soc. Am.*, vol. 114, pp. 2079–2098, 2003.

[45] E. Javel and G. Clark, "Responses of cat auditory nerve fibers to biphasic electrical current pulses," *Ann. Otol. Rhinol. Laryngol.*, vol. 96, pp. 26–30, 1987.

[46] N. Kiang, T. Watanabe, E. Thomas, and L. Clark, "Discharge Patterns of Single Fibers in the Cat's Auditory Nerve," *M.I.T. Res. Monogr. no. 35*, 1965.

[47] J. T. Rubinstein, B. S. Wilson, C. C. Finley, and P. J. Abbas, "Pseudospontaneous activity : stochastic independence of auditory nerve fibers with electrical stimulation," vol. 127, pp. 108–118, 1999.

[48] A. Verveen and H. Derksen, "Fluctuations in membrane potential of axons and the problem of coding," *Kybernetic*, vol. 2, no. 4, pp. 152–160, 1965.

[49] J. T. Rubinstein, "Threshold Fluctuations in Node of Ranvier In an N Sodium Channel Model of the Node of Ranvier," vol. 68, no. March, pp. 779–785, 1995.

[50] B. Sakmann, E. Neher, and M. B. Jackson, *Single-Channel Recording*, vol. Chapter 6. 1995.

[51] J. A. White, J. T. Rubinstein, and A. R. Kay, "Channel noise in neurons.," *Trends Neurosci.*, vol. 23, pp. 131–7, 2000.

[52] J. R. Groff, H. DeRemigio, and G. D. Smith, "Markov chain models of ion channels and calcium release sites," in *Stochastic Methods in Neuroscience*, 2009, pp. 29–64.

[53] R. F. Fox and Y. N. Lu, "Emergent collective behavior in large numbers of globally coupled independently stochastic ion channels," *Phys. Rev. E*, vol. 49, pp. 3421–3431, 1994.

[54] D. T. Gillespie, "Exact Stochastic Simulation of couple chemical reactions," *J. Phys.*

Chem., vol. 81, pp. 2340–2361, 1977.

[55] H. Mino, J. T. Rubinstein, and J. A. White, “Comparison of Algorithms for the Simulation of Action Potentials with Stochastic Sodium Channels,” *Ann. Biomed. Eng.*, vol. 30, no. 4, pp. 578–587, Apr. 2002.

[56] N. S. Imennov, J. H. Won, W. R. Drennan, E. Jameyson, and J. T. Rubinstein, “Detection of acoustic temporal fine structure by cochlear implant listeners: Behavioral results and computational modeling,” *Hear. Res.*, vol. 298, pp. 60–72, Apr. 2013.

[57] J. Goldwyn, N. Imennov, M. Famulare, and E. Shea-Brown, “Stochastic differential equation models for ion channel noise in Hodgkin-Huxley neurons,” *Phys. Rev. E - Stat. Nonlinear, Soft Matter Phys.*, vol. 83, pp. 1–16, 2011.

[58] J. Woo, C. A. Miller, and P. J. Abbas, “The dependence of auditory nerve rate adaptation on electric stimulus parameters, electrode position, and fiber diameter: A computer model study,” *J. Assoc. Res. Otolaryngol.*, vol. 11, pp. 283–296, 2010.

[59] C. A. Miller, N. Hu, F. Zhang, B. K. Robinson, and P. J. Abbas, “Changes across time in the temporal responses of auditory nerve fibers stimulated by electric pulse trains.,” *J. Assoc. Res. Otolaryngol.*, vol. 9, no. 1, pp. 122–37, Mar. 2008.

[60] F. Zhang, C. A. Miller, B. K. Robinson, P. J. Abbas, and N. Hu, “Changes across time in spike rate and spike amplitude of auditory nerve fibers stimulated by electric pulse trains.,” *J. Assoc. Res. Otolaryngol.*, vol. 8, no. 3, pp. 356–72, Sep. 2007.

[61] L. A. Cartee, C. van den Honert, C. C. Finley, and R. L. Miller, “Evaluation of a model of the cochlear neural membrane. I. Physiological measurement of membrane characteristics in response to intrameatal electrical stimulation,” *Hear. Res.*, vol. 146, no. 1–2, pp. 143–152, Aug. 2000.

[62] L. T. Cohen, “Practical model description of peripheral neural excitation in cochlear implant recipients: 5. Refractory recovery and facilitation,” *Hear. Res.*, vol. 248, no. 1–2, pp. 1–14, 2009.

[63] F. Rattay, “Analysis of models for extracellular fiber stimulation.,” *IEEE Trans. Biomed. Eng.*, vol. 36, no. 7, pp. 676–82, Jul. 1989.

[64] C. Van den Honert and P. H. Stypulkowski, “Physiological properties of the electrically stimulated auditory nerve. II. Single fiber recordings,” *Hear. Res.*, vol. 14, pp. 225–243, 1984.

[65] C. van den Honert and P. H. Stypulkowski, “Single fiber mapping of spatial excitation patterns in the electrically stimulated auditory nerve.,” *Hear. Res.*, vol. 29, pp. 195–206, 1987.

[66] C. van den Honert and P. H. Stypulkowski, “Temporal response patterns of single auditory nerve fibers elicited by periodic electrical stimuli.,” *Hear. Res.*, vol. 29, pp. 207–222, 1987.

[67] C. A. Miller, P. J. Abbas, K. V Nourski, N. Hu, and B. K. Robinson, “Electrode configuration influences action potential initiation site and ensemble stochastic response properties,” *Hear. Res.*, vol. 175, pp. 200–214, 2003.

[68] R. K. Shepherd and E. Javel, “Electrical stimulation of the auditory nerve. I. Correlation of physiological responses with cochlear status,” *Hear. Res.*, vol. 108, pp. 112–144, 1997.

[69] J. H. Frijns and J. H. ten Kate, “A model of myelinated nerve fibres for electrical prosthesis design.,” *Med. Biol. Eng. Comput.*, vol. 32, pp. 391–8, 1994.

[70] J. Crank and P. Nicolson, “A practical method for numerical evaluation of solutions of partial differential equations of the heat-conduction type,” *Adv. Comput. Math.*, vol. 6, no.

1, pp. 207–226, 1996.

[71] J. T. Rubinstein, “Analytical theory for extracellular electrical stimulation of nerve with focal electrodes,” vol. 60, no. September, 1991.

[72] W. A. H. Rushton, “A theory of the effects of fibre size in medullated nerve,” *J. Physiol.*, vol. 115, pp. 101–122, 1951.

[73] C. Koch, *Biophysics of Computation: Information Processing in Single Neurons*. New York: Oxford University Press, 1999.

[74] R. FitzHugh, “Computation of impulse initiation and saltatory conduction in a myelinated nerve fiber,” *Biophys. J.*, vol. 2, pp. 11–21, 1962.

[75] L. Goldman and J. S. Albus, “Computation of impulse conduction in myelinated fibers; theoretical basis of the velocity-diameter relation,” *Biophys. J.*, vol. 8, pp. 596–607, 1968.

[76] C. W. Parkins and J. Colombo, “Auditory-nerve single-neuron thresholds to electrical stimulation from scala tympani electrodes.,” *Hear. Res.*, vol. 31, pp. 267–85, 1987.

[77] M. C. Liberman and M. E. Oliver, “Morphometry of intracellularly labeled neurons of the auditory nerve: correlations with functional properties.,” *J. Comp. Neurol.*, vol. 223, pp. 163–176, 1984.

[78] M. C. Brown, “Morphology of labeled efferent fibers in the guinea pig cochlea.,” *J. Comp. Neurol.*, vol. 260, pp. 605–18, 1987.

[79] O. Gleich and S. Wilson, “The diameters of guinea pig auditory nerve fibres: distribution and correlation with spontaneous rate.,” *Hear. Res.*, vol. 71, pp. 69–79, 1993.

[80] J. H. Frijns, S. L. de Snoo, and R. Schoonhoven, “Potential distributions and neural excitation patterns in a rotationally symmetric model of the electrically stimulated cochlea,” *Hear. Res.*, vol. 87, no. 1–2, pp. 170–186, Jul. 1995.

[81] J. H. Frijns, S. L. de Snoo, and J. H. ten Kate, “Spatial selectivity in a rotationally symmetric model of the electrically stimulated cochlea,” *Hear. Res.*, vol. 95, no. 1–2, pp. 33–48, May 1996.

[82] F. Rattay, P. Lutter, and H. Felix, “A model of the electrically excited human cochlear neuron I . Contribution of neural substructures to the generation and propagation of spikes,” vol. 153, pp. 43–63, 2001.

[83] C. Finley, B. Wilson, and M. White, “Models of neural responsiveness to electrical stimulation,” in *Cochlear Implants: Models of the Electrically Stimulated Ear*, J. Miller and F. Spelmen, Eds. New York: Springer, 1990, pp. 55–93.

[84] a G. Richardson, C. C. McIntyre, and W. M. Grill, “Modelling the effects of electric fields on nerve fibres: influence of the myelin sheath.,” *Med. Biol. Eng. Comput.*, vol. 38, no. 4, pp. 438–446, 2000.

[85] C. C. McIntyre, A. G. Richardson, and W. M. Grill, “Modeling the excitability of mammalian nerve fibers: influence of afterpotentials on the recovery cycle.,” *J. Neurophysiol.*, vol. 87, no. 2, pp. 995–1006, 2002.

[86] D. M. T. Dekker, J. J. Briaire, and J. H. M. Frijns, “The impact of internodal segmentation in biophysical nerve fiber models.,” *J. Comput. Neurosci.*, vol. 37, no. 2, pp. 307–15, 2014.

[87] P. a Leake and G. T. Hradek, “Cochlear pathology of long term neomycin induced deafness in cats.,” *Hear. Res.*, vol. 33, pp. 11–33, 1988.

[88] S. G. Kujawa and M. C. Liberman, “Adding insult to injury: cochlear nerve degeneration after ‘temporary’ noise-induced hearing loss.,” *J. Neurosci.*, vol. 29, no. 45, pp. 14077–14085, 2009.

[89] H. W. Lin, A. C. Furman, S. G. Kujawa, and M. C. Liberman, “Primary neural degeneration in the guinea pig cochlea after reversible noise-induced threshold shift,” *J. Assoc. Res. Otolaryngol.*, vol. 12, no. 5, pp. 605–616, 2011.

[90] J. Snel-Bongers, J. J. Briaire, E. H. Van Der Veen, R. K. Kalkman, and J. H. M. Frijns, “Threshold levels of dual electrode stimulation in cochlear implants,” *J. Assoc. Res. Otolaryngol.*, vol. 14, pp. 781–790, 2013.

[91] A. C. Furman, S. G. Kujawa, and M. C. Liberman, “Noise-induced cochlear neuropathy is selective for fibers with low spontaneous rates.,” *J. Neurophysiol.*, vol. 110, pp. 577–86, 2013.

[92] C. A. Miller, P. J. Abbas, B. K. Robinson, J. T. Rubinstein, and A. J. Matsuoka, “Electrically evoked single-fiber action potentials from cat: Responses to monopolar, monophasic stimulation,” *Hear. Res.*, vol. 130, pp. 197–218, 1999.

[93] H. Spoendlin and A. Schrott, “Analysis of the human auditory nerve,” *Hear. Res.*, vol. 43, no. 1, pp. 25–38, Dec. 1989.

[94] J. H. Goldwyn, E. Shea-Brown, and J. T. Rubinstein, “Encoding and decoding amplitude-modulated cochlear implant stimuli-- a point process analysis,” *J. Comput. Neurosci.*, vol. 28, no. 3, pp. 405–424, 2011.

[95] I. C. Bruce, L. S. Irlicht, M. W. White, S. J. O’Leary, S. Dynes, E. Javel, and G. M. Clark, “A stochastic model of the electrically stimulated auditory nerve: pulse-train response.,” *IEEE Trans. Biomed. Eng.*, vol. 46, pp. 630–637, 1999.

[96] J. H. Goldwyn, J. T. Rubinstein, and E. Shea-Brown, “A point process framework for modeling electrical stimulation of the auditory nerve,” *J Neurophysiol*, vol. 108, no. 5, pp. 1430–1452, Jan. 2012.

[97] M. C. van Rossum, “A novel spike distance.,” *Neural Comput.*, vol. 13, no. 4, pp. 751–763, 2001.

[98] J. D. Victor and K. P. Purpura, “Nature and precision of temporal coding in visual cortex: a metric-space analysis.,” *J. Neurophysiol.*, vol. 76, no. 2, pp. 1310–1326, 1996.

[99] W. Bialek, F. Rieke, R. R. de Ruyter van Steveninck, and D. Warland, “Reading a neural code.,” *Science*, vol. 252, pp. 1854–1857, 1991.

[100] G. O’Brien, N. S. Imennov, and J. T. Rubinstein, “Simulating electrical modulation detection thresholds using a biophysical model of the auditory nerve.,” *J. Acoust. Soc. Am.*

[101] E. D. Young, “Neural representation of spectral and temporal information in speech.,” *Philos. Trans. R. Soc. Lond. B. Biol. Sci.*, vol. 363, no. 1493, pp. 923–45, Mar. 2008.

[102] K. Hopkins and B. C. J. Moore, “The contribution of temporal fine structure to the intelligibility of speech in steady and modulated noise.,” *J. Acoust. Soc. Am.*, vol. 125, no. 1, pp. 442–6, Jan. 2009.

[103] Y. Cazals, M. Pelizzone, O. Saudan, and C. Boex, “Low-pass filtering in amplitude modulation detection associated with vowel and consonant identification in subjects with cochlear implants.,” *J. Acoust. Soc. Am.*, vol. 96, no. 4, pp. 2048–54, Oct. 1994.

[104] Q. J. Fu, “Temporal processing and speech recognition in cochlear implant users.,” *Neuroreport*, vol. 13, no. 13, pp. 1635–9, Sep. 2002.

[105] J. H. Won, W. R. Drennan, K. Nie, E. M. Jameyson, and J. T. Rubinstein, “Acoustic temporal modulation detection and speech perception in cochlear implant listeners.,” *J. Acoust. Soc. Am.*, vol. 130, no. 1, pp. 376–388, Jul. 2011.

[106] X. Luo, J. J. Galvin, and Q.-J. Fu, “Effects of stimulus duration on amplitude modulation processing with cochlear implants.,” *J. Acoust. Soc. Am.*, vol. 127, pp. EL23–L29, 2010.

[107] M. Chatterjee and S. C. Peng, “Processing F0 with cochlear implants: Modulation frequency discrimination and speech intonation recognition,” *Hear. Res.*, vol. 235, pp. 143–156, 2008.

[108] B. E. Pfingst, L. Xu, and C. S. Thompson, “Effects of carrier pulse rate and stimulation site on modulation detection by subjects with cochlear implants,” *J. Acoust. Soc. Am.*, vol. 121, no. 4, p. 2236, 2007.

[109] J. J. Galvin and Q. J. Fu, “Effects of stimulation rate, mode and level on modulation detection by cochlear implant users.,” *J. Assoc. Res. Otolaryngol.*, vol. 6, no. 3, pp. 269–79, Sep. 2005.

[110] P. Busby, Y. Tong, and G. Clark, “The perception of temporal modulations by cochlear implant patients.,” *J. Acoust. Soc. Am.*, vol. 94, no. 1, pp. 124–31, Jul. 1993.

[111] W. S. Geisler, D. G. Albrecht, R. J. Salvi, and S. Saunders, “Discrimination Performance of Single Neurons : Discrimination Performance Information Rate and Temporal-Pattern,” 1991.

[112] P. X. Joris and T. C. Yin, “Responses to amplitude-modulated tones in the auditory nerve of the cat.,” *J. Acoust. Soc. Am.*, vol. 91, pp. 215–232, 1992.

[113] B. S. Krishna and M. N. Semple, “Auditory temporal processing: responses to sinusoidally amplitude-modulated tones in the inferior colliculus.,” *J. Neurophysiol.*, vol. 84, pp. 255–273, 2000.

[114] P. X. Joris, C. E. Schreiner, and a Rees, “Neural processing of amplitude-modulated sounds.,” *Physiol. Rev.*, vol. 84, no. 2, pp. 541–77, Apr. 2004.

[115] P. C. Nelson and L. H. Carney, “Neural rate and timing cues for detection and discrimination of amplitude-modulated tones in the awake rabbit inferior colliculus.,” *J. Neurophysiol.*, vol. 97, no. 1, pp. 522–39, Jan. 2007.

[116] T. Dau, B. Kollmeier, and A. Kohlrausch, “Modeling auditory processing of amplitude modulation. I. Detection and masking with narrow-band carriers.,” *J. Acoust. Soc. Am.*, vol. 102, pp. 2892–2905, 1997.

[117] M. J. Hewitt and R. Meddis, “A computer model of amplitude-modulation sensitivity of single units in the inferior colliculus,” vol. 95, no. 4, pp. 2145–2159, 1994.

[118] Y. Xu and L. M. Collins, “Predictions of psychophysical measurements for sinusoidal amplitude modulated (SAM) pulse-train stimuli from a stochastic model.,” *IEEE Trans. Biomed. Eng.*, vol. 54, no. 8, pp. 1389–98, Aug. 2007.

[119] M. G. Heinz, X. Zhang, I. C. Bruce, and L. H. Carney, “Auditory nerve model for predicting performance limits of normal and impaired listeners,” *Acoust. Res. Lett. Online*, vol. 2, no. 3, p. 91, 2001.

[120] M. G. Heinz, H. S. Colburn, and L. H. Carney, “Evaluating auditory performance limits: i. one-parameter discrimination using a computational model for the auditory nerve.,” *Neural Comput.*, vol. 13, no. 10, pp. 2273–2316, 2001.

[121] M. G. Heinz, H. S. Colburn, and L. H. Carney, “Evaluating auditory performance limits: II. One-parameter discrimination with random-level variation.,” *Neural Comput.*, vol. 13, no. 10, pp. 2317–38, Oct. 2001.

[122] R. Hartmann, G. Topp, and R. Klinke, “Discharge patterns of cat primary auditory fibers with electrical stimulation of the cochlea,” *Hear. Res.*, vol. 13, pp. 47–62, 1984.

[123] C. A. Miller, P. J. Abbas, B. K. Robinson, J. T. Rubinstein, and A. J. Matsuoka, “Electrically evoked single-fiber action potentials from cat: responses to monopolar, monophasic stimulation.,” *Hear. Res.*, vol. 130, pp. 197–218, 1999.

[124] J. T. Rubinstein, M. Soma, and F. A. Spelman, “Mixed boundary value problems in the implanted cochlea: An analytical model of a cylindrical banded electrode array.,” in *IEEE Seventh Annual Conference of the Engineering in Medicine and Biology Society*, 1985, vol. 11, pp. 1120–1123.

[125] H. Fletcher and W. A. Munson, “Loudness, its Definition, Measurement and Calculation,” *J. Acoust. Soc. Am.*, vol. 5, pp. 82–108, 1933.

[126] L. H. Carney, “Spatiotemporal encoding of sound level: Models for normal encoding and recruitment of loudness,” *Hear. Res.*, vol. 76, pp. 31–44, 1994.

[127] E. M. Relkin and J. R. Doucet, “Is loudness simply proportional to the auditory nerve spike count?,” *J. Acoust. Soc. Am.*, vol. 101, pp. 2735–2740, 1997.

[128] J. J. Eggermont, “Between sound and perception: Reviewing the search for a neural code,” *Hearing Research*, vol. 157. pp. 1–42, 2001.

[129] M. G. Heinz, J. B. Issa, and E. D. Young, “Auditory-nerve rate responses are inconsistent with common hypotheses for the neural correlates of loudness recruitment,” *J. Assoc. Res. Otolaryngol.*, vol. 6, pp. 91–105, 2005.

[130] R. V. Shannon, “Threshold and loudness functions for pulsatile stimulation of cochlear implants,” *Hear. Res.*, vol. 18, pp. 135–143, 1985.

[131] R. V Shannon, “A model of threshold for pulsatile electrical stimulation of cochlear implants.,” *Hear. Res.*, vol. 40, pp. 197–204, 1989.

[132] T. G. Forrest and D. M. Green, “Detection of partially filled gaps in noise and the temporal modulation transfer function.,” *J. Acoust. Soc. Am.*, vol. 82, pp. 1933–1943, 1987.

[133] J. C. Middlebrooks, “Auditory cortex phase locking to amplitude-modulated cochlear implant pulse trains.,” *J. Neurophysiol.*, vol. 100, pp. 76–91, 2008.

[134] J. M. Goldberg and P. B. Brown, “Response of binaural neurons of dog superior olivary complex to dichotic tonal stimuli: some physiological mechanisms of sound localization.,” *J. Neurophysiol.*, vol. 32, pp. 613–636, 1969.

[135] Y. Cazals, “Low-pass filtering in amplitude modulation detection associated with vowel and consonant identification in subjects with cochlear implants,” *J. Acoust. Soc. Am.*, vol. 96, no. 4, p. 2048, Oct. 1994.

[136] S. P. Bacon and N. F. Viemeister, “Temporal modulation transfer functions in normal-hearing and hearing-impaired listeners.,” *Audiology*, vol. 24, pp. 117–134, 1985.

[137] S. P. Bacon and R. M. Gleitman, “Modulation detection in subjects with relatively flat hearing losses.,” *J. Speech Hear. Res.*, vol. 35, pp. 642–653, 1992.

[138] S. B. C. Dynes and B. Delgutte, “Phase-locking of auditory-nerve discharges to sinusoidal electric stimulation of the cochlea,” *Hear. Res.*, vol. 58, pp. 79–90, 1992.

[139] C. K. Machens, M. B. Stemmler, P. Prinz, R. Krahe, B. Ronacher, and A. V Herz, “Representation of acoustic communication signals by insect auditory receptor neurons.,” *J. Neurosci.*, vol. 21, pp. 3215–3227, 2001.

[140] C. M. McKay and K. R. Henshall, “Amplitude modulation and loudness in cochlear implantees,” *J. Assoc. Res. Otolaryngol.*, vol. 11, pp. 101–111, 2010.

[141] C. M. McKay and H. J. McDermott, “Loudness perception with pulsatile electrical stimulation: the effect of interpulse intervals.,” *J. Acoust. Soc. Am.*, vol. 104, no. 2 Pt 1, pp. 1061–1074, 1998.

[142] A. J. Oxenham and B. C. J. Moore, “Modeling the additivity of nonsimultaneous masking,” *Hear. Res.*, vol. 80, no. 1, pp. 105–118, 1994.

[143] C. Lorenzi, C. Micheyl, and F. Berthommier, “Neuronal correlates of perceptual amplitude-modulation detection,” *Hear. Res.*, vol. 90, no. 1–2, pp. 219–227, 1995.

[144] S. H. Nirenberg and J. D. Victor, “Analyzing the activity of large populations of neurons: how tractable is the problem?,” *Current Opinion in Neurobiology*, vol. 17. pp. 397–400, 2007.

[145] J. H. Macke, P. Berens, A. S. Ecker, A. S. Tolias, and M. Bethge, “Generating spike trains with specified correlation coefficients.,” *Neural Comput.*, vol. 21, pp. 397–423, 2009.

[146] M. C. Liberman and M. E. Oliver, “Morphometry of intracellularly labeled neurons of the auditory nerve: correlations with functional properties.,” *J. Comp. Neurol.*, vol. 223, pp. 163–176, 1984.

[147] A. C. Furman, S. G. Kujawa, and M. C. Liberman, “Noise-induced cochlear neuropathy is selective for fibers with low spontaneous rates.,” *J. Neurophysiol.*, vol. 110, pp. 577–86, 2013.

[148] M. G. Heinz, H. S. Colburn, and L. H. Carney, “Evaluating auditory performance limits: i. one-parameter discrimination using a computational model for the auditory nerve.,” *Neural Comput.*, vol. 13, no. 10, pp. 2273–316, Oct. 2001.

[149] B. J. Gantz, G. G. Woodworth, J. F. Knutson, P. J. Abbas, and R. S. Tyler, “Multivariate predictors of audiological success with multichannel cochlear implants,” *Ann. Otol. Rhinol. Laryngol.*, vol. 102, no. 12, pp. 909–916, 1993.

[150] J. Rubinstein and W. Parkinson, “Residual Speech Recognition and Cochlear Implant Performance: Effects of Implantation Criteria,” *Am. J. Otol.*, vol. 20, no. 4, pp. 445–452, 1999.

[151] D. R. Friedland, H. S. Venick, and J. K. Niparko, “Choice of ear for cochlear implantation: the effect of history and residual hearing on predicted postoperative performance.,” *Otol. Neurotol.*, vol. 24, no. 4, pp. 582–589, 2003.

[152] J. B. Nadol, “Degeneration of cochlear neurons as seen in the spiral ganglion of man,” *Hear. Res.*, vol. 49, no. 1–3, pp. 141–154, 1990.

[153] J. B. Nadol, “Comparative anatomy of the cochlea and auditory nerve in mammals.,” *Hear. Res.*, vol. 34, pp. 253–66, 1988.

[154] Z. J. Koles and M. Rasminsky, “A computer simulation of conduction in demyelinated nerve fibres.,” *J. Physiol.*, vol. 227, no. 2, pp. 351–64, 1972.

[155] F. Rattay and H. Felix, “A model of the electrically excited human cochlear neuron . II . In £ uence of the three-dimensional cochlear structure on neural excitability,” vol. 153, pp. 64–79, 2001.

[156] J. Fayad, F. H. Linthicum, F. R. Galey, S. R. Otto, and W. F. House, “Cochlear implants: Histopathologic findings related to performance in 16 human temporal bones,” in *Annals of Otology, Rhinology and Laryngology*, 1991, vol. 100, no. 10, pp. 807–811.

[157] P. Blamey, “Are spiral ganglion cell numbers important for speech perception with a cochlear implant?,” *Am. J. Otol.*, vol. 18, no. 6 Suppl, pp. S11–2, 1997.

[158] J. H. Goldwyn, S. Bierer, and J. Bierer, “Modeling the Electrode-Neuron Interface of Cochlear Implants: Effects of Neural Survival, Electrode Placement, and the Partial Tripolar Configuration,” vol. 268, pp. 93–104, 2011.

[159] J. A. Bierer and K. F. Faulkner, “Identifying cochlear implant channels with poor electrode-neuron interface: partial tripolar, single-channel thresholds and psychophysical tuning curves.,” *Ear Hear.*, vol. 31, no. 2, pp. 247–258, 2010.

[160] J. Tsuji and M. C. Liberman, “Intracellular labeling of auditory nerve fibers in guinea pig:

central and peripheral projections,” *J Comp Neurol*, vol. 381, no. 2, pp. 188–202, 1997.

[161] D. M. Fekete, E. M. Rouiller, M. C. Liberman, and D. K. Ryugo, “The central projections of intracellularly labeled auditory nerve fibers in cats.,” *J. Comp. Neurol.*, vol. 229, no. 3, pp. 432–50, 1984.

[162] M. C. Liberman, “Central projections of auditory nerve fibers of differing spontaneous rate, II: Posteroventral and dorsal cochlear nuclei,” *J. Comp. Neurol.*, vol. 327, no. 1, pp. 17–36, 1993.

VITA

Gabrielle (Elle) O’Brien was born in Stony Brook, New York. After completing her schoolwork at Ward Melville Sr. High School, she received her undergraduate degree in mathematics at Agnes Scott College in Decatur, Georgia. During this time she completed independent research projects on *p*-adic geometry and biophysical models of endogenously rhythmic neurons. In October 2013 she matriculated at the University of Washington to complete her graduate studies in neuroscience.